MASTER

Synchrotron radiation detection and 2D emissivity profile reconstruction in TCV exploring the power of multispectral imaging systems in runaway electron studies

Wijkamp, Tijs A.

Award date:
2020

Department of Applied Physics

Synchrotron radiation detection and 2D emissivity profile reconstruction in TCV

exploring the power of multispectral imaging systems in runaway electron studies

T.A. Wijkamp

Supervisors:
prof. dr. R.J.E. Jaspers
dr. R. Engeln
MSc. A. Perek

Eindhoven, 2019/2020

Abstract

Runaway electron formation and mitigation are among the main hurdles that need to be overcome before magnetically confined nuclear fusion can fulfil its promising role in the energy industry. During plasma start-up, low density operation and disruptions, a relativistic beam of electrons can be formed. Loss of control of such a population forms a major threat to the reactor walls and other components. Designing operation scenarios which avoid their creation, and devising mitigation techniques for formed beams, require accurate theories and models. Validation of these tools should occur through experiments. The non-resolved issue of obtaining the model input in the form of specie temperatures and density distributions, along with the electric field, obscures this comparison. Also, runaways themselves can be considered collisionless and are illusive to most electron diagnostics. This is problematic as the temporal evolution of their distribution function in energy, space and direction of movement is the main quantity of interest in the runaway field.

The multispectral imaging systems designed at the Dutch Institute For Fundamental Energy Research (DIFFER) in collaboration with EPFL and MIT, have the potential to provide the necessary experimental model input as well as information on the runaway population evolution. This class of optical imaging systems is designed to record camera images of several impurity radiation lines at different wavelengths simultaneously, using a nearly identical field of view. In this work the power of multispectral imaging for runaway studies is explored using the beam-splitter based, 4 camera MultiCam system on the TCV tokamak in Lausanne, Switzerland.

Through a tomographic inversion, 2D emissivity maps in the poloidal plane can be constructed for line radiation from neutrals and ions. These can serve as the basis for estimating the essential modelling plasma parameters, being the temperatures and density distributions of electrons and (impurity) ions, by means of suitable collisional-radiative models still under development. As a test case, neutral and singly ionized He emissivity profiles are successfully resolved on the mm scale in a cold runaway companion plasma. With the use of appropriate optical filters, synchrotron radiation from the toroidally revolving runaways is separated from the line emission. Distribution information is extracted via comparison with forward modelled images obtained through the synthetic synchrotron diagnostic SOFT. It is found that the observations can only be explained by the presence of high momentum ($\sim 50\ m_e c$), high pitch angle (~ 0.50 rad) electrons at the edge (normalized radius larger than 0.8) of the plasma. This knowledge is essential for comparison of the experimental results with kinetic models. To support the phase-space and real-space estimates a spectral analysis is performed. 2D ratios of synchrotron patterns at different wavelengths provide a parameter of comparison unique to multispectral imaging systems. Lastly, SOFT behaviour is validated through a vertical position scan of the runaway beam. Changes in pattern geometry are accurately matched by the software, deepening the confidence in this widely used analysis tool. It is concluded that multispectral imaging systems provide a valuable complement to the diagnostics currently available for runaway studies.

Contents

Acknowledgements

The work presented in this thesis would not have been possible without the guidance, support and inspirational discussions of and with a number of people. Firstly, I would like to thank my daily supervisor for showing me the way during my first steps in the world of academic research. What I appreciate most is the relentless enthusiasm he showed when talking about the project, experimental results and the life in fusion research in general. More than once I walked out of his office with renewed spirit and ideas on where to head next in the research after feeling I was somewhat stuck. He allowed me to give direction to my own project while being available to answer any questions I had at any moment (truly any moment). Thanks Artur!

Next I would like to thank my academic supervisors Roger and Richard for having a critical look at my work and progress, urging for me to have a plan B ready when things do not work out as intended (as often in experimental physics) and helping me prioritise my efforts in a project which is so diverse that losing yourself on a side track is an easy mistake to make.

Much inspiration and help was also offered by people I was lucky to meet over the course of my research. I am specifically grateful for the work Bryan Linehan has put into the MANTIS project. Even more than his working ethics its his humour on the job which I appreciate. My host institute DIFFER is a great place to work at, filled with a lot of true researchers who are committed to their goals and interested in what others are doing. The support of the institute for the MANTIS project and my runaway adventure were naturally essential to the results presented here. I would also like to express my gratitude towards the people at TCV for thinking along when the project demanded a lot of flexibility from the mechanics, designers and those in charge of the runaway experiments. This enabled us to get the system ready for operation and obtain the wonderful synchrotron footage during the MST1 campaign.

Furthermore, the warm welcome into the runaway community at the Runaway Electron Modelling meeting was an eye opener for me. It was great to see how productive a research community can be when all involved work together towards the same goal rather than just race each other. For me personally the collaboration with Mathias Hoppe and Gergely Papp was especially important in learning to use the modelling tool SOFT and getting (incredibly fast and detailed) feedback on my analysis of the data.

Last but not of course not least, a big thanks to my family and friends for always expressing their unconditional support for what I do and showing their interest. They provide an enormous source of energy to enthusiastically work towards the goals I set out to achieve.

Chapter 1

Introduction

1.1 The grand potential of nuclear fusion

To sustain and further increase the standard of living all around the world, human kind has to exploit all of its ingenuity to tackle a variety of obstacles that lay ahead. A challenge considered most pressing at the time speaking, is that of ensuring that future generations will be accommodated in their energy demand [1]. The approach to energy production currently adhered to has resulted in unprecedented changes in earth's climate over the last decades [2]. In order to limit and eventually eliminate the toll that energy production takes on the planet, solutions to the energy problem ought to be of a sustainable, environmentally friendly and inherently safe nature.

A prospective candidate for the energy mixture of the future, satisfying all above criteria, is magnetically confined nuclear fusion. Two light elements convert some of their mass to a fast amount of energy when they fuse to form a single nucleus. Here on earth it is not possible to fuse atoms through gravitational force like stars do. Therefore fusion researchers pursue energy production by trapping a 150 million K plasma in some of the strongest magnetic fields developed to date. For the purpose of fusion on our own planet, a deuterium and tritium mixture is the envisioned fuel [1].

Fusion produces no CO_2 and is inherently safe, but the realization of an energy plant has proven to be a tremendous scientific and engineering challenge. Taking into account the deployment time of an energy production source after it has reached maturity, fusion is not expected to contribute significantly to the energy transition on the short term. However, the continuous development of new technologies and the acquisition of fundamental scientific insights in name of nuclear fusion, could let fusion reactors occupy a significant part of the energy sector by the turn of the century [3].

The most developed, although not the only, approach to realizing fusion energy is the tokamak. These devices have at their basis a torus shape vessel, surrounded by magnetic coils. The toroidal field coils generate a magnetic field in the toroidal direction, around which the charged particles gyrate. Gradients in the magnetic field cause particle drifts, and as a result solely a toroidal field will not confine the plasma. This issue is tackled by generating a poloidal field, which will result in the total magnetic field having a helically wound structure. To achieve this a plasma current is induced by a solenoid in the torus center. For steady state operation maintaining this current can also be realized through non-inductive methods [1].

Tokamaks are on the verge of making the transition from the research to the deployment phase. The theoretical and experimental research efforts in the field are culminating in the construction of ITER in the south of France. This 6.2 m major radius tokamak is erected to test current understanding and explore the new physics of a self sustaining fusion reaction [4].

Large tokamaks like ITER are expected to pose scientists and engineers with some challenges that are less daunting in the currently operated smaller devices. One of the major issues foreseen is the formation of a population relativistically fast electrons carrying a significant part of the plasma current, which can pose a serious threat to the system components if they are not confined or slowed down [5]. This thesis deals with the optimization and application of an optical diagnostic which can be used to study these electrons and the techniques devised to mitigate these beams simultaneously.

1.2 Runaway electron beams

Charged particles in a plasma are accelerated under the influence of electric fields. Their drift velocity is limited by Coulomb collisions with other charged particles. Since the frequency of this type of collision scales with the inverse velocity to the third power, highly energetic particles are however not strongly hindered in their acceleration [1, 6]. Beyond a critical energy and driving electric field electrons in a fusion plasma will as a result run away to relativistic velocities. The energy of these runaway electrons (RE) can reach up to tens of MeVs in a tokamak [7, 8].

Runaways are typically produced in a low density, high electric field environment. Events in which the plasma suddenly cools down so that the resistivity increases, and along with that the electric field, are effective initiators for the formation of RE beams. This reveals the strong link of the study on runaways with that on plasma disruptions, in which the energy and current content of a fusion plasma are dissipated on short time scales [9, 10]. The runaway production mechanisms are discussed in detail in section 2.2.

One of the few ways to observe REs in a fusion reactor is to look at the radiation they emit. Like all charged particles, electrons radiate when they are accelerated. The light they send out in the direction of their velocity due to their curved motion in the tokamak is called synchrotron radiation [11]. Usually part of this spectrum falls in the infrared, and suitable diagnostics for direct detection exist [7].

Runaways have emerged as one of the major concerns for ITER [5, 12]. The complete plasma current can be converted to the runaway regime following a disruption. When control is lost over a RE beam its total energy content can end up on a very concentrated region of the vessel. The total energy in such a beam can exceed 100 MJ, causing destruction of the first wall [7, 13]. The threat is especially severe due to the high single particle energy of the relativistic electrons. A single runaway is extrapolated to have an energy up to 100 MeV following an ITER like disruption [14]. It can be shown that 50 MeV electrons already penetrate deep enough into the first wall to cause damage to internal components not meant for replacement [5, 15].

Given the severity of the risks, it is essential to obtain a better understanding of runaway electrons. In particular, it is important that suitable prevention and suppression schemes are developed and experimentally verified. Much attention has been devoted to developing disruption mitigation schemes, aimed at weakening the events which can generate high runaway currents. Despite the progress in this field, it is however likely that in some experiments significant runaway beams will still form. Coming up with methods which dissipate such a population is therefore also of vital importance [16].

Schemes for mitigation developed thus far mainly rely on particle injection to abruptly slow down the runaway beam through collisions. Massive gas injection (MGI) and killer pellet injection are the two options usually considered for this purpose [17, 18, 19, 20].

1.3 Connecting models and experiments

The effectiveness of gas injection as a mitigation tool is highly reliant upon the ability of the impurities to reach the runaway beam and the way the runaways interact with these particles through collisions. Models have been constructed to predict the effect of gas insertion in pre- and post-disruptive plasmas on runaway populations, with the aim of designing effective RE suppression strategies. Well diagnosed experiments are indispensable for the validation and improvement of these codes. The time evolution of the energy and location of the runaway population, as described by kinetic RE models, depends on the plasma temperature, (impurity) density, effective charge state and electric field [21]. Information on the first three plasma parameters can in principle be inferred from light emitted by the plasma through collisional-radiative models. These link emissivity of atomic and molecular species to plasma parameters through collision operators. Developing suitable operators for the interactions in post-disruptive RE filled plasmas is however still work in progress, as runaways can effect ionization and excitation processes significantly increasing the complexity of the problem [22].

Challenges in determining the model input is not limited to the theoretical domain. Accurate reconstructions of the plasma emissivity are a challenge in itself, and errors here propagate through to the implemented impurity distribution, electron density and temperature [23]. Temperatures and densities can be inferred through alternative techniques but are usually of a line integrated nature. Studying electron and impurity dynamics in realistic non-uniform plasmas therefore requires many lines of sight and multiple dedicated systems.

Crucial to model validation is the ability to probe the evolution of the runaway population itself, which is essentially the output parameter of this class of codes. Synchrotron radiation is a promising information source

for passive diagnostics due to the strong dependence of its spectral characteristics on runaway momentum and location. Interpretation of spectra or camera images is however highly non-trivial and usually involves matching of experimental observations to forward modelled diagnostic outputs to constrain the RE distribution function [24, 25].

1.4 Multispectral imaging and the MANTIS system

In a fusion reactor with a large variety of elements at a broad range of energies, and thus ionization states, there is a rich light spectrum emerging from the plasma. Regular camera footage of this light is hard to interpret due to the overlap of the emission contribution from many different species on the resulting image. Spectrometers are more useful in this regard but do not spatially resolve the emission pattern.

An alternative light analysis technique which has found its way to fusion science is multispectral imaging. Particularly noticeable in the field of impurity studies is the Multispectral Advanced Narrowband Imaging System (MANTIS), developed at the Dutch Institute For Fundamental Energy Research (DIFFER) in cooperation with EPFL and MIT. Initially created as a diagnostic and real-time feedback control tool for plasma detachment studies, this device is capable of simultaneously imaging 10 different emission lines over the cross section of a tokamak [26, 27, 28]. The basic set-up is depicted in figure 1.1 A. Light from the tokamak is guided to the entrance of the system via a set of mirrors. Here the bundle is directed towards a first camera with a narrowband interference filter. As depicted in figure 1.1 B, only light at a chosen wavelength is allowed to pass through. Although some of the intensity is lost due to absorption, most light not at the transmission wavelength is reflected off the filter. Via a concave mirror the bundle is directed to a next camera where the process repeats. In this way MANTIS can record the time and spatial evolution of radiation emission patterns for 10 very specific wavelengths using the same camera view. If these are chosen well, the lines are highly representative of a certain type of impurity in a given charge state.

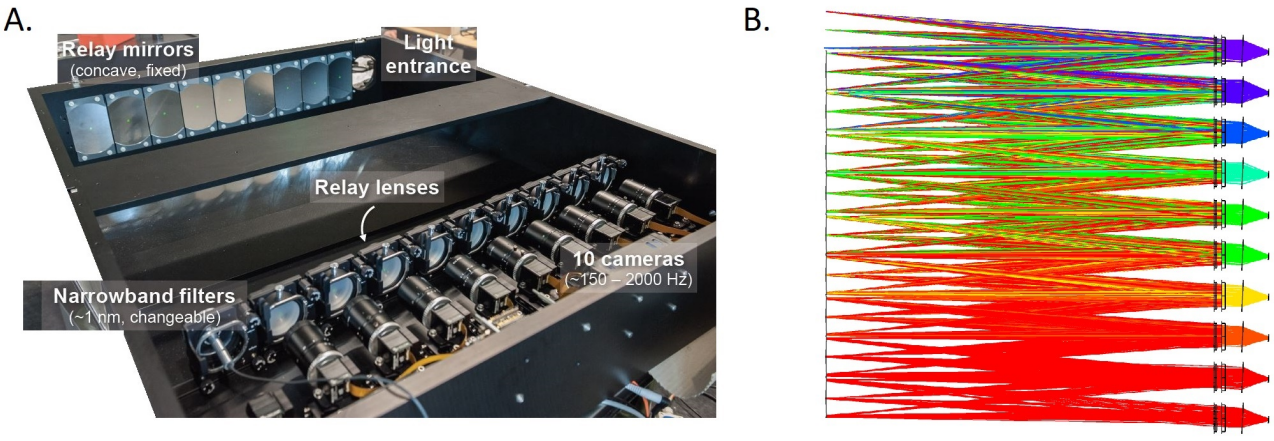

Figure 1.1: A. Basic lay-out of the MANTIS system. Light enters through the entrance slit and is subsequently recorded by 10 cameras with different narrowband optical filters. The light reaches all cameras through reflection off the non-transmitted portion off the filters and a set of concave mirrors. B. Top view of the system with a light ray trace, depicting how the different narrow parts of the initial spectrum are projected onto different cameras. Image with courtesy of Y. Andrebe.

The MANTIS system was tested in the TCV tokamak in Lausanne. An example of a MANTIS image obtained during experiments in TCV is shown in figure 1.2. Quantitative analysis of the impurity distribution directly from these images is limited in extend, as each pixel intensity represents a line integrated measurement. The issue can be solved by means of a tomographic inversion under the assumption of toroidal symmetry of the plasma. Complicated spatial emissivity patterns can be studied in a 2D poloidal coordinate system.

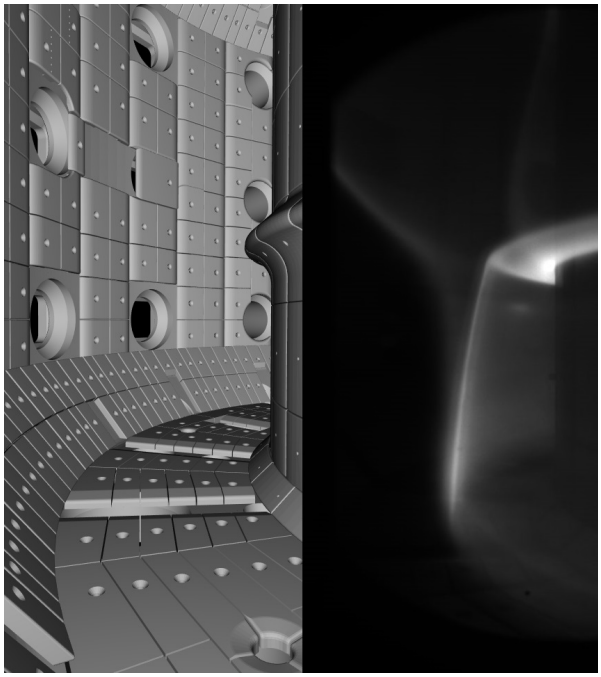

Figure 1.2: Side-by-side image of the TCV divertor region in a CAD model and a MANTIS frame. The MANTIS image shows an example of a CIII line. The light appears to originate only from a certain radial position in the plasma, providing information on the local plasma conditions and constituents.

1.5 MANTIS+: moving to simple, robust design

While further exploring the potential of multispectral imaging in fusion research, the next design steps of the MANTIS line have been initiated. In setting out development plans for technologies in the field of fusion, engineers often have the commercial fusion plant of the future in the back of their heads. This is no different for light based diagnostics, and studies on the system requirements for the 'demonstration power station' (DEMO) are already under way [29, 30]. This concept tokamak is meant to follow up on ITER and would serve as definitive proof of the viability of commercial fusion.

Where ITER diagnostics are designed for scientific purposes, that of DEMO have the sole purpose of providing the input needed for keeping the plasma under control. Robustness, reliability and size are the criteria on which any new system will be judged. The diagnostics have to handle unprecedented neutron and gamma fluxes, should function properly for several years without maintenance or calibration, and should not compromise the breeding of tritium in the reactor blanket [29]. Regardless of whether multispectral imaging will become part of the future DEMO diagnostic mix, making system improvement based on the three mentioned criteria is essential if the successor of MANTIS is to become a standard analysis and control tool in present day fusion experiments.

Implementation of a new smaller, lightweight version of the MANTIS system would also benefit current research inquiries at TCV. Such a device could be installed at one of the TCV middle or upper ports, and provide a head-on view of high-up plasmas. Especially during runaway experiments having a multispectral imaging system with such a viewing geometry would be of added value. Impurity dynamics at the position of the RE beam can be studied. Also, using the right filter set it is not ruled out that synchrotron radiation can be recorded using the same sensors. In this way information on runaway energy and location can be obtained. Multispectral imaging of this kind would be a truly novel and valuable addition to RE experiments. In this thesis the potential of multispectral imaging systems for providing 2D resolved emissivity profiles and synchrotron radiation images for the use in runaway modelling is explored.

1.6 Research question

The potential of multispectral imaging systems to provide input for runaway models, while simultaneously probing the RE distribution characteristics for validation of these same models, warrants an exploration of the use of such systems in actual runaway electron experiments. An experimental proof-of-principle for the emissivity reconstruc-

tion is aimed for using the 4 channel MultiCam system during TCV runaway experiments. The use of one of MANTIS predecessors is motivated by the option to install this small light weight device at the same vertical position as the studied circular plasmas. While recording impurity emission, it should be assessed whether it is possible to detect synchrotron radiation from the RE population in TCV using this system. This is not yet certain due to the relatively low on axis magnetic field of the device. Synchrotron spectra shift towards the infrared with decreasing field, so that the radiation in TCV could fall just outside of the camera wavelength sensitivity range. If detected, synchrotron images can be interpreted with the use of synthetic diagnostics which generate camera images using magnetic field, detector and runaway distribution data. Ideally, constraints on the distribution function can be imposed. These could help validating and benchmarking kinetic codes.

The Medium Sized Tokamak (MST) campaign in the highly flexible TCV tokamak, which has runaway and disruption mitigation studies as one of its main objectives, appears as the ideal opportunity to put multispectral systems to the test in the context of RE studies. TCV has shown to be capable of operating under reproducible runaway scenarios. Full conversion of the plasma current to the relativistic regime can be achieved by gas injection, and excellent spatial control over the beam is in place [16, 31, 32].

From the unique position that MultiCam will be in, the following research questions emerge:

> *Can the MultiCam system generate 2D poloidal emissivity maps on temporal and spatial scales relevant to kinetic runaway models?*
>
> *What part of electron phase space can be detected and identified using visible synchrotron radiation and the synthetic runaway diagnostic SOFT?*

Before conducting experiments it is of importance to understand how selected cameras, optical design and filters influence the uncertainty of the experimental outcome. Specific attention is devoted to limits in the emissivity magnitude accuracy and space resolution, as these are non-straightforward outcomes of various detection, processing and analysis steps.

On the basis of the outcome of this work, potential future directions for the development of multispectral imaging systems in the field of runaway electron studies will be specified. These are chosen on the basis of existing holes in experimental capabilities to probe the parameters governing runaway modelling and theory validation, along with the strengths of the MANTIS line of systems.

1.7 This thesis

Formulations of the answers to the central research questions in this thesis are build-up starting at the theoretical basis, moving on to a description of the diagnostic and lastly treating the experimental results from the MST1 campaign at TCV along with their interpretation. Chapter 2 deals with the physics of runaway electrons. This includes the main formation processes, a description of the characteristic properties and a treatment of synchrotron radiation. The synthetic diagnostic SOFT is addressed, as well as the kinetic theory underlying many modelling tools in the field. Chapter 3 treats models used infer information on the plasma parameters from emissivity profiles, placing the theory in the perspective of runaway filled plasmas. As a basis for describing experimental results, a typical TCV runaway scenario is discussed in chapter 4.

With the theoretical framework in place, attention will be devoted to multispectral systems. Chapter 5 will provide an elaborate overview of MANTIS+, which will also form the basis for treating the MultiCam system used in the TCV experiments. Interference filters are discussed, and uncertainties in emission profile reconstruction are identified and quantified.

MST1 campaign results are treated in chapters 6 and 7. The first section deals with the observation of synchrotron radiation. An attempt is made to trace back the origin of the light using SOFT, and a new spectral analysis method is presented to reinforce the drawn conclusions. Conditions for pattern observations are identified and potential underlying mechanisms are discussed. The second chapter deals with emission profile reconstruction in runaway scenarios, discussing the discharge phases from which one may hope to obtain information and providing a proof of principle for resolving impurity charge states.

The exploratory study is concluded in section 8, assessing the potential of multispectral imaging systems in runaway electron studies. A clear direction for future research is set out on the basis of the strengths of the system.

Chapter 2

Runaway electrons

2.1 Electron collisions in fusion plasmas

2.1.1 Coulomb collisions and the critical field

In the presence of a toroidal electric field, electrons in a fusion plasma are accelerated by the corresponding part of the Lorentz force. The acceleration is limited by collisions with other charged particles. Taking into account that small scattering angle collisions dominate the Coulomb interactions in thermal plasmas, the relativistic scattering cross-sections for electron-electron and electron-ion collisions can be used to construct the following expression for the drag force [33]:

$$\vec{F}_d = -\frac{e^4 n_e \ln(\Lambda)}{4\pi\epsilon_0^2 m_e v_e^2}\Big(1 + \frac{Z_{eff}+1}{\gamma}\Big), \tag{2.1}$$

where the electrons have charge e, density n_e, rest mass m_e and velocity v_e, the constant ϵ_0 is the permittivity of vacuum and $\ln(\Lambda)$ is the Coulomb logarithm. The relativistic factor γ is related to the electron velocity and the speed of light c as $\gamma = 1/\sqrt{1-(v/c)^2}$. The effective charge Z_{eff} of a quasi-neutral plasma is defined as [1]

$$Z_{eff} = \frac{\sum_j Z_{s,j}^2 n_j}{n_e}, \tag{2.2}$$

where the sum is over all ion species j, with charge $Z_{s,j}$ and density n_j. The collision frequency ν_{clb} is found by dividing the friction force by the relativistic momentum $\gamma m_e v_e$ [7, 1, 34]:

$$\nu_{clb} = \frac{e^4 n_e \ln(\Lambda)}{4\pi\gamma\epsilon_0^2 m_e^2 v_e^3}\Big(1 + \frac{Z_{eff}+1}{\gamma}\Big). \tag{2.3}$$

Note that the collision frequency shows a rather strong decrease with increasing particle velocity. Electrons for which the force exerted by the electric field exceeds the experienced drag will be continuously accelerated to relativistic velocities [35]. The critical velocity $v_{e,c}$ beyond which this force imbalance starts to occur is obtained by equating expression (2.1) to the electric force, which yields[7]:

$$v_{e,c} = \sqrt{\frac{e^3 n_e \ln(\Lambda)\Big(1 + \frac{Z_{eff}+1}{\gamma}\Big)}{4\pi\gamma\epsilon_0^2 m_e E_\parallel}}, \tag{2.4}$$

where $E_\parallel$ is the component of the electric field along the magnetic field lines. An often referred to quantity in the field of runaway physics is the Dreicer field E_D. It is defined as the parallel electric field for which the critical velocity equals the thermal electron velocity $v_{th,e} = (k_b T_e/m_e)^{1/2}$, where k_b is the Boltzmann constant and T_e the electron temperature [35]. Using equation (2.4) this leads to the following expression:

$$E_D = \frac{e^3 n_e \ln(\Lambda)}{4\pi\gamma\epsilon_0^2 k_b T_e}\Big(1 + \frac{Z_{eff}+1}{\gamma}\Big). \tag{2.5}$$

The relativistic friction force introduces a lower limit on the electric field strength required to produce runaways. Below this limit no RE production occurs and any existing population will thermalize. This critical electric field E_c is for a fully ionized plasma given by the Connor-Hastie field [6, 9]:

$$E_c = \frac{e^3 n_e \ln(\Lambda)}{4\pi\epsilon_0^2 m_e c^2}. \tag{2.6}$$

Knowledge of the critical field is important, as it is a decisive parameter in both the generation and decay of runaway current [9]. The treatment above however does not take all the electron physics into consideration, and is only approximately valid in the limit where no electrons are bound to atoms. Actual critical fields are usually a few factors higher than that predicted by equation (2.6). This is appears to be mainly due to (i) the fact that particles lose energy through synchrotron radiation and Brehmstrahlung, and (ii) the presence of partially ionized impurities in the plasma [36, 9]. The latter explanation is related to the fact that runaways can probe the internal structure of atoms so that bound electrons form a sea of particles to interact with. Suitable modifications to equation (2.6) are discussed in appendix A.

2.2 Production mechanisms

Typically, runaways are produced when either the plasma density is low or the electric field increases on a short time scale. Keeping the plasma density at a low level limits the critical electric field, so that this threshold is easily surpassed for instance during the start-up phase of a tokamak discharge [36]. Sudden increases in the electric field are usually the result of rapid plasma current and energy dissipation during plasma disruptions. In such an event the plasma quickly cools, the resistivity increases and the electric field follows the same trend [5, 8, 16]. In this section the production mechanisms relevant for the work presented here are addressed.

2.2.1 Direct generation

Consider the case when the electric field exceeds the critical field from equation (2.6). If part of the initial Maxwellian population exceeds the critical velocity, this portion will runaway to the relativistic regime. The rest of the distribution remains close to Maxwellian in case of a steady-state plasma [37]. This so called Dreicer generation process has been found to lead to a gradual conversion of current in low density plasmas [38]. While the high energy electrons are drained by the runaway process, the tail of the distribution is replenished by collisional processes [39].

An approximate expression for the steady state growth of the runaway population via Dreicer generation is given by [40]:

$$\frac{dn_{RE}}{dt} = C_{Dreicer} n_e \nu_{th} \Big(\frac{E}{E_D}\Big)^{-3(1+Z_{eff})/16} \exp\Big(\frac{-E_D}{4E} - \sqrt{\frac{1+Z_{eff}}{E/E_D}}\Big), \tag{2.7}$$

where ν_{th} is the electron-electron collision frequency of thermal particles

$$\nu_{th} = \frac{n_e e^4 \ln(\Lambda)}{4\pi\epsilon_0^2 m_e^2 v_{th}^3}, \tag{2.8}$$

which decreases with the thermal electron velocity $v_{th} = \sqrt{2eT_e/(\pi m_e)}$. Note that the production rate depends strongly on the ratio between the electric field and Dreicer field. A relativistic treatment yields a correction to the Dreicer formula above and was derived by Connor and Hastie [6].

2.2.2 Secondary generation

The second important production mechanism is that of secondary generation. Via this path a small seed population of REs can initiate a quick conversion of a large portion of the plasma current to the relativistic regime. As will be clarified next, such production on short time scales is especially pronounced in large tokamaks. The avalanche effect is a direct consequence of head-on, large angle collisions between runaways and members of the low energy electron population. If sufficient energy is transferred, and $E > E_c$, the low energy electron may be pushed over the critical velocity boundary and run away to high energies. Thus, a secondary RE is produced while the initial runaway will stay in this regime as well [41, 8].

To illustrate some of the properties of the avalanche process, the Rosenbluth Putvinski runaway growth rate in the cylindrical approximation is used [42, 40]:

$$\frac{dn_{RE}}{dt} = n_{RE}\nu_{th,rel}\frac{E/E_c - 1}{\sqrt{3(Z_{eff}+5)/\pi}\ln(\Lambda)}\Big(1 - \frac{E_c}{E} + \frac{4\pi(Z_{eff}+1)^2}{3(Z_{eff}+5)((E/E_c)^2+3)}\Big)^{-1/2}, \tag{2.9}$$

where $\nu_{th,rel}$ is the thermal collision rate of relativistic particle for which $v_{th} = c$ is adopted. In the approximation $E/E_c \gg 1$ the growth rate is proportional to the runaway density and the parallel electric field. Equation (2.9) effectively illustrates two characteristic properties of the avalanche effect. First of all, the solution to this equation in the large electric field limit is of exponential form. Secondly, the exponentiation factor is proportional to the electric field [43]. The field present during a plasma disruption depends on the plasma current I_p used to produce the poloidal field. Therefore, a device like ITER is expected to show an avalanche effect of about a factor of $\exp(I_{p,ITER}/I_{p,TCV}) \approx \exp(15)$ larger than in TCV [4, 44]. What process is dominant in RE production is thus strongly dependent on the machine size. Also, this quick calculation gives an indication as to how problematic runaway production could be for the future generations of fusion devices. In an ITER current quench one may have fields of 80-100 V/m during a short period of around 150 ms [38, 45]. At such fields this duration is plenty to convert the 16 MA plasma current to a RE beam [4].

Just like the critical electric field, also the runaway production rate estimates are modified if one takes into account the interaction of REs with bound electrons. For electric fields strongly exceeding the critical field, the growth rate predicted by equation (2.9) is an underestimation. Due to the partial screening effect, the chance of runaways to undergo a head-on collision with free and bound electrons is essentially equal. Adding impurities to the plasma thus increases the reservoir of low energy electrons which can become part of the runaway current [46].

2.3 The orbit of runaways

A discussion of the parameters by which runaway populations are characterized demands a spatial framework. It is common practise to indicate the position of runaways using a toroidal coordinate system in r, θ and ϕ, which are defined in figure 2.1. In some occasions a Cartesian coordinate system is more intuitive, which is therefore also indicated.

Another concept important in the description of runaway orbits is that of flux surfaces. Fusion plasma equilibria and their disturbances are often derived from the theory of magneto hydrodynamics (MHD), which treats the plasma as an electrically conducting fluid. The equations at its basis reveal that magnetic field lines lie on surfaces of constant pressure in an equilibrium situation [1]. These surfaces form nested cylinders each enclosing a fixed magnetic flux, and are therefore referred to as flux surfaces. The helicity of the field lines on a surface can be characterized using the safety factor q, defined as:

$$q(r) = \frac{1}{2\pi}\int \frac{B_\phi}{RB_\theta}dl, \tag{2.10}$$

where the integral is taken over a closed poloidal contour. The magnetic fields B_ϕ and B_θ are the components in the toroidal $\hat{\phi}$ en poloidal $\hat{\theta}$ directions respectively. The coordinate R denotes the distance from the z-axis to the evaluated point, and is equal to $\vec{R} = (R_0 + r\cos(\theta))(\cos(\phi)\hat{x} + \sin(\phi)\hat{y})$ with R_0 the major radius of the toroid, being the distance from the origin to a point on the toroids central axis. A convenient simplification, valid for $r << R$, is to approximate the safety factor in the toroidal geometry by that for a cylinder, which yields:

$$q(r) = \frac{rB_\phi}{RB_\theta}. \tag{2.11}$$

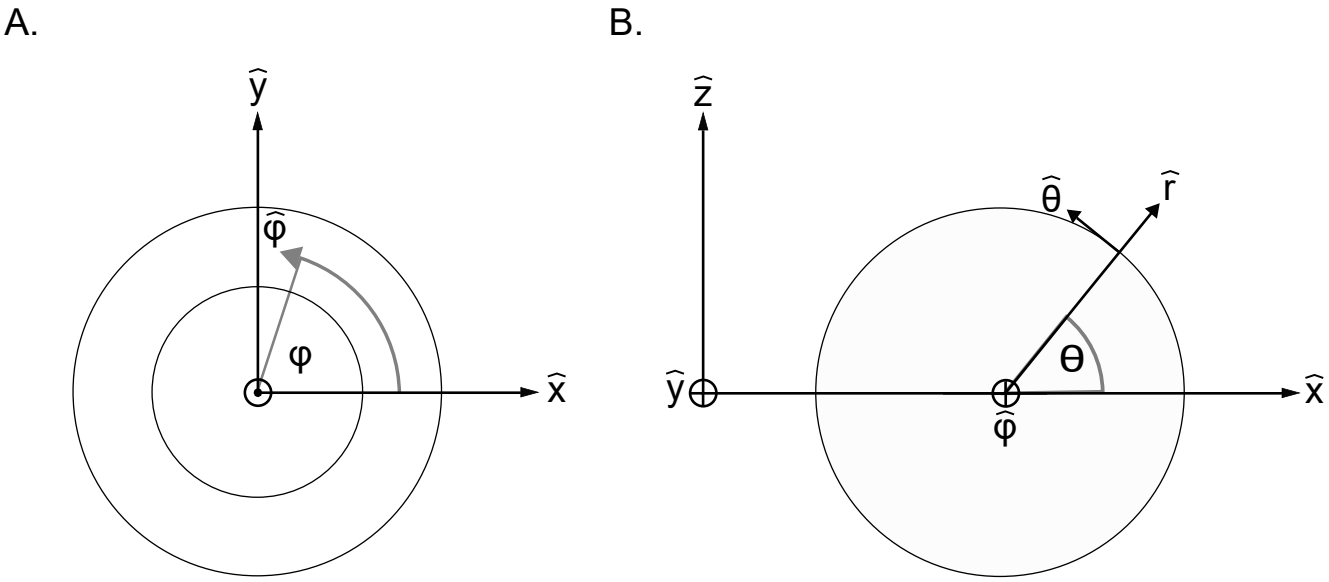

Figure 2.1: Cartesian x, y, z and toroidal r, θ, ϕ coordinate system. A) Top view of the toroid. B) Poloidal cross-section.

This geometrical factor can also be understood as the amount of toroidal revolutions a field line makes before it has undergone a single poloidal turn.

With the basic framework for describing electron motion in tokamaks in place, the typical movement of runaways can be described. First of all, the question arises where these fast electrons are generated in the first place. During steady-state plasma operation the temperature and current profiles tend to peak near the magnetic axis around which the flux surfaces form. Since the electrons are thus more energetic near the center than at the edge, a larger portion of the population can overcome the runaway threshold and is accelerated to the RE regime. Primary production mechanisms during a steady phase in the discharge thus tend to create a beam in the center of the machine [7].

When a disruption occurs the energy is quickly dissipated, and the peaked profiles typically flatten. Since the dominant portion of the current is however situated near the central axis, due to the higher temperature and thus lower resistance here, this is also the region where during the current quench phase the largest electric fields arise. The critical field is thus most easily surpassed near the center, and here the current to RE beam conversion process is strongest. For typical tokamak operation runaways are thus generated around the magnetic axis. Experiments as well as numerical models confirm this behaviour [47].

Once generated, the runaways follow a trajectory composed of three different components. First of all, charged particles gyrate around magnetic field lines. The motion of electrons around their guiding center, which is the gyration averaged electron position, occurs at the electron cyclotron frequency $\omega_{ce,e}$ [34]

$$\omega_{ce,e} = \frac{eB}{\gamma m_e}, \tag{2.12}$$

with a corresponding Larmor radius $\rho_{l,e}$:

$$\rho_{l,e} = \frac{\gamma m_e v_{e,\perp}}{eB}, \tag{2.13}$$

where $v_{e,\perp}$ is the electron velocity component perpendicular to the magnetic field direction. The guiding center of the particle motion follows the helically twisted magnetic field lines, forming the second contribution to the electron motion. Reconstructing the magnetic surfaces during primary RE generation processes is thus of importance for accurate modelling. Lastly, the orbit is displaced from the magnetic field surface due to gradient, curvature and $E \times B$ drifts. This shift δ_{orbit} can be estimated by balancing the Lorentz force component on the electron due to the poloidal magnetic field with the centrifugal force due to the electron motion in the poloidal plane [7]:

$$\delta_{orbit} \approx \frac{\bar{q}W}{ecB_\theta}. \tag{2.14}$$

In equation(2.14) $\bar{q}$ is the electron trajectory averaged safety factor and W is the particle energy. A final important parameter describing the electron motion is their pitch angle Θ, which is the angle between the particle velocity vector and the magnetic field:

$$\Theta = \arctan\left(\frac{v_{e,\perp}}{v_{e,\parallel}}\right). \tag{2.15}$$

The pitch angle strongly influences the transport and radiation properties of the runaway population. Orbit displacements of runaways are also coupled to this parameter. A more general version of equation (2.14) taking into account a finite pitch angle is

$$\delta_{orbit} \approx \frac{p\cos(\Theta)}{ecB_\theta}(1 + \frac{1}{2}\tan^2(\Theta))r. \tag{2.16}$$

2.4 Energy of runaway electrons: limits and estimates

The electron runaway process is not one without limits. Radiative energy loss, a growing orbit radius, resonance with magnetic field ripples and plasma instabilities provide an upper bound to the energy which electrons can attain [48]. Which of these effects actually sets the limit depends on the reactor and plasma parameters.

Before briefly treating the different limits, a short note on the relation between kinetic energy W and momentum p as they are both used to indicate the velocity of runaways. The latter is often expressed in units of $m_e c$. For relativistic electrons of rest mass m_e:

$$W^2 = (pc)^2 + (m_e c^2)^2. \tag{2.17}$$

The first upper boundary is set by the fact that the critical field is surpassed for a limited amount of time. Neglecting collisions and radiation energy losses the maximum energy $W_{e,max}$ attained at any point in time is the product of the toroidal gyration frequency and the energy gain per revolution:

$$W_{e,max|V_l}(t) = \frac{ec}{2\pi R_0}\int V_l(t')dt'. \tag{2.18}$$

The loop voltage V_l is equal to the electric field multiplied by the toroidal circumference. For a typical TCV runaway shot, lasting 1.5 s from the first primary generation onwards and which has an average loop voltage in the order of 0.5 V, this yields a maximum energy of around 41 MeV.

A second boundary is set by the radiative losses of particles in gyrating motion. Electrons follow the helically wound magnetic field lines, while rotating about them at their cyclotron frequency. The superposition of both movements constitutes a complicated helical path. A more detailed treatment of synchrotron radiation is presented in section 2.5.1. For the time being the radiative power loss P_{syn}, dominated by the toroidal motion, is simply given [7]:

$$P_{syn} = \frac{\mu_0 e^2 c^3}{6\pi R_c^2}\gamma^4, \tag{2.19}$$

where μ_0 is the permeability of vacuum and R_c the curvature radius for helical electron motion. This last parameter can by approximated by [48]

$$\frac{1}{R_c} \approx \frac{1-\Theta^2}{R_0} + \frac{eB\Theta}{m_e c\gamma_e}. \tag{2.20}$$

To find the upper bound for the electron energy, this loss term is balanced to the energy gain due to acceleration by the electric field. Considering a collisionless electron, which is a good approximation for electrons near speed c, one gets [34]

$$P_{V_l} = \frac{eV_l c}{2\pi R_0}. \tag{2.21}$$

Solving the quadratic equation for γ which results from equating equations (2.21) and (2.19), yields

$$\gamma_{max|syn} = \frac{R_0 e B_0}{2m_e c} \frac{\Theta}{1-\Theta^2} \Big(\sqrt{1 + (\frac{2m_e c}{eB_0\Theta})^2 \frac{1-\Theta^2}{R_0} \sqrt{\frac{3\epsilon_0 V_l}{eR_0}}} - 1 \Big). \tag{2.22}$$

From γ one can determine the relativistic energy of an electron W_e:

$$W_e = \gamma m_e c^2. \tag{2.23}$$

The limit depends strongly on RE pitch angle. Consider a TCV RE discharge, with a loop voltage of 0.85 V, a major radius of 0.88 m and an on axis field of 1.43 T [31]. For zero pitch angle the energy limit is at 54 MeV, and decreases with increasing Θ to reach 28 MeV at 0.2 rad. Strong scaling of the synchrotron losses with γ furthermore prevent runaways from reaching much higher energies even at larger electric fields. Doubling E to 1.7 V the limit at zero pitch angle increases by merely 10 MeV.

Another limit follows directly from the orbit shift calculated using equation (2.14). An electron orbiting near the magnetic axis is lost if the shift is equal to the minor radius of the device. The limit is calculated for TCV. As a crude approximation of the average q-profile, assuming a constant current density and using the cylindrical system estimate of equation (2.11), a value of 2.5 is chosen. This leads to a maximum electron energy of 42 MeV. This is incidentally very similar to the two previously mentioned limits.

Runaways are also prohibited from reaching indefinitely high energies due to an interaction of the electrons with ripples in the magnetic field caused by the finite amount of toroidal field coils. If the electron cyclotron frequency is in resonance with the frequency at which the electron feels the periodical changes in the magnetic field, the electrons are scattered and change pitch angle. As a result the synchrotron radiation limit can be lowered significantly due to enhanced radiation losses at larger pitch angles, as will be discussed in section 2.5.1. The energy corresponding to the resonance condition for the first harmonic is [7]:

$$W_{e,max|ripple} = \frac{ecR_0 B}{N_{coil}}, \tag{2.24}$$

with N_{coil} the amount of toroidal field coils of the device. Higher order resonances occur at lower energies, but are much weaker. For TCV equation (2.24) predicts a limit of 23 MeV. This is somewhat lower than the loop voltage, synchrotron radiation and orbit shift limits. The arguments used to derive these upper boundaries for the electron energy are merely approximations, but do reveal that REs in TCV could obtain energies of several tens of MeV. At the start of the discharge the RE energy is expected to be limited by the shot duration up to that point, while the other mentioned limits can start to play a role at later times. A description of typical TCV runaway shots is given section 4.

A last note on runaway energy limits is that instabilities of the plasma can also prevent the electrons from reaching higher energies. At certain energy thresholds the REs can exchange energy with resonant oscillations in the plasma, powering these fluctuations [34]. Numerical studies have also shown that plasmas in which a large fraction of the current has been converted to the runaway regime, are likely to exhibit a low q, high internal inductance state prone to kink instabilities [49]. In this way interaction with MHD modes can lead to a direct change in the electron energy or a loss of confinement.

Elaborate modelling of ITER RE disruptions indicate that runaways will most likely attain energies in strong excess of the TCV upper bounds. On the basis of Monte-Carlo models expectations are that runaway energies of 100 MeV will not be an exception in case of a disruption, with a bulk residing in the order of 10 MeV [14].

2.5 Synchrotron radiation

2.5.1 The origin and characteristics of synchrotron radiation

Given the prominent role that synchrotron radiation measurements have in this research, an overview of the theory related to its emission and detection is warranted. In appendix B it is derived that the angular power emitted by charged particles of position $\vec{r}$, velocity $\vec{u}$ and acceleration $\vec{a}$ is given by

$$\frac{\partial P}{\partial \Omega} = \frac{\vec{\tilde{r}} \cdot \vec{u}}{\tilde{r}c} S_{rad} \tilde{r}^2 = \frac{q^2}{16\pi^2 \epsilon_0} \frac{|\hat{\tilde{r}} \times (\vec{u} \times \vec{a})|^2}{(\hat{\tilde{r}} \cdot \vec{u})^5}. \tag{2.25}$$

With this tool in hand, the radiation characteristics of the electron synchrotron problem can be addressed. To this end consider a particle with an instantaneous velocity $\vec{v} = v\hat{z}$ and a perpendicular acceleration $\vec{a} = a\hat{x}$. If one positions the electron in the origin $\vec{\tilde{r}} = \vec{r}$, where $\vec{r}$ is the point of evaluation. In a spherical coordinate system with polar angle θ_s from the z-axis and azimuthal angle ϕ_s from the x-axis in the x-y plane, $\vec{r} = r\sin(\theta_s)\cos(\phi_s)\hat{x} + r\sin(\theta_s)\sin(\phi_s)\hat{y} + \cos(\theta_s)\hat{z}$, and equation (B.4) gives a synchrotron emission power per solid angle of:

$$\frac{\partial P_{syn}}{\partial \Omega} = \frac{cq^2\beta^4}{16\pi^2\epsilon_0 R^2} \frac{\big(1 - \beta\cos(\theta_s)\big)^2 - (1-\beta^2)\sin^2(\theta_s)\cos^2(\phi_s)}{\big(1 - \beta\cos(\theta_s)\big)^5}, \tag{2.26}$$

with R the radius of curvature, which for runaways in a tokamak can be approximated using equation (2.20). This distribution, for $\phi_s = 0$, is shown for different values of β in figure 2.2 A. For each particle velocity, the output power is normalized to its maximum value over all solid angles, so that the radiation patterns can be compared more easily. First of all, notice that the electron emits radiation primarily along the angle $\theta_s = 0$, which is in the direction of the particle velocity. The higher the particle energy, the more concentrated the synchrotron radiation is along the vector $\vec{v}$. With this knowledge, one can expand equation (2.26) for small angles $\theta_s << 1$ and high relativistic factors $\gamma >> 1$;

$$\frac{\partial P_{syn}}{\partial \Omega} \approx \frac{cq^2\beta^4\gamma^6}{2\pi^2\epsilon_0 R^2} \frac{(1+\theta_s^2\gamma^2)^2 - 4\theta_s^2\gamma^2\cos^2(\phi_s)}{(1+\theta_s^2\gamma^2)^5}.$$

The angle for which $\partial P_{syn}/\partial\Omega = 0$ now is $|\theta_s| = 1/\gamma$, which is a good approximation for half the emission cone aperture.

Although figure 2.2 A reveals the emission geometry, it hides the fact that the actual power output for different values of β varies strongly. The approximation for the total power expression in equation (B.5) was already given in expression (2.19). This dependency is illustrated in figure 2.2 B, where the power is plotted as a function of β values between 0.1 and 0.9999 for TCV parameters and a pitch angle of 0.1. Notice that as the particle approaches the speed of light, the emitted power readily shoots up. A 1 MeV electron radiates less than 1 percent of its energy away every second, while this initially is above 10 percent for one with an energy of 10 MeV. The high energy part of an electron population thus typically dominates the total radiative output.

To consider the full picture the angular spectral synchrotron radiation function of equation (B.6) is studied. This is done in the high energy limit $\gamma \gg 1$, $\theta_s \ll 1$. The instantaneous energy distribution, for which $\omega_{ce} t_r \ll 1$, is:

$$\frac{\partial^2 W}{\partial\Omega\partial\omega} \approx \frac{q^2}{12\pi^3\epsilon_0 c}\Big(\frac{\omega}{\omega_c}\Big)^2\Big(\theta_s^2 + \frac{1}{\gamma^2}\Big)^2\Big(K_{2/3}^2(\zeta) + \frac{\theta_s^2}{\theta_s^2 + 1/\gamma^2}K_{1/3}^2(\zeta)\Big),$$

where $K_{1/3}$ and $K_{2/3}$ are modified Bessel functions of the second kind and $\zeta = \frac{1}{3}(\omega/\omega_c)(\theta^2 + 1/\gamma^2)^{3/2}$ [50]. The power output per frequency interval is now found by multiplying this expression by the toroidal revolution frequency of the electron and integrating over the full solid angle. A conversion to the wavelength λ domain gives [7]:

$$\frac{\partial P_{syn}}{\partial \lambda} = \frac{e^2 c}{\sqrt{3}\epsilon_0\gamma^2\lambda^3} \int_{\frac{4\pi R_c}{3\lambda\gamma^3}}^{\infty} K_{5/3}(x)dx. \tag{2.27}$$

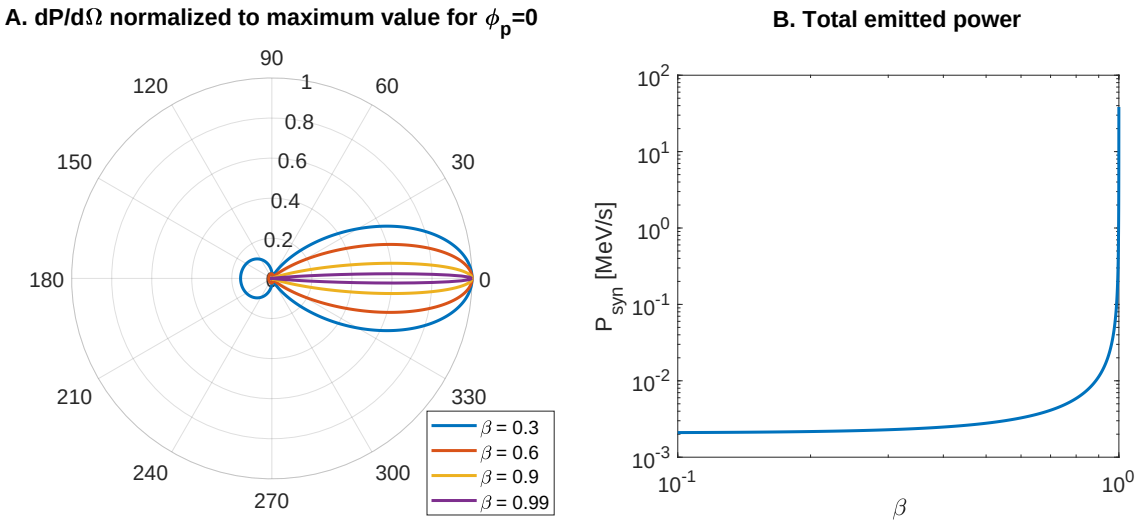

Figure 2.2: A) Synchrotron emission power per solid angle according to equation (2.26) in the $\phi_s = 0$ plane for different values of β. Note that the intensities are normalized to their maximum value (at $\theta_s = 0$). The figure clearly illustrates that the emission angle decreases with particle velocity, and is concentrated in the direction of the particle movement. B) Total emitted synchrotron radiation power as a function of the particle energy. As the charge approaches the speed of light there is a sharp increase in radiative losses.

The properties of this function are illustrated in figure 2.3. First of all, figure A shows how the spectral distribution of the synchrotron emission varies with particle energy for TCV machine parameters. Evidently, the emission peak shifts to smaller wavelengths as the energy increases. Note that for a pitch angle of 0.1, the emission peak is at 4.1 μm for a 30 MeV electron, which is beyond the maximum energy expected at TCV based on the energy limits. At 800 nm, above which most visible light cameras start to have a poor detection efficiency, the intensity of the radiation has already dropped off to less than 1 percent of the peak value.

In figure 2.3 $\partial P_{syn}/\partial\lambda$ is displayed for a 30 MeV particle at different pitch angles. Firstly, note that the total emitted power scales strongly with Θ. Electrons with a large perpendicular velocity are expected to have a dominant contribution to the total emission spectrum of a runaway population. Also, the calculations indicate that the emission peak shifts to lower wavelength with increasing pitch angle. At a pitch angle of 0.40, the peak is situated around 1.3 μm and $\partial P_{syn}/\partial\lambda$ is three to five orders of magnitude larger in the visible range than for an electron with pitch angle 0.10. This gives the clear indication that cameras operating in this range are relatively sensitive to high energy, large pitch angle runaways.

While the derivation of equation (2.27) is convenient for illustrating the nature of synchrotron emission, it is based on the assumption of electrons moving in a circular path around the torus. This can be resolved through Lorentz transformations in the particle frame of reference. Furthermore, for the purpose of determining the radiation an external observer would perceive, one has to correct for the fact that the light source is moving close to the speed of the light it emits. This introduces an additional correction. The spectral power in a homogeneous field now becomes [25]

$$\frac{\partial P_{syn}}{\partial\lambda} = \frac{e^2 c}{\sqrt{3}\epsilon_0\gamma^2\lambda^3}(1-\beta\cos(\Theta)\cos(\mu))\int_{\frac{4\pi m_e c\gamma_\parallel}{3\gamma^2 eB\lambda}}^{\infty} K_{5/3}(x)dx, \tag{2.28}$$

where μ is the angle between the particle guiding center tangency line and the line-of-sight of the observer. The error made by neglecting the cyclotron motion of the electron in the cylindrical geometry for which equation (2.28) is valid, can be assessed by comparing the equation to more complete expressions. A treatment of synchrotron emission by Pankratov taking into account gryo-motion, cyclotron motion and orbit drifts shows that ignoring the cyclotron component to the emission is expected to give accurate results in case the electron momentum p and pitch angle Θ satisfy [51]:

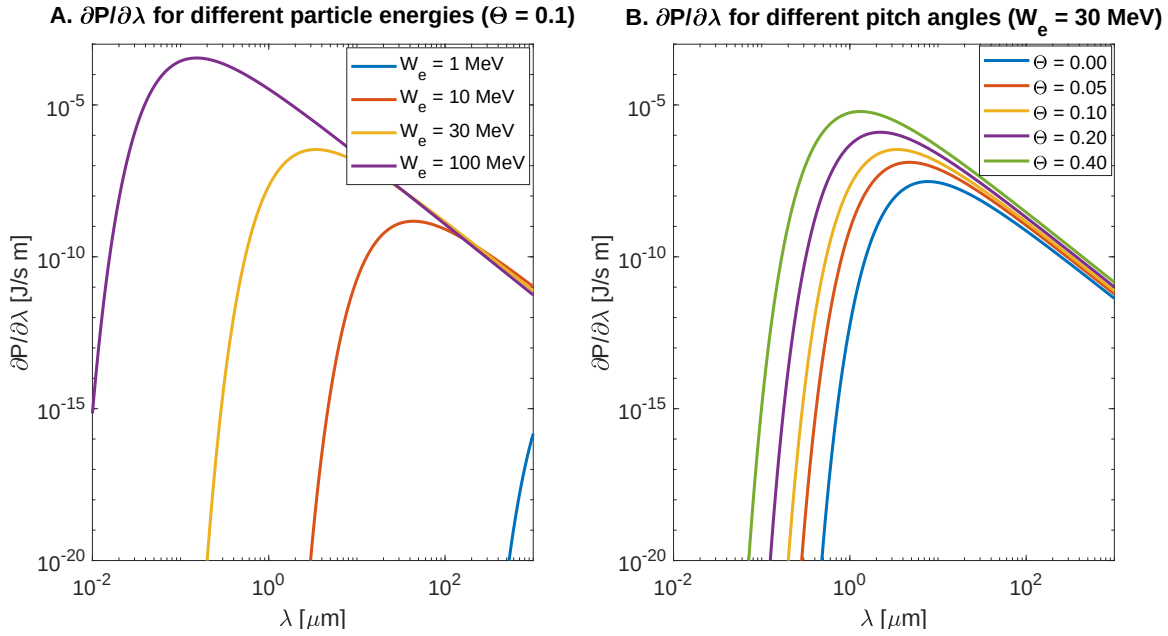

Figure 2.3: A) Spectral distribution of synchrotron emission for different particle energies and TCV machine parameters. Note the shift of the peak intensity to lower wavelengths with increasing energy. B) Spectral distribution for a 30 MeV particle at different pitch angles. For larger pitch angles the emission at higher frequencies increases.

$$\eta = \frac{eBR}{p}\frac{\sin(\Theta)}{\cos^2(\Theta)} \gg 1.$$

For TCV central axis conditions $\log 10(\eta)$ is plotted in figure 2.4. The red line indicates the curve for which $\eta = 1$. Note that at high energies equation (2.28) is only expected to yield accurate results for relatively large pitch angles.

2.5.2 Generation of synthetic synchrotron camera patterns using SOFT

The theory presented above is not sufficient to predict and interpret images perceived by cameras during runaway experiments. As explained, the direction of emission is strongly focussed along the electron velocity. The emission pattern is therefore highly dependent on the particle path and thus on the magnetic field line structure. Only radiation from a specific part of the RE distribution, in terms of position, energy and pitch angle, will reach an observer. In recent years synthetic synchrotron emission tools have been developed to study the correlation between the runaway distribution function and the emission pattern as perceived by optical diagnostics. The software used in this work to interpret the light emitted by the electrons is the Synchrotron-detecting Orbit Following Toolkit (SOFT) [25]. The strength of this framework lies in the fact that it is computationally efficient while retaining most of the runaway physics. In this section of brief overview of the software is provided.

The central equation

SOFT is designed to construct the total intensity I_{tot} of electron radiation originating from an optically thin plasma, which arrives at a given detector. This intensity is a function of (i) an angular electron radiation intensity distribution $dI/d\Omega$ in position $\vec{r}$ and momentum $\vec{p}$ space as inferred from an input magnetic field and detectable wavelength range, (ii) a camera position $\vec{r}_{detector}$, viewing direction $\hat{n}$ and viewing angle Ω_n, (iii) and the phase space distribution function $f_e(\vec{r},\vec{p})$ of the electrons:

$$I_{tot} = \int\int\int O\left(\frac{\vec{r}'}{r'}\right)\frac{\vec{r}'\cdot\hat{n}}{(r')^3}\frac{dI(\vec{r},\vec{p},\vec{r}')}{d\Omega} f(\vec{r},\vec{p})d\vec{p}dVdA, \tag{2.29}$$

where one integrates over the plasma volume V and detector area A, and $\vec{r}'$ is the difference vector between the detector and volume element $\vec{r}_{detector} - \vec{r}$. The function $O\left(\frac{\vec{r}'}{r'}\right)$ is equal to 1 if $\vec{r}'/r'$ falls inside the viewing cone Ω_n

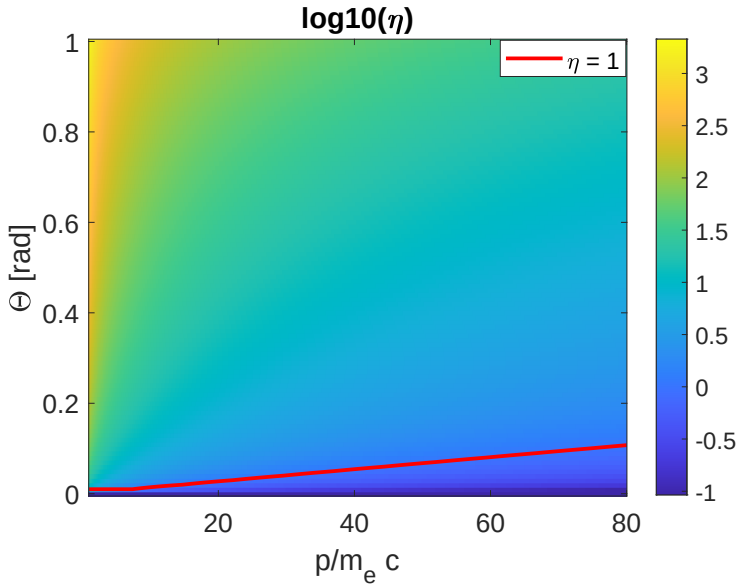

Figure 2.4: Phase-space map of $\eta = (eBR\sin(\Theta))/(p\cos^2(\Theta))$, which gives an indication as to whether the cylindrical synchrotron equation (2.28) is expected to yield accurate results. For $\eta < 1$ the cyclotron component to synchrotron radiation starts to become important.

and 0 otherwise, so that one only integrates over the volume elements which are in the field of view. Projection of the radiation I onto the detector plane is ensured by the element $(\vec{r}' \cdot \hat{n})/(r')^3$. Note that the distribution function essentially weighs the intensity of the light emitted by some electron in the phase space $(\vec{r}, \vec{p}, \vec{r}')$ by its abundance in the plasma. The geometric factors introduced above are also illustrated in figure 2.5.

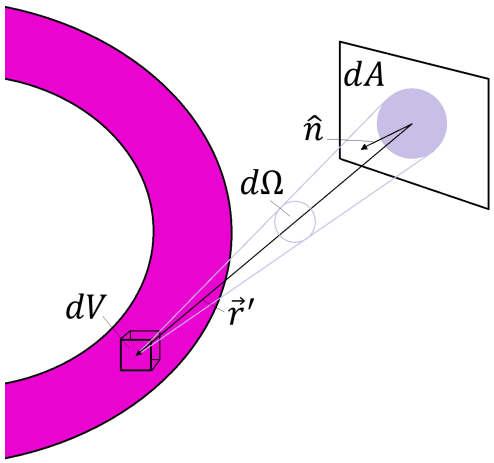

Figure 2.5: Overview of geometric quantities which reappear in the SOFT central equation (2.29). Light emitted in a cone $d\Omega$ by volume element dV lands on a detector with different area dA. The position of the detector with respect to the emission source is $\vec{r}'$, and the surface normal is $\hat{n}$.

When operating the software, concrete input to SOFT consists of (i) an electron distribution function in momentum, pitch angle and minor radius, (ii) a magnetic field specified in the toroidal plane and (iii) detector spectral range, location, viewing angle and aperture. Magnetic field data for TCV is available through the Grad-Shafranov solver LIUQE, which uses magnetic probe data at the vessel boundary as boundary conditions [52].

Numerically integrating equation (2.29) requires a choice of phase-space parametrization and discretization. The position space is discretized in orbits. This choice has the particular advantage that once the distribution function is known on one place on an orbit, it is known everywhere along that same trajectory. The underlying Liouville's theorem holds provided that the distribution function changes slowly as compared to the orbit time. In guiding-

center formulation electron trajectories are obtained by integrating over their gyro angle, so that they follow the magnetic field lines. This is valid to good approximation if the gyro radius is much smaller than the typical spatial scale over which the magnetic field fluctuates [8]. The phase space treatment described here becomes inaccurate for too high electron energies, or situations in which fast plasma dynamics is observed such as during a disruption.

The breakdown of zeroth-order guiding-center theory at high energies is related to the orbit drift described in section 2.3 and gyro-orbit deformations at large electron momenta. The latter is only significant if the perpendicular momentum component is of comparable magnitude as the parallel component. First order drift corrections to the electron orbit are implemented in SOFT. The phase-space region of validity of the software will be assessed more extensively in future endeavours by the SOFT developing team through comparison with, computationally expensive, full-orbit models.

The set of guiding center coordinates adopted consists of the maximum major radius of the orbit ρ, a time coordinate τ which is 0 for $R = \rho$, a gyro angle and the toroidal angle, parallel momentum $p_\parallel$ and perpendicular momentum $p_\perp$ at time $\tau = 0$. Parallel and perpendicular here refer to momentum vector orientation with respect to the local tangent-line of the guiding-center orbit or magnetic field. In this formulation, the integral (2.29) can be re-written as:

$$I_{tot} = \int\int\int G(\rho, p_\parallel, p_\perp) f_e(\rho, p_\parallel, p_\perp) p_\perp d\rho dp_\parallel dp_\perp. \tag{2.30}$$

The function $G(\rho, p_\parallel, p_\perp)$ is referred to as the diagnostic response function or Green function, and includes the integral over the detector surface, gyro angle, orbit time and toroidal angle. It constitutes the orbit averaged received emission of particles positioned at $(\rho, p_\parallel, p_\perp)$ in phase space. The electron distribution function again serves as a weight factor to find the total emission received by the detector. As the numerical implementation of this equation takes the form of a matrix multiplication, one can quickly compute I_{tot} for any electron distribution function once G has been constructed. When analysing synchrotron pattern change over time, G will have to be modified if the magnetic field changes configuration with respect to the camera.

The parametrization presented in equation (2.30) is not the only right choice. Users of SOFT have the choice among a wide variety of options, and one which will also be used frequently in this work is that in the total momentum p, pitch angle Θ and minor radius ρ. Equation (2.30) changes Jacobian in this framework. Furthermore, the intensity on the detector can be reconstructed as a function of wavelength. Correctly incorporating the effect of transmission filters requires one to convolve the output Green function with the filter transmission $T(\lambda)$. To construct synthetic detector output, the equation used here is thus:

$$I_{tot} = \int\int\int\int G(\rho, p, \Theta, \lambda) f_e(\rho, p, \Theta) p^2 \sin(\Theta) T(\lambda) d\rho dp d\Theta d\lambda. \tag{2.31}$$

This does not take into account the camera sensitivity curve which will have to be corrected for in experimental data to allow a comparison.

Finding the diagnostic response function

In order to determine the diagnostic response function an angular emission model for the electrons has to be selected

Since relativistic electrons emit light almost exclusively in their direction of motion, the light emitted by a runaway gyrating around a magnetic field line can by approximated by a hollow cone centred on the guiding-center orbit. Its width scales as $\sim 1/\gamma$, and the cone is therefore assumed to be infinitely thin. This is illustrated in figure 2.6 A. Integrating the total emitted power $P(p_\parallel, p_\perp)$ of a particle over the gyro angle θ_{gyro}, the power load on the detector thus takes the form [8]

$$\int_0^{2\pi} \frac{dP}{d\Omega} d\theta_{gyro} = P(p_\parallel, p_\perp) \delta\Big(\hat{v}_{gc} \cdot \hat{n} - \cos(\Theta)\Big). \tag{2.32}$$

The direction vector $\hat{v}_{gc}$ is that of the guiding center, and the delta function indicates that the detector only receives light in case it is somewhere on the emission cone. Note that the opening angle of the cone is equal to the pitch angle Θ. The highly non-isotropic nature of synchrotron and bremstrahlung emission creates the situation in which each distribution function has an associated surface-of-visibility. This is a bended and twisted surface

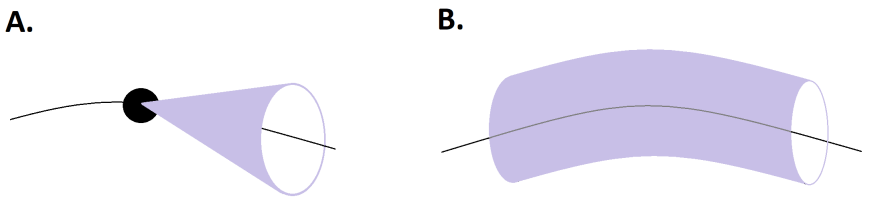

Figure 2.6: A) An electron following its guiding-center while emitting synchrotron radiation under a pitch angle Θ due to its gyrating motion and the directional nature of the emitted light. B) Example of a surface of visibility for a fixed detector configuration, electron distribution and magnetic geometry.

defining all the points from which the specified detector will receive light. A visualization of the concept is shown in figure 2.6 B, where it takes the form of a cylinder. In case the detector is a camera, the constructed image will be a 2D projection of the surface-of-visibility onto the detector plane. Note that the registered pattern intensity is particularly pronounced where the viewing line-of-sight is tangential to the surface-of-visibility.

The notion of a surface-of-visibility can also be developed using the light received from individual points in phase space. For a single radius, parallel momentum and perpendicular momentum, the detected pattern of light consists of one or multiple traces on the detector. As an example a TCV magnetic equilibrium, retrieved from shot 64614 at 1.1 seconds using LIUQE, is used as input for SOFT to generate traces corresponding to 12 MeV electrons, at a minor radius of 0.5 times that of the last closed flux surface, with pitch angles of 0.1, 0.4 and 0.7 rad. The detector parameters correspond to that of a visible-light camera with a 640 nm filter installed on the middle port, at nearly the same height as the magnetic axis. Aforementioned traces are shown in figure 2.7 A, where the light coming from each separate point in phase space has been assigned a different color to highlight the geometrical effects. A top view of the patterns is provided in figure B, where the magnetic axis is indicated using the dotted blue line and the detector position is that of the red dot. Note how particles at different pitch angles contribute to the image at very different positions even though their radial locations are identical. For sufficiently high pitch angles the surface-of-visibility consists of two separate ones at different toroidal positions, moving apart as the pitch angle increases.

For a realistic non-single particle distribution, the total pattern is a superposition of all phase-space traces weighted by the electron distribution function and some Jacobian. Figure 2.7 C shows that the intensity weights in the example case differ by many orders of magnitude depending on the pitch angle. What portion of the electron distribution thus dominates the total image is an interplay between this change in intensity and the particle abundance. The complex geometric and light intensity effects make the interpretation of synchrotron images highly non-trivial. Careful modelling is needed to make any statement on what part of phase-space is observed in an image.

Obtaining an expression of the Green function is the primary aim of SOFT. Knowledge of this parameter helps one to find out what part of the phase-space the detector is sensitive to. Usually this is only a portion of the actual runaway population, so that from a single camera image no statements can be made on the shape of the total distribution. However, using multiple cameras or camera wavelength sensitivities, different points on the distribution curve can be found and compared.

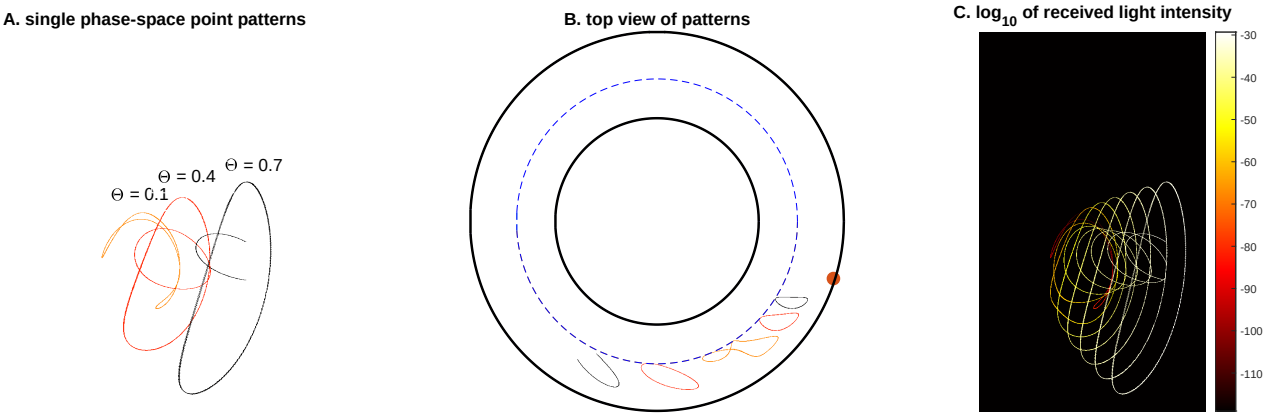

Figure 2.7: SOFT output for individual phase-space point electrons in a magnetic equilibrium extracted from TCV shot 64614. The particles of different pitch angles have an energy of 12 MeV, and orbit at a normalized minor radius of 0.5. The displayed projections are those onto a visible light camera with a 640 nm filter at a middle port. A) Projected traces for three different pitch angles, showing the geometrical effects of directed synchrotron emission. B) Top view of the position of the corresponding surfaces of visibility, along with the magnetic axis in blue and the detector position in red. C) Logarithmic intensity map for eight different values of the pitch angle ranging from 0 to 0.7.

2.6 Kinetic description of runaway dynamics

2.6.1 The kinetic equation

Understanding runaway formation and mitigation requires numerical models describing the collective behaviour in momentum and position space. One of the most developed and successful underlying theoretical frameworks to date is the kinetic description, in which the time evolution of the aforementioned distribution function $f_e(\vec{p},\vec{r})$ in momentum and position-space is linked to electromagnetic and drag forces inside the plasma. For tokamak conditions a large aspect-ratio limit of the gyro- and bounce- averaged Fokker-Planck equation is adopted. Neglecting spatial dependency of plasma parameters the kinetic equation takes the form [21, 40]

$$\frac{\partial f_e}{\partial t} - eE\hat{B}\cdot\nabla_{\vec{p}} f_e = C(f_e) + S(f_e). \tag{2.33}$$

The second term on the left-hand-side describes acceleration by the electric field component along the magnetic field direction $\hat{B}$. On the right-hand-side are the collision terms $C(f_e)$ and all particle and heat source terms $S(f_e)$. The latter can include slowing-down terms due to synchrotron and bremsstrahlung emission.

Note that the Fokker-Planck equation itself is derived under the assumption of small-angle collisions dominating changes in the electron population. The head-on collisions driving avalanche generation are therefore not incorporated in the theory. Using a suitable source term this deficiency in the theory can however be overcome [40, 53, 54].

2.6.2 Steady-state solutions

Fitting synthetic images to real synchrotron patterns requires one to adopt a certain functional form of the electron distribution function. The less parameters the curve can be described with, the lower the computational demand on the fitting procedure. Steady-state analytical solutions to equation (2.33) can be found given that appropriate simplifications are made. Input for SOFT calculations treating quiescent steady-state runaway discharges in TCV has the highest demand for an accurate distribution function shape at large momenta. The underlying argumentation is that this part of the population is expected to dominate the emission in the visible, as argued in section 2.5.1. For a parallel momentum strongly exceeding that of the 'O-point', at this location in phase-space the collisional drag and pitch angle scattering are of similar size, drag-damping can be ignored with respect to pitch angle scattering so that [55]

$$f_e(p_\parallel, p_\perp) = f_0 \exp(c_1 p_\parallel) \exp(c_2 p_\perp^2), \tag{2.34}$$

where c_1 and c_2 are negative constants with theoretical values

$$\begin{aligned} c_1 &= -\frac{2c_3(1+Z_{eff})}{m_e c(E/E_c - 1)^2} \\ c_2 &= -\frac{c_3}{(m_e c)^2(E/E_c - 1)} \\ c_3 &= \frac{2\epsilon_0 B^2}{3 n_e m_e \ln(\Lambda)}. \end{aligned}$$

The third term c_3 is a measure of the synchrotron radiation strength. An analytical expression in the case where avalanche effect dominates the distribution evolution has been derived with the use of a Rosenbluth-Putvinski source [56]. The full expression is

$$\begin{aligned} f_e(p, \Theta) = \frac{n_{RE}}{\sqrt{3\pi(Z_{eff}+5)}\cos(\Theta) p \ln(\Lambda)} \frac{E/E_c - 1}{2(1+Z_{eff})} \\ \exp\Big(- \frac{\cos(\Theta)p}{\sqrt{3(Z_{eff}+5)/\pi}\ln(\Lambda)} - \frac{E/E_c - 1}{2(1+Z_{eff})} \tan(\Theta)\sin(\Theta)p \Big). \end{aligned} \tag{2.35}$$

This equation is approximately valid if $\gamma \gg 1$ and $E/E_c \ll 1$. A 2 parameter fitting form of this equation can therefore be written as:

$$f_e(p, \Theta) = \frac{f_0}{\cos(\Theta)p} \exp\Big(d_1 \cos(\Theta)p + d_2 \tan(\Theta)\sin(\Theta)p \Big).$$

Chapter 3

Collisional radiative models

The collision and source terms in the kinetic equation are a function of the temperature and density distributions of electrons and (impurity) ions. One way to obtain experimental estimates of such quantities is through the light emitted by the different plasma constituents. Multispectral systems provide the data required to construct 2D emissivity profiles in the poloidal plane through the calibration procedures described in section 5. These are valuable on their own for making qualitative statements on the spatiotemporal distribution of impurities. Extracting the electron temperature and density however requires a bridging model.

In this chapter two models linking the distribution of different ionization and excited states to electron density and temperature are treated. The Corona model can be used for quick estimates of ionization distributions. A more widely applicable and complete framework is that based on rate equations. The collisions and excitation states which need to be included in the model depend on the plasma conditions, and are identified here. Recent advances in the RE community on including the collisions between runaways and the background plasma are summarized. Conditions under which runaway driven excitation becomes important for interpreting emissivity profiles are extracted. This is needed for the interpretation of emissivity profiles treated in this work.

3.1 The Corona model

First, a simple to use framework for obtaining ionization stage distribution estimates is treated in the form of the Corona model. This framework is approximately valid for low density plasmas, such as the one in fusion reactors. It is assumed that all transitions to higher levels are collisional, and that to lower levels are radiative. Also, the plasma is postulated to be ionizing, meaning that recombination from the next ionization state as a populating source is neglected. In plasmas where the model applies well, the population of exited states of a certain specie is negligible compared to that of the ground state [57]. The ionization state densities n_z are related by [58]:

$$\frac{n_{z+1}}{n_z} \approx 10^8 \frac{\zeta_z}{n_{QN,z}} \frac{T_{e,eV}}{\chi_z^3} \exp(-\frac{\chi_z}{k_b T_e}), \tag{3.1}$$

where χ_z is the ionization energy, $n_{QN,z}$ is the principle quantum number of the highest non-empty electron shell in the ion ground state and ζ_z the number of electrons in this shell. The region of validity can be estimated by demanding that states have a hydrogen-like energy and sufficient radiative transitions to lower levels. This sets an upper density limit of [59]:

$$n_e \leq 6 \cdot 10^{16} (z+1)^6 T_{e,eV} \exp\Big(\frac{0.1(z+1)^2}{T_{e,eV}}\Big), \tag{3.2}$$

where z is the ion charge in units of e. Note that this implies that the limit becomes less severe with increasing ionization state. In a cold (sub 10 eV), post-disruptive plasma the limit for neutral particles is at $6.0 \cdot 10^{17}$ m^{-3}, and the model accuracy is uncertain. For $z > 0$ and pre-disruptive temperatures the Corona model is expected to provide accurate estimates.

3.2 The rate equation model

This section contains an inquiry into the most commonly used category of collisional radiative models (CRM). To obtain accurate results for a wide range of plasma parameters rate equations are typically used. The time evolution of the different particle states are coupled through a multitude of collisional radiative processes, depending on which are expected to be dominant. A good example of the implementation of such a model is found within the Atomic Data and Analysis Structure (ADAS). In the name of this project a large database of atomic data has been collected from literature, which can be accessed through the OPEN-ADAS search tool [60].

For illustrative purposes a model including electron impact- excitation, de-excitation and ionization, along with electronic recombination and spontaneous emission is build up [61]. Including these processes accurate results are to be expected for plasmas with very low RE content, such that ionization and excitation channels related to these relativistic electrons are negligible. Progress on extensions of this framework and the limits of its applicability are treated in section 3.4.

In the simple case where one assumes that only the ground state of each ionization level is populated, the time evolution of the density of each state is governed by three collisional-dielectronic coefficients. These constants depend on the temperature and density of the free electron population which is assumed to be Maxwellian [62]. An effective ionisation coefficient S_{CD}, recombination coefficient α_{CD} and charge exchange recombination coefficient C_{CD} are distinguished. For some ionization state of charge z, the density evolves according to [60];

$$\frac{dn_{(z)}}{dt} = -n_e S_{CD,(z)} n_{(z)} + n_e S_{CD,(z-1)} n_{(z-1)} + (n_e \alpha_{CD,(z+1)} + n_o C_{CD,(z+1)}) n_{(z+1)}, \tag{3.3}$$

where n_o denotes the density of other particle species which can donate an electron during charge exchange. Note that $C_{CD,z}$ will depend on the type of particle with which the charge exchange occurs. Deviating expressions are in order for the neutral and fully ionized states as recombination and ionization can not occur in the respective cases. The system as a whole can be expressed in matrix form as

$$\begin{bmatrix} dn_{(0)}/dt \\ dn_{(1)}/dt \\ \vdots \\ dn_{(Z)}/dt \end{bmatrix} = C \begin{bmatrix} n_{(0)} \\ n_{(1)} \\ \vdots \\ n_{(Z)} \end{bmatrix}, \tag{3.4}$$

where C is a matrix with coefficients $C_{z,z'}$ for $z, z' = 0, 1, ..., Z$.

$$\begin{aligned} C_{z,z-1} &= n_e S_{CD,(z-1)} \\ C_{z,z} &= \begin{cases} -n_e S_{CD,(0)} & \text{if } z = 0 \\ -n_e (S_{CD,(z)} + \alpha_{CD,(z)} + \frac{n_e}{n_0} C_{CD,(z)}) & \text{if } z = 2, 3, ..., Z-1 \\ -n_e (\alpha_{CD,(Z)} + \frac{n_o}{n_e} C_{CD,(Z)}) & \text{if } z = Z \end{cases} \\ C_{z,z+1} &= n_e \alpha_{CD,(z+1)} + n_o C_{CD,(z+1)}. \end{aligned}$$

An equilibrium ionization state distribution can be found by setting the left-hand-side vector components in equation (3.4) to zero. Although illustrating the concept of CRMs well, the model above is strongly simplified. The ionization and ordinary recombination term both describe transitions driven by electron impact. Ion impact, radiative recombination, three-body recombination and spontaneous decay are not considered. Also, only the regular ground state of each ionization level is considered. Long-lived metastable states and other excited levels are not taken into account.

To assess what model extensions in terms of resolved species and state transitions are relevant to add to the model, the different time scales of the processes are considered. Denoting the decay time of metastables and ordinary excited states as τ_m and τ_o respectively, typical charge dependent values are given by [62]

$$\begin{aligned} \tau_m &\approx 10/z^8 \\ \tau_o &\approx 10^{-8}/z^4. \end{aligned} \tag{3.5}$$

The life time of the ground state is governed by the ionization and recombination time scales:

$$\begin{aligned} \tau_{ion} &= [10^{11} - 10^{13}](z+1)^4 \sqrt{\chi_H / k_b T_e} \exp(\chi_z / k_b T_e)/n_e \\ \tau_{rec} &= [10^{17} - 10^{19}](1/(z+1)^2) \sqrt{k_b T_e / \chi_H}/n_e. \end{aligned} \tag{3.6}$$

Here χ_z is the ionization energy of charge state z and χ_H that of hydrogen. The characteristic time scale estimates for neon are depicted in figure 3.1 as a function of electron temperature. Time scales are weighed sums over all ionization levels computed using the Corona ionization stage distribution. The figure indicates that metastable populations have life times which are large compared to ionization and recombination processes at sub 10 eV temperatures. This indicates that significant populations of such particles may exist in neutral and low-z impurity populations. The simple set of linear equations (3.4) do not resolve metastable states, and might thus be an inadequate representation of reality for these low-temperature plasma states.

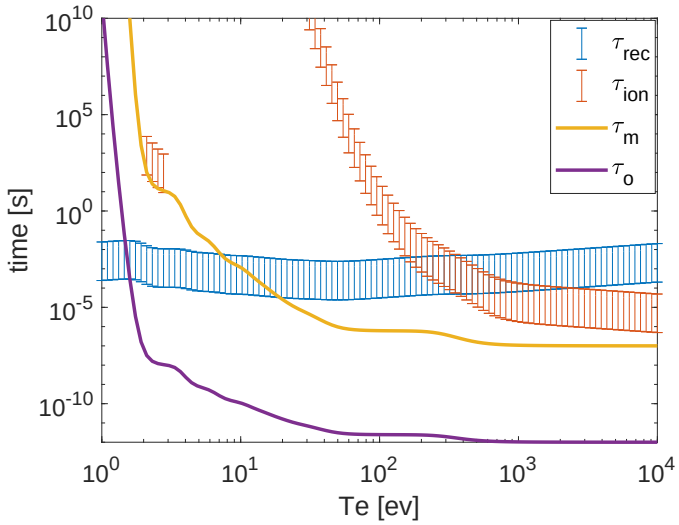

Figure 3.1: Estimate for the characteristic life times of ordinary and metastable neon states along with ionization and recombination time scales. All time scales are mean values over all ionization stages, and are displayed as a function of electron temperature. These have been computed using the Corona equilibrium to determine the distribution over different ionization stages.

For low-z species, the ADAS database harbours rate constants for metastable particles, offering a solution to the issue of having to incorporate these species in the model. The modified approach is a natural extension of equation (3.3) and is treated in appendix C. Equations (C.2) and (C.3) together allow one to solve for the equilibrium populations if the time derivatives are set to zero.

Another observation which can be made on the basis of figure 3.1, is that the lifetime of metastables can be on a scale which is large compared to that of typical plasma dynamical processes [62]. This could render an equilibrium description of the particle state distribution as assumed up till now inaccurate. To deal with such issues metastable resolved time dependent approaches to collisional radiative modelling have been developed [61, 63]. Note that the equilibrium assumption usually does hold for the excited states of impurities. This means that the emission emerging from the decay of such states can be decoupled from transport equations [62]. To use the time dependent equations in interpreting emission profiles one would have to combine it with an impurity transport model. Only in this way the changing n_e and T_e conditions for a specific group of impurity particles due to translation can correctly be accounted for.

From the discussion presented here, it is concluded that under fusion reactor plasma conditions a metastable approach is required for low ionization stages. In cold post-disruptive plasmas where it is only neutrals and low ionization stages which radiate using the extended model is therefore of essence.

3.3 Emission and line ratios

To relate experiment to theory the gap between the population distribution, which is a function of electron temperature and density, and the observed emission from the plasma has to be bridged. Doing so requires some assumptions about the origin of the observed light. First of all, it is assumed that the emissivity contribution from a specific energy transition of an impurity specie can be separated from other sources. The emission coefficient for the spectral line under consideration, resulting from the decay of state i to state j, is given by [64]

$$\epsilon_{i\to j} = \frac{n_i A_{i\to j}}{4\pi}, \tag{3.7}$$

where $A_{i\to j}$ denotes the Einstein coefficient for spontaneous emission. Extending the model for ionization and metastable states to one also including the ordinary excited states, n_i can be found and the emission ratio for transition $i \to j$ and $i' \to j'$ is simply [63]

$$R_{ij,i'j'} = \frac{A_{i\to j} n_i}{A_{i'\to j'} n_{i'}}, \tag{3.8}$$

given a certain 2D emission profile. In this way line ratio can be used to find the population ratio $n_i/n_{i'}$, which through the CRM can be related to a particular combination of electron density and temperature. In practise the uncertainty range in n_e and T_e obtained from a single ratio measurement is rather large and even multiple wildly varying solutions may come forward. Therefore it is usually necessary measure at least two line ratios to find these plasma parameters through light detection.

Information which can be used to calculate the steady state population of ordinary excited states is bundled together with spontaneous emission rates in so called photon emissivity constants PE. These are the product of the Einstein coefficient for some transition and a parameter which indicates the reaction cross section. The excited states are mainly occupied through electron collision excitation of the ion under consideration, or by free electron recombination of the parent ion [62]:

$$\epsilon_{(z,i\to j)} = n_e\Big(\sum_{k=1}^{M_(z)} PE^{(exc)}_{(z,\sigma[k],i\to j)} n_{(z,\sigma[k])} + \sum_{k=1}^{M_{(z+1)}} PE^{(rec)}_{(z+1,\nu[k],i\to j)} n_{(z+1,\nu[k])}\Big), \tag{3.9}$$

where $PE^{(exc)}_{(z,\sigma[k],i\to j)}$ is the electron excitation term for an initial metastable state $\sigma[k]$ and $PE^{(rec)}_{(z+1,\nu[k],i\to j)}$ is the recombination photon emission coefficient for the parent metastable $\nu[k]$.

3.4 Collisional radiative models for runaway filled plasmas

The rate coefficients used to infer quantitative information from emissivity profiles depend on the mechanisms driving ionization, recombination, excitation and de-excitation. Coefficients in the ADAS database are applicable to plasmas over a wide range of densities and temperatures, but do not capture the effect of relativistic electrons on the mentioned processes. To get an idea of when ADAS coefficients are reliable and when runaways become important to CRMs the work by Garland et al is briefly treated [22]. They show that in low temperature plasmas with high-Z species the ion charge state distribution and radiative properties can be dominated by runaways. After a thermal collapse in ITER radiative losses would be dominated by the RE current rather than deuterium or impurities.

Quantum electrodynamic modifications to the collisional excitation and radiation cross sections of electrons with atoms are the underlying reason for the severe deviations from regular CRM coefficients. These yield an increase in cross section for collisions above a $\sim$1 MeV threshold rather than the traditionally expected decrease. Electron energy loss per travelled distance in a background plasma increases linearly with the bound electron density according to Bethes electron stopping formula. Also, this energy transfer channel increases with a decrease in mean ionization potential, and therefore is more important for low ionization states. These two trends combined cause this mechanism to dominate ionization and excitation processes after a thermal quench when temperatures drop to a few eV. The runaways can not be decoupled from the plasma any longer in CRM treatments.

The exact role of runaways in ionization and excitation processes in TCV are yet to be determined. A study of such nature using a CRM that couples the background plasma self-consistently to the runaway population is outside

the scope of this work. Based on the results presented in the work by Garland et al, a rough guideline for the use of ADAS coefficients can however be extracted. Expectations are that these describe pre-injection conditions accurately, but are inadequate to obtain quantitative information from the emissivity profiles in post-disruptive RE companion plasmas. This is to be taken into account when interpreting emission profiles described in this work.

Chapter 4

TCV runaway scenario

Interpretation of synchrotron patterns and emissivity profiles benefit from prior knowledge of the prevailing plasma conditions. Experimental results presented in chapters 6 and 7 are obtained for strongly varying densities, temperatures and plasma constituents. In this section the different phases encountered during TCV RE experiments are highlighted through a treatment of the standard circular plasma scenario with a gas injection triggered disruption and subsequent RE avalanche production. Quiescent experiments, where runaways are formed through primary mechanisms in a low density non-disruptive plasma, are in essence an extension of the pre-injection phase and are thus treated along the way. The disruption scenario has been proven reproducible, which is required for studying the effects of externally controllable plasma parameters on the RE beam position, formation and decay [31].

To highlight the different stages of the discharge, experimental data from runaway shot 63433 are shown in figure 4.1. The evolution of the plasma current (A), loop voltage (B), electron density (C,D) and hard x-ray counts are shown as a function of time. The loop voltage data is derived from the flux loop encircling the central solenoid at $Z = 0$, which is the geometrical central height plane of the tokamak. The FarInfraRed (FIR) interferometry data shows an average electron density along the $R = 0.903$ m line, which is closest to the center of the plasma. Thomson scattering derived data for the electron density concerns the position $R = 0.900$ m, $Z = 0.228$ m. The PhotoMultiplier Tube for X-rays (PMTX) delivers a signal which increases with the amount of detected X-rays and their energy.

During the experiment a central toroidal magnetic field of 1.43 T is used, and the Ohmic L-mode plasma carries a 200 kA current. After plasma start-up, signified by a spike in the loop voltage, the discharge enters a stationary phase during which the density is kept at a low level to allow primary RE seed generation in low critical field conditions. TCV densities during this stage are typically around the $5 \cdot 10^{18}$ m^{-3} level shown in figure 4.1 D. Pre-disruptive temperatures are in the order of 1 keV. The seed formation is critical for the eventual avalanche driven RE beam generation. If densities are too high in the initial stationary discharge phase, no runaway beam is observed. The experimentally found limit is around $1 \cdot 10^{19}$ m^{-3} [31, 32, 65]. In this device secondary mechanisms are furthermore expected to be small during the low density phase [31]. In quiescent scenarios this low density state is maintained until the end of the shot.

During MGI experiments the equilibrium situation in the plasma is disrupted by a gas injection at the time indicated by the blue dashed line in figure 4.1. A particle injection locally cools the plasma and it was found that this leads to the onset of strong MHD activity when the cold front reaches the $q = 2$ surface [66, 67, 68]. This triggers a collapse of the plasma thermal energy on a time scale of 5-10 ms, known as a thermal quench (TQ) [31, 68, 69]. In the resulting landscape of chaotic magnetic field lines, magnetic islands and flux tube near the central axis may persist. These can confine and sustain the existing runaway population formed during the pre-disruption phase [70, 71]. Note that beyond this point the density measurements provided by the Thomson scattering system become inaccurate.

In the TCV TQ phase the electron temperature is found to drop from 1 keV to a few eV. Due to the rapid temperature drop in the TQ phase, the resistance momentarily increases significantly since it scales as $\sim T^{-3/2}$ [1]. An increased electron reservoir and electric field also mean that secondary runaway generation through the avalanche effect becomes important. In the presence of a hot RE seed population a strong runaway beam is achievable [31].

The TQ stage is followed by a current quench (CQ), during which the current decays over a time scale of tens to

hundreds of ms. Alternatively, TCV feedback systems can sustain I_p at a fixed level to isolate the effects of current decay through gas injection. Full conversion of the plasma current to the runaway regime has been observed in TCV. Beam stability up to 650 ms has been achieved, giving plenty of time to test mitigation strategies [65]. The post-disruption phase is accompanied by a low loop voltage due to the negligible resistance of runaways which start to dominate the current [31].

Figure 4.1 E also shows a strong increase in the PMTX signal after the initial gas injection, indicating that the runaways collide more frequently with the walls. Through colliding with the vessel REs decelerate quickly, which produces the observed x-rays. On top of the steady x-ray signal, short lived spikes can be observed during the post-disruptive phase. These mark short expulsions of RE current due to momentary disturbances in beam stability.

The mitigation approach in the experimental scenarios discussed here consists of a second gas injection at the time indicated by the red dotted line in figure 4.1. MGI tens to hundreds of times stronger than the initial gas injection can be used to study the influence on the current decay. TCV furthermore allows the beam to be moved around in the vessel through its excellent vertical stability control. Therefore, the gas injection location relative to the beam can be varied. The amount of gas which can be used for mitigation purposes is limited by the ability of the vacuum pumps to process the injected quantity [67].

Right after the second injection figure 4.1 shows a quick drop in the plasma current, as the runaways are slowed down through collisions with the heavy gas. Not all runaways are lost through this channel as the PMTX signal spike shows. Beam stability is lost during the second injection, and many runaways hit the wall during the final current decay stage, causing the PMTX to saturate.

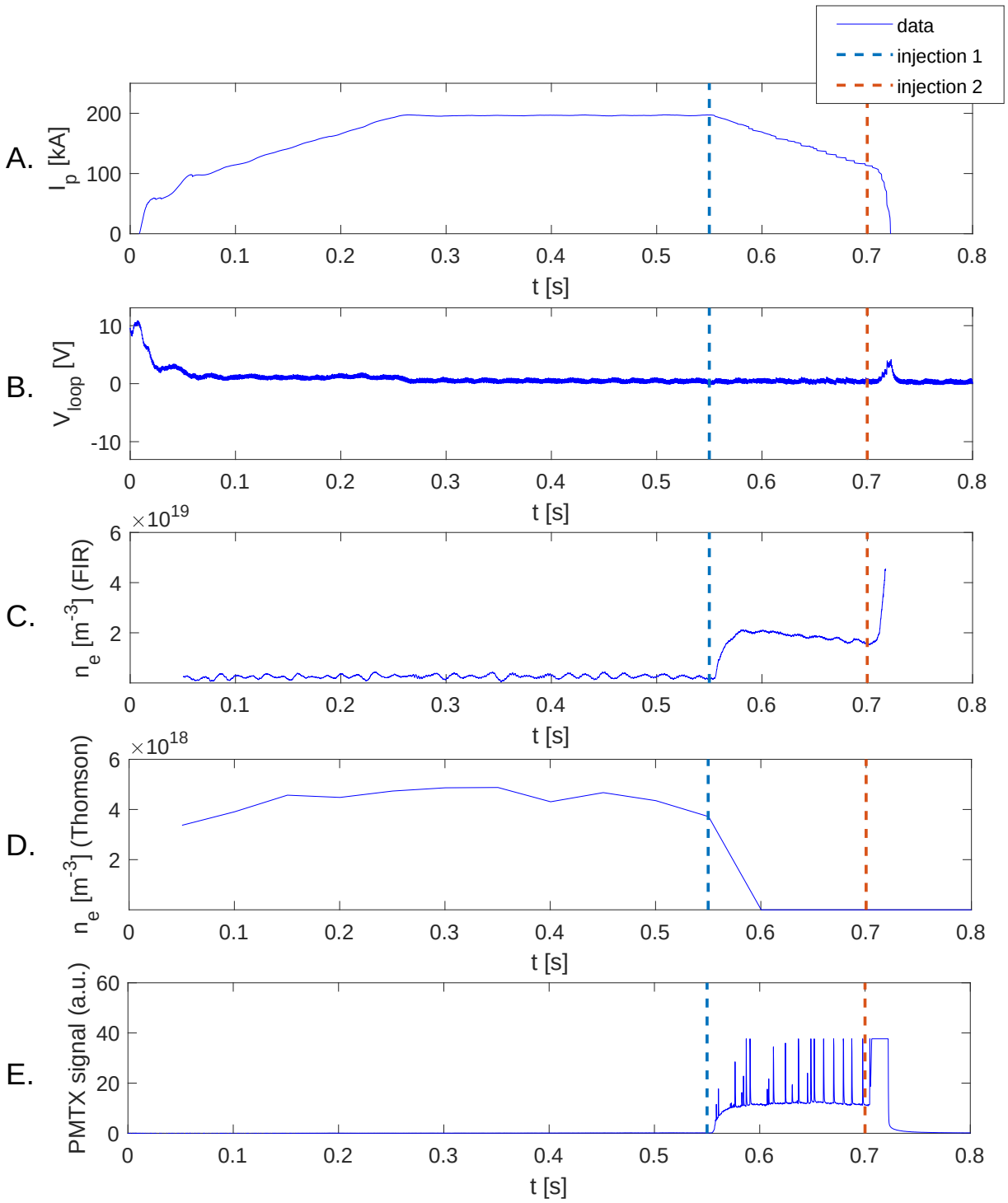

Figure 4.1: Various diagnostic readings for TCV runaway shot 63433, exemplifying the experimental TCV RE scenario. Ne (1.3 bar, 5 ms) is injected into a D plasma at 0.55 s to cause a disruption and trigger conversion of the current to the runaway regime by means of the avalanche effect. A large amount of Kr (5.0 bar, 20 ms) is injected at 0.70 s to kill the runaway beam. A) plasma current, B) loop voltage, C) average electron density at $R = 0.903$ m measured with the FarInfraRed (FIR) interferometer, D) electron density at $R = 0.900$ m, $Z = 0.228$ m, determined using Thomson scattering, E) PhotoMultiplier Tube for hard X-rays (PMTX) signal.

Chapter 5

Multispectral systems and data processing

As a basis for the experimental work with MultiCam presented in chapters 6 and 7 the principles behind multispectral systems treated here. MultiCam and the MANTIS systems operate using the same camera hardware and software, but differ the manner in which light is distributed amongst different cameras. The most recent developments in the line of multispectral systems are treated by discussing the design of MANTIS+. This new lightweight system has all benefits of the optical cavity based MANTIS system, but the flexibility of a smaller device making it the number one candidate for the potential extension of multispectral runaway systems in the future. The description of MultiCam rests on that of MANTIS+.

Apart from understanding the system used for RE experiments, it is of importance to detail the latest calibration and tomographic inversion procedures which allow quantitative imaging. In doing so, uncertainties in the pixel readout values are acquired. In this work the gap between uncertainties in raw images and emissivity profiles is bridged through an error propagation study, allowing a first time assessment of emissivity profile errors.

5.1 Multispectral systems

5.1.1 Design of MANTIS+

The basic principle behind the MANTIS and MANTIS+ systems was described in section 1.4. In the current section attention will be devoted to the most important technical specifications of the new system. This includes a description of the components, an overview of the hardware and data management and an assessment of the specifications in terms of resolution and acquisition rate. A more detailed description of the filters used is deferred to section 5.2.1.

The different components in MANTIS+, and the way in which images are formed onto the cameras, can best be addressed following the path of light through the system. An optical relay is placed in front of the transparent window belonging to the port on which the system is installed. Light from the tokamak is directed towards the box entrance via two mirrors. An overview of the cavity in the form of CAD drawings is provided in figure 5.1.

At the entrance, the main lens (A) projects an image onto the camera at the other side of the cavity. Here light is incident on a narrowband optical interference filter (B) behind a relay lens, where a selected wavelength section is transmitted. Most of the other light in the 400 to 800 nm range is reflected. The transmitted light reaches a camera (C), whose sensors detect the incoming photons. The cavity has a length of 400 mm. This value was chosen in accordance with optical ray tracing calculations by the TCV team using the ZEMAX software [72]. The factors setting a lower bound on this value are the minimum camera separation, the light ray to filter angle and the filter curvature. As will be discussed in section 5.2.1, the use of large filter inclinations and surface bending compromise the transmission at the right wavelength and sharp imaging. Decreasing cavity size is therefore not deemed desirable. For the chosen depth, the central beam to filter surface normal angle is fixed at 3°. The half-angle of the light cone between the main lens and the filter surface is 2.3°.

Reflected light is focussed just in front of a mirror (D) at the other end of the cavity. This is achieved through a relay lens with a focal length slightly smaller than this dimension. The concave mirrors have a twice as small focal

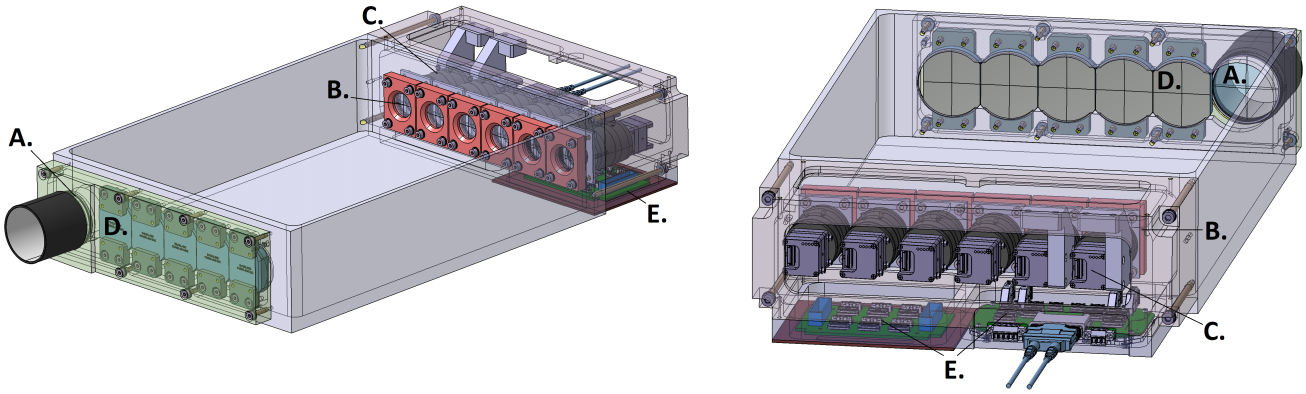

Figure 5.1: Front and rear view of MANTIS+ cavity CAD drawings. A: main lens at cavity entrance B: filter holder C: camera with relay lens D: mirror E: hardware. Image with courtesy of J.D. Landis.

length, so that the reflected light from the image projected on the first filter will reach the adjacent filter. The reason why the light is not focussed precisely onto the mirror is that this would cause a large amount of scattering in case a surface imperfection is targeted. Light intensity in the imaging range is preserved well, as the Thorlabs dielectric coated mirrors have a reflection coefficient above 0.99 in the 400 to 750 nm range.

The superior performance in terms of light retention is the primary argument for using mirrors instead of relying on a beam-splitter based system. Given the fact that one might wish to image a set of weak emission lines, multispectral imaging benefits strongly from such a configuration. Furthermore, large photon fluxes allow for short camera integration times and thus high temporal resolution. The downside of this approach is that it is more challenging to get the image degradation from channel to channel to a level where it is not the limiting factor in the spatial resolution.

Different than for the adjustable MANTIS system the relay lens, filters and cameras are fixed in their position. This design decision is justified by the relatively small cavity size. As compared to MANTIS, errors are magnified by a factor 2.5 less in MANTIS+. The fixed configuration reduces alignment time and improves system reliability through the use of less moving components. The main uncertainty in the optical configuration is the filter surface orientation. This is as these components are replaceable, and minor deviations in glass orientation with respect to the filter retaining ring can occur. A first order estimate of the effect of such an error can be obtained using ray transfer matrices in the 1D paraxial beam approximation [73]. The intended angle of incidence is denoted θ_{in}, the filter inclination with respect to the desired position is θ_{error}, L is the cavity length and r_0 is the radial distance of the ray under consideration to the optical axis of the mirror. Using transfer matrices for the path of the ray to the mirror, the modification of its direction at the curved mirror with approximate focal length $L/2$, and lastly the path from the mirror to the second filter, one gets:

$$\begin{bmatrix} 1 & L \\ 0 & 1 \end{bmatrix} \begin{bmatrix} 1 & 0 \\ -2/L & 1 \end{bmatrix} \begin{bmatrix} 1 & L \\ 0 & 1 \end{bmatrix} \begin{bmatrix} r_0 \\ -(\theta_{in} + 2\theta_{error}) \end{bmatrix} = \begin{bmatrix} -r_0 \\ -(\theta_{in} - 2\theta_{error}) \end{bmatrix}.$$

Note that the position of the ray on the second filter is not modified by errors in the ray to filter angle, but the incoming angle for this ray onto the next filter is. An offset in the second filter which matches that of the first one will correct this error. Mirrors can be rotated 360 degrees in their holders, which has the practical implication that tilting errors can be corrected for using an error in the next channel. Of course such a practise is undesirable in terms of calibration efforts, which are intended to be minimal for this system. The maximum angle offset can be calculated by enforcing a maximum displacement from the desired position of each ray on the mirror. This error term r_{error} is given by:

$$r_{error} = L\Big(\tan(\theta_{in} + 2\theta_{error}) - \tan(\theta_{in})\Big). \tag{5.1}$$

Realizing that the cone of light itself has a finite angle, so that the maximum intended angle of incidence is 5.3°, and setting an upper limit on the displacement on the mirror of 1 mm, the maximum angular deviation is found to be 0.07°. The upper bound on the displacement has been chosen based on the size of the mirror. Experiments with the filter retaining rings show deviations are expected to be in the order of 0.03°, which is safely below the

threshold. Note that angular deviations also have an effect on the transmission wavelength of interference filters. This effect will be quantified in section 5.2.1.

A second possible source of error deserving some attention are chromatic aberrations which can occur in the used lenses. Since the index of refraction of a material is wavelength dependent, by a phenomenon called optical dispersion, the focal length of a lens is a function of this parameter as well. Although differences are expected to be minor, they can build up if the imaging system is sufficiently large. The mirror configuration of the MANTIS system however counteracts such effects, as the image is rotated by 180 ° between each channel.

A last observed degrading effect in MANTIS images treated here is ghosting. The light reflected off the filter can originate from different layers inside this dielectric, depending on the way it has been fabricated. A ray of light which reflects on the second layer in such a stack, will emerge at the surface a slightly different position than one which has been reflected at the first interface. The image formed on the next filter in line will thus be a superposition of the desired image and a slightly displaced, usually much dimmer, version of that same image. The presence of ghosting has implications for the order in which the interference filters are placed. A first guiding principle in picking this order is to start with the weakest lines on the first channels and place the very intense ones in the last positions. This ordering can be critical as light retention is not perfect due to incomplete reflection of the light outside of the filter transmission band. Recording a weak emission line in one of the last channels may lead to low photon fluxes and a poor time resolution, or even not being able to observe significant signal at all. For image quality reasons not all filter orders perform equally well. It is has been observed that ghosting effects are especially large if two adjacent filters transmit well in neighbouring spectral regions [27].

The potential sources of image degradation described here have been brought to a minimum level for MANTIS+. Tolerances in the design are such that the threshold for angular uncertainties is not reached. Furthermore, ghosting has become negligible with the use of custom designed highly reflective filters.

5.1.2 Data acquisition and processing

Now that the imaging of light onto the camera sensors has been been described, the data collection is treated. This includes a brief overview of the hardware and computer-camera communication procedure. A comprehensive treatment is given by Perek et al for the MANTIS system [27]. MANTIS+ operates in an identical fashion on this front.

The demands based on which hardware and software design decision have been made are threefold. Firstly, since studied line intensities can vary by orders of magnitude, it is rewarding to optimize the data acquisition details per individual channel. The MANTIS and MANTIS+ systems should be capable of making adjustments on a real-time basis. Camera gain and exposure time must change over the duration of the shot to match changes in emission intensity. Secondly, the system should be capable of resolving steep gradients in the emission profile, therefore an upper limit of 5 mm in spatial resolution is demanded [27]. This determines the pixel size of the camera sensors which can be used. Thirdly, the delay between frame acquisition by the camera and its availability on a central computer for control purposes should be minimized. Any time spend on transferring and reading-out data will be lost for real-time analysis. Real-time in detachment control context means faster than 2 ms [28].

To satisfy the criteria above, while also limiting the expenses made on the system, the choice for the cameras has fallen on the Ximea MX031MG-SY-X2G2-Fx with Sony IMX252 sensors. The latter consist of 2064 by 1544 pixels of size 3.45 by 3.45 μm, and have a dynamic range of 70.9 dB. Bit resolutions of 8, 10 and 12 bits per pixel are supported by the camera, along with a wide range of exposure times from the μs to second scale. The gain is adjustable in the 0-24 dB range. Sensor quantum efficiency is above 45 % in the 400 to 700 nm range, and shows a steep drop below this window. From 700 to 900 nm there is a nearly linear decrease from 45 to 10 %. These specifications are delivered by a 26.4 by 26.4 mm camera, keeping the cavity size limited.

All six data streams are managed from the MANTIS+ side by a XiSwitch. Collected frames are sent to an external motherboard via an optical cable, where they are fed directly to the RAM without CPU interference. The motherboard hosts enough cores to assign one to each individual camera stream. Furthermore, one core is solely dedicated to communication with the cameras, one operates a real-time Linux kernel and two more are available for tasks related to data aggregation, control algorithms and linking with the central TCV digital control system. Cameras and triggers are managed by a hardware interface code which also controls frame delivery, saves data to a storage and communicates with control system. Details on the hardware and software involved can be found in the article by Perek et al [27].

If the photon flux in the studied spectral interval is sufficiently high, the factor limiting the acquisition speed is the camera sensor readout time. The used sensors allow a high degree of control over the procedure used in reading

out the collection of pixels. Flexibility in this regard does not only benefit control engineering studies, but is a valuable property when studying plasma dynamics as well. Pixels are read out in a line-by-line manner. The MANTIS+ optical relay rotates the image such that this occurs in the radial direction of the poloidal plane. In the z-direction adjacent columns can be binned in pairs of 2 to increase acquisition speed. Furthermore, the reading procedure can be limited to a pixel selection which contains all information of the region of interest in the camera view. This limits image size and thus the time needed to obtain the frame data. Note that the readout time also depends on the used pixel depth, making 8 bit the preferred option for fast acquisition. Depending on the choice of values for the parameters described above, maximum frame rates are normally above 400 Hz and can reach up to well over 1 kHz. When the acquisition is constrained not by the readout time but by the photon flux, as is the case for weak emission lines, frame rates can typically still be kept above 200 Hz.

5.1.3 MultiCam

The system used for the experiments described in this work is the MultiCam system. This imaging system formed the starting point for multispectral studies at TCV and the development of the more advanced MANTIS line of systems. Its use in current studies is motivated by its limited size and weight which allow installation on the middle port, the low alignment demands as compared to MANTIS and the possibility of swapping filter in between shots. The cameras, filters and data acquisition hardware used for MultiCam are exactly as described for the MANTIS+ system.

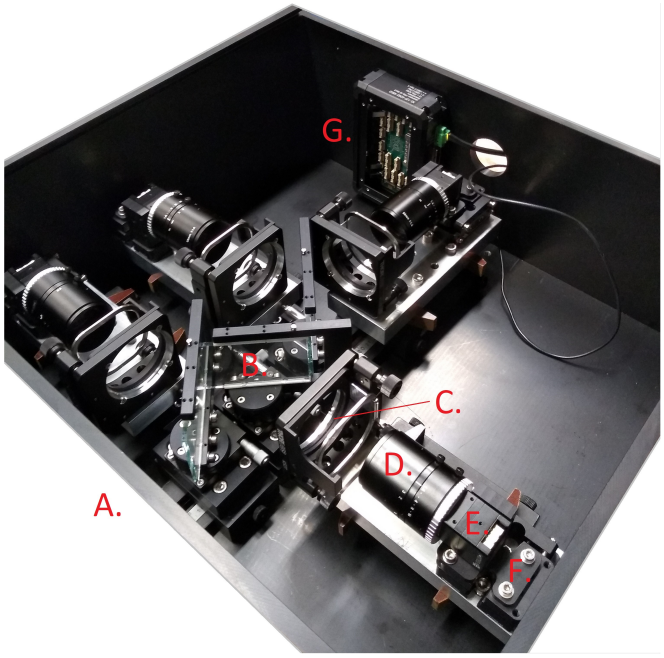

Figure 5.2: MultiCam setup showing the A: connection to relay optic, B: beam splitters, C: filter holders, D: objectives, E: cameras, F: adjustable 5-axis camera stage and G: XiSwitch which regulates the connection to external computers.

The difference between the MANTIS systems and MultiCam lies in the optical design of the box, which for MultiCam is beam splitter based as shown in figure 5.2. Light enters the box (A) via a straight relay optic without any mirror components. The intensity is distributed amongst four channels with the use of beam splitters (B). Accumulated intensity at the last channel is one fourth of that at the first one. This difference is leading in the choice of filter positions. Filters are positioned in Thorlabs holders (C) in front of camera objectives (D). The focus of each camera depends on the filter choice and is calibrated before installation on the tokamak using a checkerboard reference. The detectors themselves (E) are borrowed from the MANTIS system so that the existing data acquisition framework can be used. Optical alignment mainly occurs through the 5-axis stages (F) on which the cameras are placed. The XiSwitch (G) regulating the data stream is positioned at the back of the system.

MultiCam specifications relevant for this work are listed in table 5.1. The inversion quantities are clarified in section 5.4.

Table 5.1: Overview of MultiCam and inversion specifications for experiments presented in this work.

feature	specification
pixels [px]	1032 x 772
pixel size [μm]	3.45 x 3.45
bit depth ADC [bit]	12
saturation level ADC	4096
acquisition rate [Hz]	200-1000
spatial inversion resolution [mm]	1-5
relative inversion uncertainty	$10^{(-0.81\pm0.02)\epsilon+(12.9\pm0.4)}$

5.2 Interference filters and spectral line selection

5.2.1 Optical interference filters

Given the central role of optical filters in the MANTIS+ system and its performance, special attention is devoted to these components. Interference filters are the logical choice for this type of application, as they can be made to reflect most of the light which is not transmitted, and can be crafted to be very selective in the wavelengths which they transmit.

Interference filters transmit light based on the operating mechanism of Fabry-Perot cavities. Suppose a light wave enters a dielectric slab with reflective mirror surfaces as illustrated in figure 5.3 for a single ray. The ray is bend toward the surface normal as the refractive index n_1 of the material is higher than that of free air, denoted as n_0. At each encounter with one of the surfaces a fixed portion of intensity is transmitted while the rest is reflected, so that the ray bounces back and forth inside the dielectric.

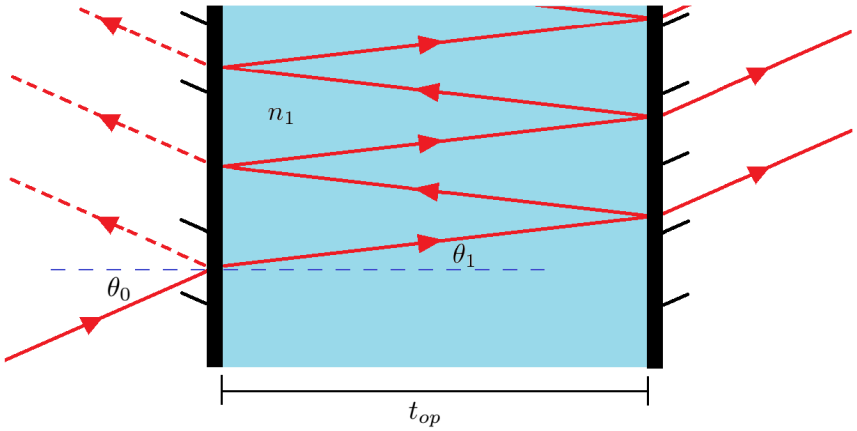

Figure 5.3: Principle behind an interference filter. The cavity consists of a dielectric with reflective surfaces. An incoming wave is fully transmitted if the cavity width equals an integer amount of half wavelengths.

Now consider the case of a light beam reaching the surface in a perpendicular orientation. One would expect the ray intensity to drop at each internal surface encounter due to partial transmission. Taking into account that in reality the travelling light is a wave, an interesting effect occurs if the optical thickness of the cavity t_{op}, which is the width times the refractive index of the material, equals an integer amount half-wavelengths. The phase of the wave attains exactly the same value after one round trip through the cavity, and the individual contributions add up so that a large amount of power bounces between the mirrors. Part of this intensity is lost at each mirror interface. The light transmitted back through the first mirror cancels the principle reflection, being the light which has not entered the cavity at all. This is because the two contributions are out-of-phase. At the same time the light lost from the cavity at the second mirror, depicted on the right in figure 5.3, has an accumulated intensity equal to that of the beam incident on the first mirror. As a result light satisfying the resonance condition for the wavelength $\lambda_{T,0}$ [74]

$$\lambda_{T,0} = m\frac{\lambda}{2}, \tag{5.2}$$

where m is an integer, will be fully transmitted through the cavity. Other light is mostly blocked and reflected back.

The angle under which the light falls upon the first mirror alters the optical path of the ray in between the mirrors. Calculating the added path length, taking into account wave refraction, the modified transmission wavelengths are

$$\lambda_T = \lambda_{T,0}\sqrt{1 - \left(\frac{n_0}{n_1}\right)^2 \sin^2(\theta_0)}, \tag{5.3}$$

where θ_0 is the angle of incidence. Since the angle of incidence influences the transmitted wavelength, it is one of the design criteria specified to the manufacturer of a filter.

Another experimental parameter which should be taken into account when designing the cavity is the operation temperature, which is known to affect the refractive index of the material. Over small ranges this dependency is approximately linear. Also, material expansion can occur, which has an effect on the optical thickness of the different layers. The combination of the two effects influences the transmission wavelength [75]. Note that the problem is marginal when hard-coated filters are used.

The principles treated here lay at the basis of interference filter functioning. Commercial filter compositions and the filter performance specifications which are to be taken into account when designing filters for multispectral systems are summarized in appendix D.

5.2.2 Spectral line selection

Emission lines chosen for specie identification have to satisfy several criteria. First of all, the line should be strong in the sense that the measured light intensity at this wavelength should be as large as possible. This will guarantee an optimal signal to noise ratio, suffering little from continuous background radiation of accelerating species. Secondly the line should be visible in the spectrum and clearly correspond to a transition recorded in literature. In this way a high level of certainty about the origin of the emission is secured. The values from literature are obtained from the NIST database [76]. A third criterion is related to the camera sensor sensitivity. As mentioned in section 5.1, the sensors have a limited wavelength range in which the quantum efficiency is of appreciable magnitude. This limits the range for line selection to roughly the 400 nm to 950 nm portion of the electromagnetic spectrum.

Lastly, for the contribution of a line to be clearly separable from its neighbour the two should not be space too closely. This adjacent line can have its origin in the same specie, or in intrinsic TCV impurities C, O, N and He. At high temperatures the dominant restricting factor is the width of the lines, which is mainly dominated by Doppler broadening $\Delta\lambda_{FWHM}$ [58]:

$$\Delta\lambda_{FWHM} = \sqrt{\frac{8k_b T_i \ln(2)}{m_i c^2}}\lambda_0, \tag{5.4}$$

where T_i is the ion temperature, m_i the ion mass and λ_0 the central emission wavelength. The effect is mainly pronounced for heavy impurities at high temperatures. Singly ionized He will for instance only be present in the plasma up to about 10 eV according the Corona equilibrium equations. At such an ion temperature the shift for a 587.6 nm emission line is only 0.072 nm. At pre-disruptive 1 keV operating conditions, Ar^{16+} lines will have a FWHM between 0.15 and 0.29 nm in the 400 to 750 nm central wavelength range.

The factor which imposes harsher restrictions on the distance by which two lines must be separated is the filter bandwidth. This value is determined by wavelength shifts which are expected based on the misalignment between the normal to the filter surface and the incoming light. For a filter of refractive index 1.45 and transmission wavelength of 750 nm at a central angle of incidence of 3°, the maximum angle of incidence 5.3 ± 0.03 gives a wavelength shift of 1.43 ± 0.01 nm according to equation (5.3). For a refractive index of 2.05 this reduces to 0.72 ± 0.01 nm, and shrinks with decreasing wavelength. From this last upper bound estimate it is found that a high refractive index filter at the low frequency end of the spectrum requires a filter FWHM of at least 1.4 nm. Emission lines suitable for detection should not have strong neighbouring lines within the wavelength dependent filter FWHM.

The ranges used for the detection of synchrotron radiation also have to meet several criteria. First of all, the transmission wavelength needs be in the sensitive range of the camera. As was argued in chapter 2.5.1, the synchrotron radiation is TCV is not expected to show a great intensity in the visible. The best chance to detect

this contribution to the spectrum is to place the filters at near IR wavelengths. In this there is a trade-off between camera sensitivity on one hand and emission intensity and the spread in detection range on the other. The last refers to the fact that making quantitative statements on the runaway distribution from the synchrotron spectrum is more accurate when the three filter ranges are well-separated. Another criterion to take into account is that the chosen range should not have strong polluting lines clouding the spectrum. In this work these criteria are satisfied through a choice of filters with a 10 nm FWHM around 800, 905 and 950 nm.

5.3 Image processing

Assuming toroidal symmetry of the plasma, characteristic plasma parameters are often expressed as a function of the R, z-coordinates introduced in section 2.3. To relate the intensity data from the camera to the emission in such a coordinate system, several processing steps are required. The procedure used in this work is detailed in this section. The steps include a calibration of the camera position, correction for lens distortion, incorporating imaging details such as the gain and exposure time, removing X-ray counts and performing a tomographic inversion to arrive at the 2D emission profile.

5.3.1 Camera calibration in Calcam

With the goal of performing a tomographic inversion in mind, one needs to have an accurate geometric model of the imaged system and knowledge of the camera position. A software program with the purpose of spatially calibrating cameras is Calcam [77]. Making use of a single image made with the camera which ought to be calibrated and a CAD model of the imaged system, this Python package can be used to tell one what the coordinates and distortion of the camera in the model are. The user can do so by matching points visible in the image to ones on the walls of the tokamak CAD model. For TCV an accurate model is available which means that MultiCam can be spatially calibrated via this method as well.

To objective is to relate the pixel position (x_p,y_p) of features in an image to a position in real space (x_c, y_c, z_c) in the camera frame of reference. In this frame the camera is positioned in the origin and views along the z-axis. The default CAD model coordinate system has its origin in the center of the torus. A point in the camera frame of reference $\vec{r}_c$, is related to one in the default system $\vec{r}$ through a translation vector $\vec{R}$ and rotation matrix $\mathbf{T}$:

$$\vec{r}_c = \mathbf{T}(\vec{r} - \vec{R}). \tag{5.5}$$

These quantities are provided by Calcam after performing the calibration. The other calibration information is related to the image distortion. First of all, normalized coordinates (x_n, y_n) are introduced to deal with perspective projection:

$$\begin{pmatrix} x_n \\ y_n \end{pmatrix} = \begin{pmatrix} x_c/z_c \\ y_c/z_c \end{pmatrix}. \tag{5.6}$$

Radial and tangential distortions are incorporated via a perspective distortion distortion model. Introducing radial and tangential distortion coefficients $C_{r,1}, C_{r,2}, C_{r,3}$ and $C_{t,1}, C_{t,2}$ respectively, one can relate the normalized coordinates to the distorted normalised coordinates (x_d, y_d) via:

$$\begin{pmatrix} x_d \\ y_d \end{pmatrix} = (1 + C_{r,1}r_n^2 + C_{r,2}r_n^4 + C_{r,3}r_n^6) \begin{pmatrix} x_n \\ y_n \end{pmatrix} + \begin{pmatrix} 2C_{t,1}x_n y_n + C_{t,2}(r_n^2 + 2x_n^2) \\ C_{t,1}(r_n^2 + 2y_n^2) + 2C_{t,2}x_n y_n \end{pmatrix}, \tag{5.7}$$

where r_n is defined as $r_n = \sqrt{x_n^2 + y_n^2}$. The distorted normalized coordinates are directly linked to pixel coordinates via a camera matrix. Its components describe the image projection using the effective focal lengths f_x and f_y in perpendicular directions and the pixel coordinates of the centre of the perspective projection on the sensor, denoted as c_x and c_y. The matrix equation is given by

$$\begin{pmatrix} x_p \\ y_p \\ 1 \end{pmatrix} = \begin{pmatrix} f_x & 0 & c_x \\ 0 & f_y & c_y \\ 0 & 0 & 1 \end{pmatrix} \begin{pmatrix} x_d \\ y_d \\ 1 \end{pmatrix}. \tag{5.8}$$

Defining some restrictions on the distortion coefficients and focal lengths used, Calcam uses the matched CAD and image points to provide the best solution to the set of equations (5.6), (5.7) and (5.8). An example is shown in figure 5.4. The resulting coefficients contain all information on the camera position in the CAD model, estimated focal lengths and the distortion coefficients. These can be used for the ray tracing efforts which will be described in section 5.3.4.

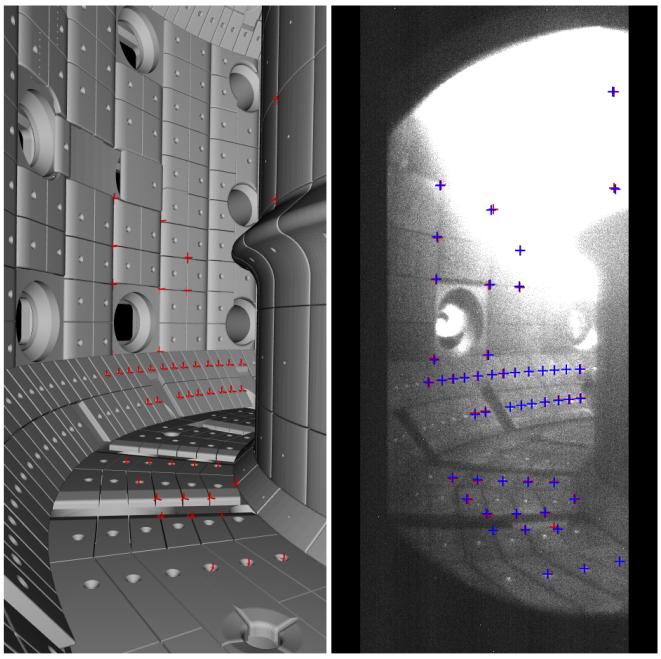

Figure 5.4: Example of user input for point fitting camera position and distortion in the Calcam software. Points in the CAD model contour of the tokamak are linked to features in the image [77]. The MANTIS image on display was taken on a TCV lower port using a D_β filter.

Calcam offers a set of tools to check the accuracy of the camera position fit. The points selected in the CAD model can be re-projected onto the actual image for comparison with the points which the user placed there. Also, the wireframe of the CAD model can be overlayed on top of the image for a robust visual check of the fitting results. A quantitative indication of the accuracy is provided in the form of a root mean square fit residual. In generating MANTIS camera calibrations the upper bound is taken to be 2.0 pixels. This threshold is normally achievable and ensures that the spatial uncertainty is not dominated by the camera calibration.

5.3.2 Intensity calibration

Bit depth correction

Conversion from raw data to photon counts starts with a correction for the offset level of the camera, which depends on the bit depth. The bit depth is equal to 8,10 or 12 depending on what analogue to digital converter is used. For the work described here 12 bit is the default value. The offset level is found by scanning the dark edges of image. Saturated pixels can be found from the saturation level

$$saturation\ level = 2^{bitdepth}.$$

Absolute intensity calibration

The next step is to calibrate the pixels for the sensor sensitivity at different photon energies, filter transmission and vignetting effects. Every calibrated image pixel im_{ij}, where i and j are pixel indices, relates to the original image $im_{raw,ij}$ via

$$im_{ij} = \frac{F_{corr,ij}\ im_{raw,ij}\ aperture^2}{gain(t)\ exposure(t)}, \tag{5.9}$$

where the exposure and gain are frame dependent and $F_{corr,ij}$ is a calibration factor which transfers pixel readings to photon counts. Variations in the conversion factor from pixel to pixel are dominated by optical and spectral vignetting. The first effect is due to light rays being lost at the edges of optics, yielding a gradual degradation of intensity towards the edge of the image. The second effect is due to emission line dependent variations in the transmission factor over the filter surface, due to a varying angle of incidence of the incoming light.

To construct the calibration factor calibration measurements are performed. A lab sphere with known spectral radiance $\epsilon(\lambda)$ is used to cover the MANTIS field of view with a uniform light source. The light is recorded and pixel medians in time are taken to construct a calibration image with pixel values $im_{cal,ij}$. Note that this image has been corrected for the gain and exposure used in this calibration experiment to get readings in intensity per unit time. To construct an intensity to photon mapping, the total amount of photons from the calibration sphere which have passed through the filter per unit time, is divided by the calibration image and an effective transmission factor $T_{r\ effective,ij}$:

$$F_{corr,ij} = \frac{1}{im_{cal,ij} T_{r\ effective,ij}} \int_{\lambda} \frac{\epsilon(\lambda) T_r(\lambda)}{hc} d\lambda, \tag{5.10}$$

with h the Planck constant and $T_r(\lambda)$ the filter transmission curve.

The effective transmission factor is there to correct for non uniform filter transmission. As indicated in formula (5.3), the location dependency of the light to surface angle will cause a variation of the transmission curve over the surface. The effect on the percentage of light allowed trough depends on the wavelength of the recorded line. The correction procedure providing the effective transmission is performed using a spectral lamp emitting the line under consideration. A labsphere is used to uniformly fill the optics with light at the corresponding wavelength. The recorded image is first corrected for optical vignetting using the labsphere calibration described before. The resulting profile is in essence a map of the transmission factor if the peak value is equated to the measured peak transmission of the filter, resulting in a pixel dependent effective transmission $T_{reffective,ij}$. This does require that the peak wavelength falls within the region of finite transmission, as should be the case for appropriately designed filters.

5.3.3 Filtering out and counting runaway X-rays

Before performing the final inversion from camera image to 2D emission profile, it is occasionally necessary to remove 'snow' from the images. These white dots can be seen in figure 5.5. There is strong evidence that these are caused by X-rays which are incident on the sensors, as the snow is only seen during runaway shots. Also, the white pixels are distributed homogeneously over the sensor, including the parts which are not exposed to light from the tokamak. When runaway confinement is lost, the electrons are incident on the wall components. The immediate deceleration leads to Brehmstrahlung in the hard X-ray regime for these highly energetic particles. These photons turn up as high intensity counts on the camera images, as the vessel and MultiCam components form no obstacle.

An example of an image from the pre-injection phase is shown in figure 5.5 A. Clearly, the procedure of extracting emission profiles at the desired wavelength is obstructed by the X-rays. During runaway experiments an additional filtering step is thus required. Assuming that the X-rays snow is distributed randomly over the pixels, and covers less than half of the image, one can resort to a median filtering technique. Here each pixel value is recalculated as being the median value of a rectangular neighbourhood of specified size. In the resulting image, the outlier X-rays do not show up any longer as illustrated in figure 5.5 B. Note that employing this filter, the position of details in the emission pattern can be modified. If the filter size is limited to a 3 by 3 square neighbourhood the introduced uncertainty is in the order of one pixel.

Filtering out the snow interestingly enough offers a new pathway for gathering information on X-ray formation. The number of outliers per video frame can be counted and tracked over time. Median filtering introduces a deviation of pixel values between the original and filtered image. A histogram binning the pixels according to these difference values reveals a distribution which peaks around 0 difference. There is however a clear group of outliers. These individual points contain the X-ray noise data, and allow for counting snow instances. A lower bound on the difference between the original and filtered pixel value should be satisfied before an intensity recording is classified as snow. Since X-rays correspond to strongly positive difference values, the absolute value of the most negative points in the distribution is chosen as a bound. This ensures that all regular deviations to the positive side are not recorded as being X-rays.

For a proper comparison with other hard X-ray detectors, one should consider the possibility of two X-rays being recorded by a pixel during the same integration period. For a collection of N_p pixels and N_{counts} snow counts, the

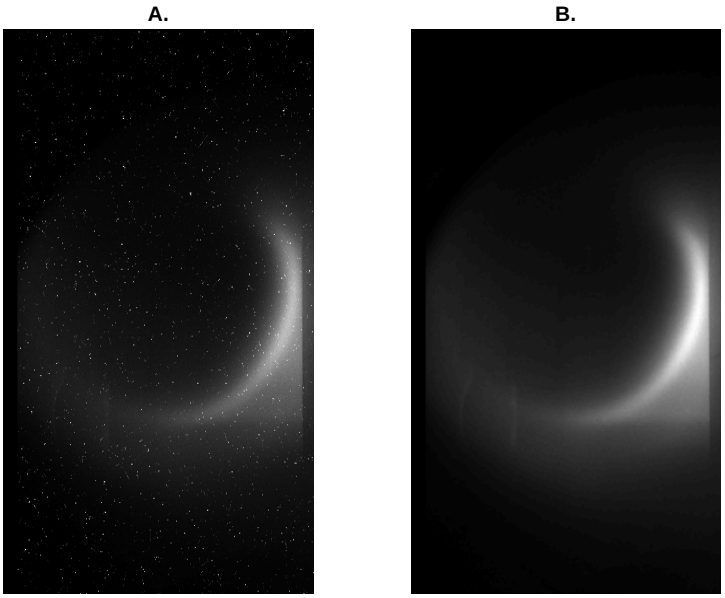

Figure 5.5: MultiCam frame acquired during runaway shot 64722 with a CIII filter. A.) Unfiltered image, note the randomly scattered white pixels. These saturated points show up whenever runaways are lost from the beam, and are believed the originate from X-rays which are formed upon RE impact on the wall. B.) Image after median filtering has been applied. These filtered images serve as input for the inversion procedure.

expectation value for the total amount of hits N_x is [78]:

$$N_X = N_p \sum_{i=1}^{N_{counts}} \frac{1}{N_p - i + 1}. \tag{5.11}$$

This assumes that each sensor pixel has an equal chance to detect an X-ray in a given time interval. The distribution has a standard deviation of:

$$\sigma_{N_X} = \Big(N_p \sum_{i=2}^{N_{counts}} \frac{i-1}{(N_p - i + 1)^2} \Big)^{1/2}, \tag{5.12}$$

which is not negligible compared to the shot noise. The shot noise varies little over the probability distribution of N_X calculated using equations (5.11) and (5.12), so that to good approximation the standard deviation is the sum of the shot noise and the contribution from equation (5.12). Single channel relative uncertainties in the X-ray counts are typically in the range of 0.019 ± 0.007.

As an example the X-ray trace, constructed using images of a 667 nm filter, has been plotted for shot 63397 in figure 5.6 A. During the experiment impurities are injected at 0.47 s, after which significant runaway production occurs. The trace indeed shows no recorded snow before the initial disruption time and starts to build up after the injection. Another characteristic moment which can be seen clearly in the figure is the final disruption, during which the X-ray noise on the camera recordings peaks strongly. After this moment in time the counts drop to zero, with the exclusion of an occasional incidental reading. These are an artefact of the method used to set a bound for the snow counting. To distinguish such incidental counts from actual X-ray recordings it is important to always relate observations to the original camera recordings.

The analysis of different channels provides similar X-ray results. Magnitudes of the signals differ, but the ratio between the traces is distributed around a fixed number with a relative uncertainty of around 0.2. When the data is available, results are averaged over the different channels. The discrepancy does pose an extra, and the main, source of uncertainty in the X-ray counts.

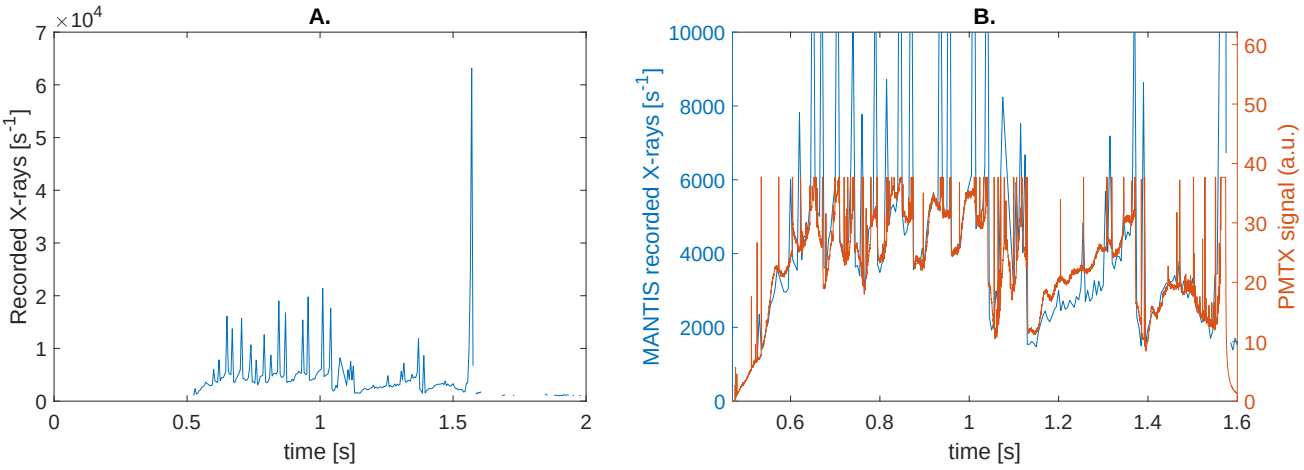

Figure 5.6: X-ray counts for shot 63397 on channel 6, as determined with equations (5.11) and (5.12) from the snow in the raw images. At 0.47 s impurities are injected into the plasma and significant runaway production occurs. A.) X-ray counts per second as a function of time. B.) Comparison between MANTIS snow and PMTX data, zoomed in at the PMTX dynamic range.

As a test for the quantitative accuracy of the X-ray detection method, MANTIS snow recordings are compared to the voltage reading of the hard X-ray detector PMTX. In figure 5.6 B, the signals are compared. Both clearly show a sudden onset of X-rays when the impurities are injected. This is a strong indication of runaway formation. The general trends in the signals show a strong similarity. Outside of the burst events, which turns up in the data a sudden spikes, the ratio between the two signals has a value of $(1.5 \pm 0.2) \cdot 10^2$, which amount to a relative uncertainty of 0.13. This falls within the uncertainty range of the X-ray counts in the MANTIS data.

Recursive spike appearances at frequencies above 200 Hz are not distinguished in the MANTIS readings due to the limited time resolution. The PTMX clearly performs better in this sense with a 5 kHz sampling rate. Snow analysis of MANTIS images however has its own advantage. During large bursts PMTX readily saturates, whereas the detection method highlighted in this section has a clearly better dynamic range. One critical note has to be made here, as the used method only works if less than 50 percent of the image is covered with snow pixels. If this boundary is exceeded the median filtering will not see these recordings as outliers and the validity of the analysis breaks down. This situation is normally not encountered but can yield misleading quantitative results for short highly intense bursts, so that these instances have to be treated cautiously. This does not take away that the method presented here can be of added value during quantitative comparison of current losses to runaways hitting the wall whenever PMTX saturates.

5.3.4 Tomographic inversion

Having filtered out undesired features from the image, and having corrected the image for the gain, exposure and intensity calibration, all preparations for performing the image inversion are in place. Images such as the one in figure 5.5 B are not yet in the final form which one wishes to study. Exploring the behaviour of impurities or a runaway beam, one ideally works with toroidally symmetric emission profiles in the R,z-plane. Every pixel intensity value of an image has contributions from emission sources at various radial and height positions. The technique explained in this section to decouple these contributions falls in the domain of tomographic inversions. Essentially, a planar spatial distribution is inferred from a collection of line integrated emissivity values.

The mathematical problem can be expressed in matrix form. A R,Z-emission pattern defined on N_s numbered toroidally symmetric radiation sources is stored in a vector $\vec{x}$. This quantity can be mapped to a pixel brightness vector $\vec{b}$ with a length equal to the amount of pixels. The entity linking the two is the so called geometry matrix, with elements A_{ij} [79]:

$$\sum_{j=1}^{N_s} A_{ij} x_j = b_i. \tag{5.13}$$

The geometry matrix component A_{ij} contains the length which a straight ray, cast at pixel i in the viewing

direction, traverses through emission source j. Calcam offers the tool to cast these rays once a camera calibration has been performed [77]. The software returns the start and end points of each ray, from which the direction vector can be inferred. Geometry matrix calculations are performed for every unique pair of camera calibration file and 2D inversion grid of interest. These grids define either rectangles or squares, which are the poloidal cross sections of an annulus of constant emission which run around the torus. For every ray the extend in R, z-space is determined, and the ray intersections of the 3D emission source boundaries are computed. For straight rays Pythagoras theorem is applied to find the total ray length through the cell. The results are stored in a sparse matrix which is beneficial for the computation time and avoids running into memory problems.

Note that for a tokamak with reflective walls, adopting the above method can result in strong inversion artefacts. This is the result of emission being allocated to positions on the wall where no actual source exist. Corrections for this can be implemented through more intricate ray tracing methods, but is expected to be of little influence to the results obtained for TCV which has carbon tiles [80]. More room for improvement is found when considering the ray width. For a non-perfectly collimated detector, the ray method becomes less representative moving away from the camera. Especially in regions with strong emission gradients, such as the divertor, errors in the order of 10 % are to be expected [81]. For the current study, in which the core plasma is of main interest, no significant improvements are expected to result from implementing rays of finite width.

Determining A_{ij} is not all there is to the reconstruction challenge. The inversion problem of finding $\vec{x}$ is generally ill-posed. Small errors in the experimental data, due to noise or calibration inaccuracies for instance, can lead to large mistakes in the reconstructed emission profile. A controlled conversion towards a solution of the system and regularization tricks can help to significantly reduce this problem as will be addressed below [82].

The procedure to retrieve $\vec{x}$ used in this work is a form of the Simultaneous Algebraic Reconstruction Technique (SART), which aims at solving a consistent system of linear equations. It does so by iteratively applying corrections to the reconstructed emission profile based on an error term proportional to the difference between the measured intensity values and the forward reconstruction of it, computed using $\vec{x}^{(k)}$ of the current iteration step [79]. The magnitude of the modification, and thus the solution convergence speed, are governed by the relaxation parameter λ_r.

Knowledge of the physical system can help further improving the inversion result through regularization. Here, additional boundary conditions on the smoothness of the solution are implemented. The final form of the recursive solving procedure is [81]

$$x_j^{(k+1)} = x_j^{(k)} + \frac{\lambda_r}{\sum_{i=1}^{N_p} A_{ij}} \sum_{i=1}^{N_p} \frac{A_{ij}}{\sum_{j=1}^{N_s} A_{ij}} (b_i - A_{ij} x_j^{(k)}) - O_j^{(k)}, \tag{5.14}$$

where N_s the amount of cells on the inversion grid, representing a discretization of the source. The smoothness operator $O_j^{(k)}$ is of an isotropic 2D discrete Laplacian form. Essentially it introduces a penalty for steep gradients in the emission profile;

$$O_j^{(k)} = \beta(N_{b,j} x_j^{(k)} - \sum_{n=1}^{N_{b,j}} x_n^{(k)}), \tag{5.15}$$

with $N_{b,j}$ the amount of cells adjacent to inversion cell under consideration and n a summation index for these neighbours. On physical grounds, each negative grid emission value is forced to zero in between the iterations k. This is as no region is expected to show net absorbing behaviour. The SART procedure is terminated once the norm of the relative difference vector $|x^{(k+1)} - x^{(k)}|/|x^{(k)}|$ has reached a pre-set value. The exact criterion follows from a trade-off between the result accuracy and computation time and is typically fixed at $1 \cdot 10^{-2}$.

An additional detail of the inversion procedure which should be mentioned is related to lenses in the MANTIS relay optics. As figure 5.4 shows, part of the real image is obscured by this optical component. This feature of the system is not incorporated directly in the calibration. Therefore, the obscured region is interpreted as a part of the vessel with absolutely no light emission. Emission patterns resulting from subsequent inversions show strong non physical artefacts. A straight forward correction is applied by finding the obscured pixels, and setting entries of the corresponding rows in the geometry matrix to zero.

5.4 Accuracy of reconstructed emission profiles

Throughout the outline of the data gathering and processing methods described above, various sources of uncertainty in the emission profile have been indicated. Proper physical analysis of the required data demands an estimate of the errors involved in this procedure, to the best of currently available knowledge. Especially in the case of runaway modelling, small changes in model input parameter can yield profound changes in the output. In this section the various sources of uncertainty are brought together.

5.4.1 Uncertainty in signal to photon conversion

Sensor signal uncertainty

To obtain uncertainties in the sensor signal, experiments and comparisons to manufacturer data sheets have been performed by the MANTIS development team. The results are specific to the sensor type used in this work, and an elaborate description is presented on the TCV wiki.

Readout noise is typically a function of the camera gain. This is the amplification factor for photo-generated electrons at the sensor. This source of error imposes an uncertainty in the amount of generated photo-electrons equal to

$$S_{readout} = 0.82 \cdot 10^{0.81 gain[db]/20}, \tag{5.16}$$

where gain in db is related to the voltage amplification factor V_{out}/V_{in} as:

$$gain[db] = 20 \log_{10}(\frac{V_{out}}{V_{in}}).$$

Sensor to sensor variation in this noise level is typically an order of magnitude smaller than the mean noise level itself.

Next, consider the shot noise, which is the direct result of the discrete nature of photons. The amount of detected photons per time interval follows Poisson distribution with its corresponding standard deviation $\sqrt{N_{ph}}$, where N_{ph} is the number of generated photo electrons per integration time. Taken into consideration the conversion gain k_{gain}, which is the amount of electrons generated per photon, the shot noise uncertainty in the obtained signal becomes

$$S_{shot} = k_{gain}\sqrt{N_{ph}}. \tag{5.17}$$

The gain factor has a value of 0.38. Note that relative shot noise in a camera device decreases with the amount of recorded photons N_{ph} as $1/\sqrt{N_{ph}}$. Increasing integration time and maximizing light intensity at each camera reduces this source of uncertainty. The latter is one of the main benefits of a mirror based system.

In previous experiments it was found that the total signal noise can not be described using solely the readout- and shot noise. An additional non-linear term is required;

$$S_{non-linear} = c_{gain}\Big(\frac{N_{ph}}{k_{gain}}\Big)^2, \tag{5.18}$$

where the factor c_{gain} was found to depend on the gain as:

$$c_{gain} = -9.73 \cdot 10^{-8} gain[db]^2 + 1.52 \cdot 10^{-7} gain[db] + 1.25 \cdot 10^{-4}.$$

To combine the uncertainties above, the square-root of the sum of their squares can be taken. This total uncertainty as well as its three contributing components are shown as a function of photo-electron counts in figure 5.7. The upper-bound on the output signal has been chosen to match the saturation value.

Subfigure A displays the situation in which there is no amplification of the sensor signal. Note that the readout noise is only a significant contribution to the total noise at low light intensities. For most of the signal range the noise is dominated by the shot noise. The non-linear contribution comes into play near saturation, preventing the

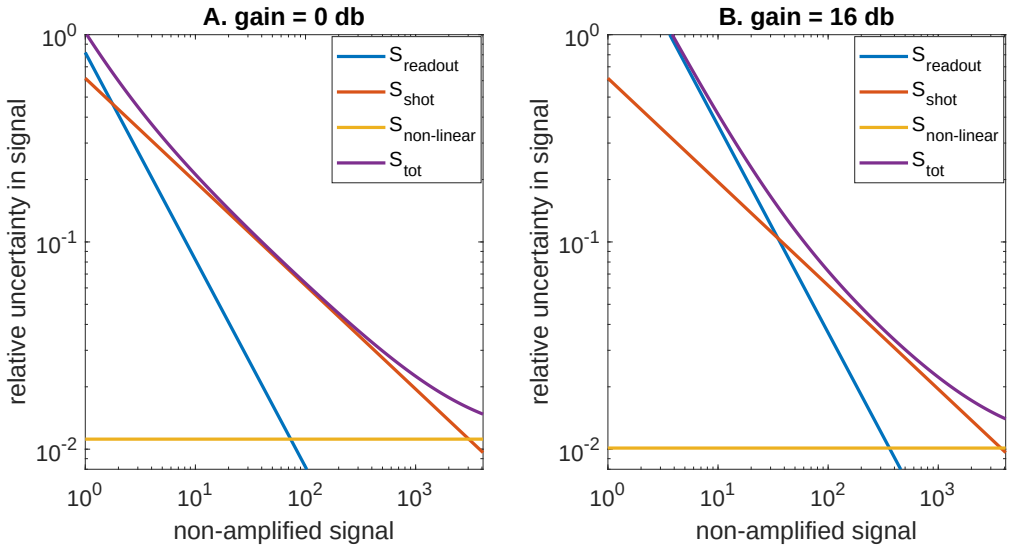

Figure 5.7: Relative uncertainty, based on 1-sigma intervals, in the camera sensor signal as a function or photoelectron counts per integration time. The total relative uncertainty, as well as the contributions of the readout-, shot- and non-linear noise are displayed. A) no signal amplification. B) 16 db signal amplification.

total relative noise form dropping below 1.5%. Furthermore, note that the relative uncertainty in the pixel values drops below 10% once signals exceed around 1% of the saturation signal. This gives an indication as to what levels of pixel signal can be relied on in a quantitative analysis of emission profiles. Error propagation in the inversion process will be discussed in the next section. For higher gains the readout noise starts playing a larger role as the signal is amplified. This raises the signal at the 10% relative error threshold by a factor of 1.5.

The effect of finite emission line widths

With the calibration for spectral vignetting incorporated, prior uncertainties in the local transmission factor are corrected for. This calibration procedure is however performed using a line with a width set by the spectral lamp characteristics. Line emission from the tokamak plasma will have a different line width due to influences of the local plasma parameters such as temperature, density and magnetic field.

To make an estimate of the upperbound of the resulting uncertainty, the effect on the transmission of D_α is studied for ion temperatures between 0 and 3 eV. The upperbound is chosen based on the Coronal equilibrium estimate of the temperature required to fully ionize a population of hydrogen atoms. Using an experimentally obtained transmission curve for a Balmer alpha filter and a Doppler broadening dominated emission line, it is found that the effective transmission varies by a factor of $7 \cdot 10^{-5}$ over this temperature range for an incidence angle of the light equal to 2°. In case the central wavelength is closer to the edge of the filter the situation changes, as local transmission gradients of the filter are higher. For a 4° angle, the uncertainty raises significantly to $3 \cdot 10^{-3}$.

The effect grows in importance with the spread of temperatures over which one could observe some emission line. In imaging highly ionized states of high Z impurities an accurate evaluation of the uncertainty in the photon flux on the sensor requires an evaluation of the expected spread in the effective transmission factor.

Unquantified sources of uncertainty

Not all sources of uncertainty have a known magnitude. The light entering the optical relay has had to pass through an optical window in the tokamak port. While designed for this purpose, depositioning of metal layers onto the window during tokamak operation can reduce the transmission. Over the wavelength range spanned by a single, broadened line this difference is expected to be negligible. For absolute calibration of the total signal magnitude, the constant transmission factor at the studied wavelengths will have to be determined. Such an experiment has to date not been performed. In computing line ratios, variations in transmission over the spectral range introduces uncertainties of unknown size.

A second unknown with similar effect of yielding a constant uncertainty factor over all pixels, is the error in

labsphere calibration. No pixel to pixel variations are expected, but a non-uniform correction factor over the visible range does translate into an uncertainty in computed ratios. Calibration by the manufacturer or with the use of another, newly calibrated sphere would be the most effective way of reducing the overall uncertainty in computed line ratios. On the basis of experience within the MANTIS project, only a conservative estimate of a relative error equal to 0.10 can be made.

5.4.2 Uncertainty in tomographic inversions

In the previous section the various contributions to the uncertainty in multispectral images have been discussed. A question which remains unanswered, is how these errors propagate to the output of the tomographic inversion procedure which has been described in section 5.3.4. This problem is not straight forward, as there is no mathematical expression linking the images directly the inverted profiles. Here, a new approach to getting an estimate of the error propagation is presented.

The statistical method described here assumes that all pixels have an uncorrelated Gaussian probability distribution at each point in time. A set of N new images is constructed by choosing a random value from every pixel value distribution. The standard SART algorithm is applied to each of the new images, generating N inversion profiles. For every cell on the inversion grid an equally large number of sample values are thus available, for which the mean and the standard deviation are computed. As such an analysis is time consuming, given the large amount of inversions, the aim identify trends in the scaling of the relative uncertainty with the local emissivity.

An example of a camera image and emissivity profile obtained during the MST1 campaign is used to illustrate the procedure. For a hollow emission tube at the D_{alpha} wavelength, pixel to pixel uncertainties are obtained using equations (5.16) (5.17) and (5.18). Figure 5.8 shows the original image, mean of the 100 reconstructed emissivity profiles and the spread in emissivity value for two cells on the emission tube. The Gaussian like spread of the obtained values allows for a clear interpretation of the standard deviation in the emissivity. A plot showing the relative uncertainty for all cells as a function of the local emissivity is shown in figure 5.9 A. There is a clear negative correlation, which on a double logarithmic scale appears to be of a linear nature. A linear-least-square fitting procedure results in slope estimates of:

$$\begin{aligned} \log_{10}(\frac{\sigma\epsilon}{\epsilon}) &= c_{\epsilon 1}\epsilon + c_{\epsilon 2} \\ c_{\epsilon 1} &= -0.81 \pm 0.02 \\ c_{\epsilon 2} &= 12.9 \pm 0.4. \end{aligned}$$

The drop-off in the error is even stronger than that in the shot noise of the original image. For the cell of highest emissivity, the relative spread is estimated to be in the range of $4.6 \cdot 10^{-3} - 2.9 \cdot 10^{-4}$. For the pixel of highest intensity the calibrated image the relative uncertainty is equal to $1.5 \cdot 10^{-2}$, and thus at least a factor of 3 larger than that in the emissivity. This is believed to be the result of the fact that a large number of random fluctuations in pixel values average out in terms of their contributions to the far fewer number of emissivity cells in the iterative correction steps of the SART procedure.

5.4.3 Spatial resolution

The best achievable spatial resolution is set by the pixel size, device dimensions, binning factor and region of interest. The emission element dimension below which further reduction will not yield an improvement of resolution, is determined using the distance between an optical relay entrance and a resolution board required to obtain a sharp image. Taking into account the field of view and the number of camera pixels a resolution of 1 mm is found for the current camera configuration. A triangular emission grid with this resolution covering the whole poloidal cross section would require over a million emission elements, exceeding the typical grid size for reconstructions on a single cpu by a factor of 100. Spatial resolution of the emissivity output is thus limited by the computational power available rather than the number of pixels on the camera.

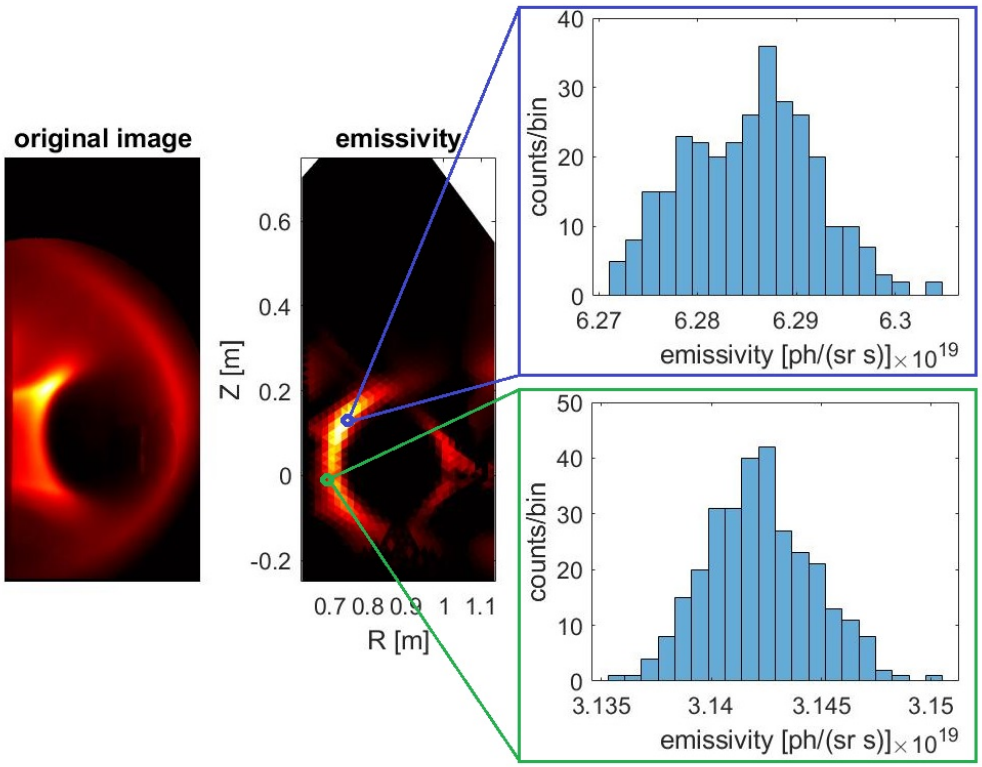

Figure 5.8: Hollow D_{alpha} emission profile alongside its tomographic inversion obtained using the SART method from equation (5.14). For two emissivity cells the Gaussian like spread in values corresponding to the uncertainty in the original image are shown.

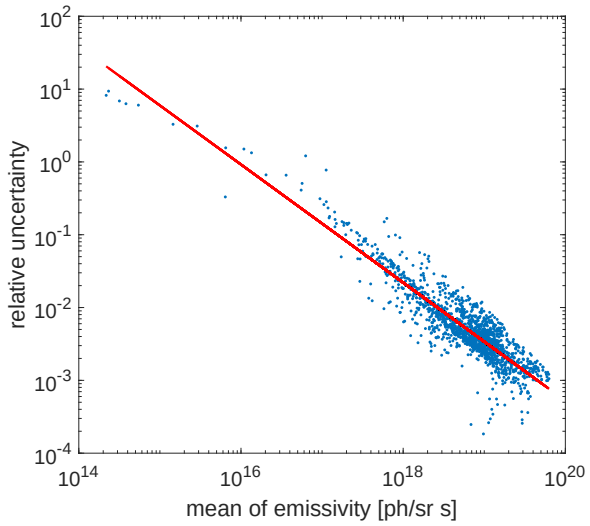

Figure 5.9: Reconstruction of relative emission cell uncertainty as a function of local emissivity for a hollow D_α emission tube. A linear fit on the double log scale is shown, satisfying $\log_{10}(\sigma\epsilon/\epsilon) = (-0.81 \pm 0.02)\epsilon + (12.9 \pm 0.4)$.

Chapter 6

Analysis of synchrotron radiation patterns in TCV quiescent scenarios

Comparison of (kinetic) runaway model output to experiments demands a means of tracking RE real- and phase-space dynamics. This chapter addresses experiments conducted to assess the potential of multispectral systems for fulfilling this demand. Despite the low magnetic field at TCV strong synchrotron emission is observed in the visible, as will be argued in section 6.1.

To infer information on the runaway distribution function evolution from the observations it is necessary to identify what part of real- and phase-space contributed to the observations. Two different complementary approaches are followed to this end. In section 6.2 the highly refined geometry of a test-case pattern is compared to super-particle SOFT output. Momentum, pitch angle and RE beam radius estimates are obtained. The second approach, presented in section 6.3, is of a spectral nature. Traditional spectrometer based distribution estimates are discussed, addressing the importance of taking into account the highly anisotropic nature of synchrotron emission in data interpretation. Novel 2D resolved spectral analysis techniques exclusive to multispectral systems are outlined and put to the test using TCV MultiCam recordings.

SOFT is not a full-orbit code and is yet to be benchmarked against such models. Validation of details in its behaviour can however also occur through comparison with experiments. A RE harbouring plasma is moved in the z-direction to assess how the geometry of synchrotron patterns changes. Using a time resolved magnetic reconstruction SOFT is capable of reproducing this behaviour accurately, as is shown in section 6.4, fortifying confidence in this widely used software.

Lastly, on the basis of the phase-space identification and attempt is made to unravel why synchrotron patterns are not observed in all shots. The experiments presented here suggest that the appearance of synchrotron patterns is (indirectly) linked to failure of post-disruptive beam formation. Possible RE production mechanisms which could populate the observed part of phase-space are discussed, along with energy limiting effects which could explain why the pattern intensity saturates. On the basis of the outcomes directions for more extensive kinetic modelling of the experiments are suggested.

6.1 Observation of continuum radiation from quiescent runaway beams

To assess whether synchrotron radiation can be observed in TCV RE experiments MultiCam is installed on a middle port with a tangential viewing direction. Quiescent as well as gas injection assisted disruption scenarios are imaged. The experiments in question use a circular plasma configuration with the magnetic axis 0.23 m above the detector. The pre-injection location of the plasma edge is visible on the deuterium Balmer filters, as shown on channel 1, 2 and 4 in figure 6.1, which displays emission recordings at 1.1 s into shot 64584. During this quiescent stage of the discharge an unexpected observation is made for a number of shots on camera channel number 3, which has filtered light in a narrow region around 640 nm as input. The phenomenon clearly manifests itself in shot 64584, again depicted in figure 6.1. After about 700 ms a blob of light appears in the center of the plasma. Saturation of the pattern intensity is reached within 300 ms, after which the observed structure remains constant until plasma disruption. The observation is striking because (i) none of the present species radiate at this wavelength, (ii) the shape of the light does not match the magnetic geometry, (iii) careful inspection of the other channels reveals that

the pattern is visible on all cameras, and lastly (iv) the Oceans spectrometers clearly record the Balmer lines but show no significant emission at 640 nm.

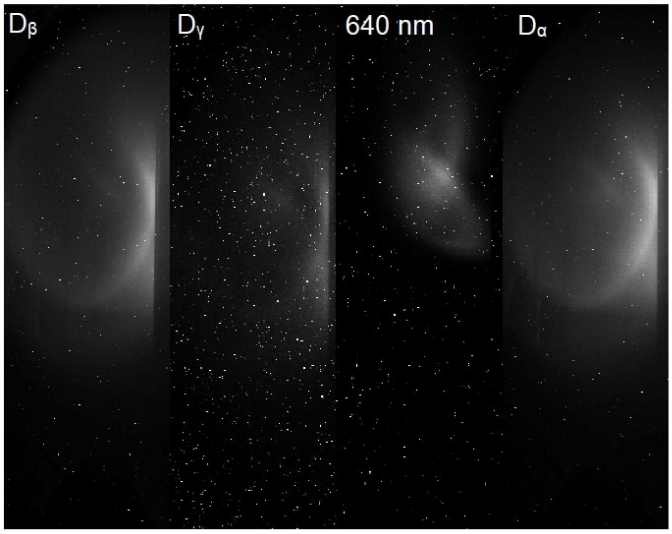

Figure 6.1: MultiCam recording for shot 64584 at time $t = 1.1004$ s. Channels 1,2 and 4 are equipped with Balmer filters and show the Deuterium emission at the edge of the hot plasma. Channel 3 has a 2 nm FWHM filter at 640.6 nm central wavelength. No atomic emission is expected at this wavelength and continuum radiation is clearly visible.

X-ray snow on the acquired data gives away the presence of runaways in the plasma. Synchrotron radiation therefore comes forward as a likely source of the continuum. The directional nature of the emission can cause this form of radiation to avoid detection by the spectrometers, while still appearing on MultiCam which faces the electrons head-on. The explanation requires more verification as TCV has a relatively low magnetic field. At the pre-set 1.43 T, little radiation is expected in the detection range of the visible light camera, as was discussed in section 2.5.1. Significant emission at the 950 nm sensitivity cut-off is only reached for highly energetic electrons at large pitch angles. As explained in section 2.5.2, predicting the camera response to synchrotron emission is however a non-trivial undertaking and modelling is needed to assess whether the observed pattern can originate from the combination of the known magnetic configuration, detector specifications and a realistic estimate of the electron distribution function.

The recorded emission only appears in a sub-selection of the runaway shots performed, and occurrence of the pattern even varies between experiments which are intended to be identical. Knowledge of what underlying mechanisms cause this difference is of importance for reproducibility of TCV RE experiments, and could shed light on RE phase-space dynamical processes. Before delving into the differences between these shots it is important to get an indication of what part of electron phase-space is actually observed. This problem is addressed using geometrical and spectral methods in the coming sections.

6.2 Geometrical comparison using SOFT

6.2.1 Estimating the momentum of observed particles

The quiescent state of the plasma forms the ideal condition for using SOFT as a synchrotron radiation interpretation tool. As plasma parameters change slowly over time, the orbit discretization method is expected to be accurate. Simultaneously, under these conditions the availability of accurate magnetic reconstructions by the Grad-Shafranov solver LIUQE is guaranteed.

While the 640 nm filter was not installed with the intention of studying synchrotron radiation, the use of this narrowband filter has a few advantages. First of all, since no neon is injected before any of the patterns are observed, minimization of atomic emission pollution is ensured. Secondly, the low FWHM of the filter yields a

Table 6.1: Calcam camera calibrations results for MultiCam channel 3 used for the analysis of shot 64584.

pupil position	(1.082, -0.346, 0.014) m
view direction	(-0.855, -0.514, 0.072)
field of view	31.7 x 60.7 ° C
focal length	988 px
optical center	(317, 577)
distortion coefficients $(C_{r,1}, C_{r,2}, C_{t,1}, C_{t,2})$	(-0.1402, -1.3622, -0.0064, 0.0364)

uniform camera sensitivity over the whole observation range. Thirdly, as mentioned in section 5.3.1 clear vessel images are required for spatial and optical calibration of each MultiCam channel. In the shot range of interest numerous Ne injection experiments are conducted, so that a sufficient number of bright calibration images are available. This increases the level of confidence in the obtained camera position and image distortion, both important for interpreting the synchrotron data using SOFT. The camera parameters used here are summarized in table 6.1.

A first assessment of the observed region of phase-space and the sensitivity of the results to uncertainties in SOFT input and theory are presented here. More thorough inquiries into potential distribution function shapes and conditions for pattern observation are deferred to section 6.5. The test frame considered is obtained at 1.1 s into shot 64584 and is shown in figure 6.1.

To get an indication of what part of phase-space the light originates from, the product of the SOFT Green function (G) and Jacobian (J) for a 3 by 3 pixel region around the point of maximum intensity is shown in figure 6.2. Orbits at all minor radii inside the last closed flux surface have been incorporated. The red line indicates the region inside which GJ has a non-zero value. The obtained detector sensitivity function clearly sets some hard limits on the particles which could have contributed to the observed structure in the first place, as pitch angles below 0.33 and above 0.72 rad fall outside the detection range. Also, particles of normalized momentum exceeding 64 can not be observed. Sensitivity to synchrotron radiation increases with energy and pitch angle.

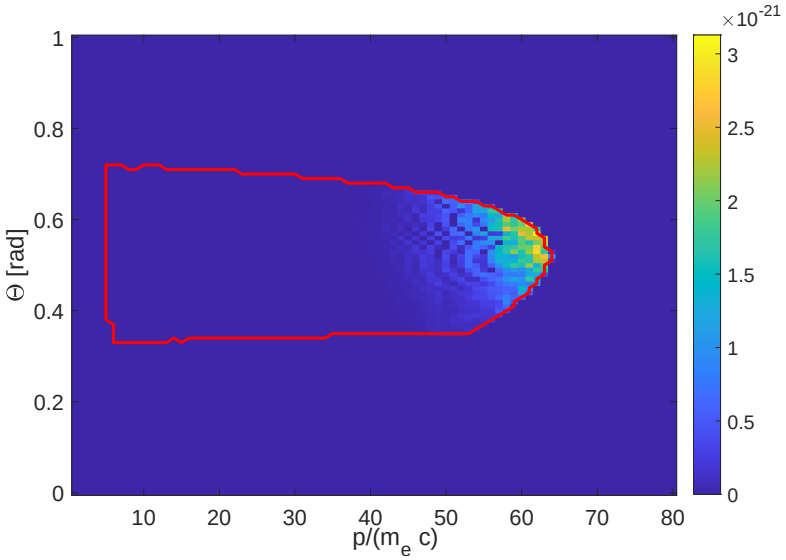

Figure 6.2: Normalized product of the Green function and Jacobian $p^2 \sin(\Theta)$ calculated using SOFT for TCV shot 64584 at 1.1 s. The detector calibration for the MultiCam camera channel with 640 nm filter is performed using Calcam. The selected image region of 3 by 3 pixels has been chosen to match the location of maximum intensity on the experimentally obtained synchrotron pattern.

Provided that GJf_e is sharply peaked around a certain value of (p, Θ), the shape of the synchrotron spot is well approximated by that generated by super particles of single momentum and pitch angle distributed equally over all radii [83]. To reduce the potential dominant momentum space, information from the whole image is used. Single particle images over the observable momentum range at a pitch angle of 0.6 are generated. Synthetic images for normalized momenta of 22, 47 and 60 are displayed alongside the real image in figure 6.4. These values were

chosen so as to most clearly show the effect of p on the spot shape and location. Although obtaining a matching synthetic image intensity distribution requires refinement of the electron distribution, the 47 $m_e c$ momentum particle produces a pattern that mimics that of the experimental result. The observed structure appears to consist of two separate surfaces of visibility, as shown in the topview of figure 6.3.

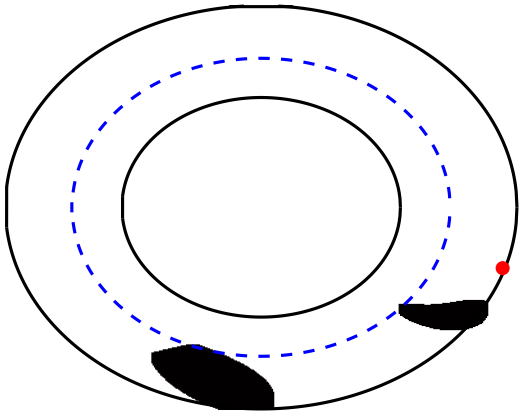

Figure 6.3: SOFT topview of surface of visibility for synchrotron radiation around 640 nm, originating from uniformly distributed electrons of normalized momentum 47 and pitch angle 0.6. A magnetic equilibrium reconstruction from shot 64584 at 1.1 s is used. The entire surface has been given the same color to show its full extend. The red dot indicates the position of MultiCam pupil.

For a normalized momentum below 24, the bottom lobe of light disappears behind the center column. Applying offsets to the detector position in the centimetre range does not affect this conclusion. If the detected part of phase-space would be below this limit, the high intensity region where the two lobes intersect would be placed against the center column. This is clearly not the case in the experiment. The momentum dependency of the geometrical shape also sets an upper bound on the dominant momentum. Beyond 54 $m_e c$, the lobes disconnect and no high intensity region of overlap is present. This same trend, although with different limits, is also observed at other pitch angles.

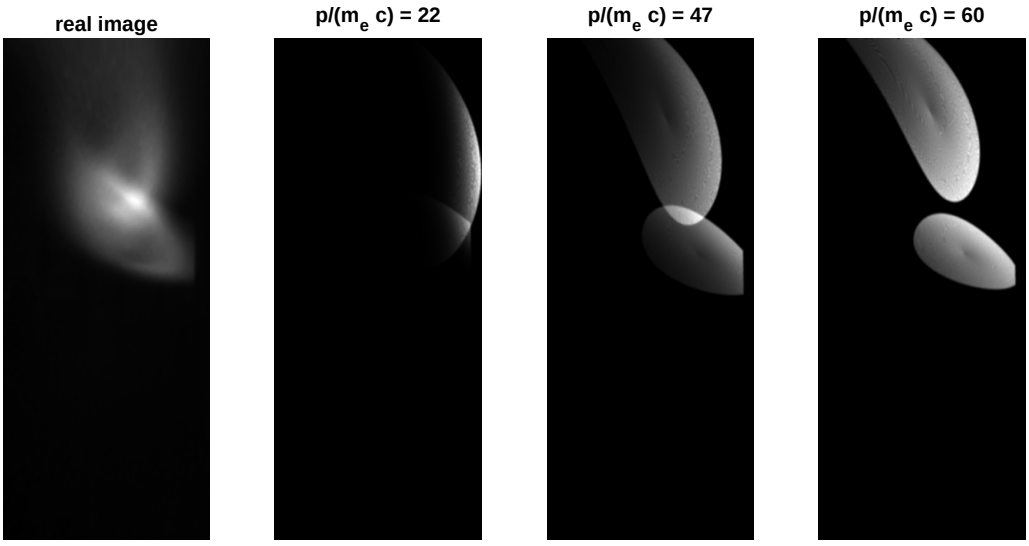

Figure 6.4: Synthetic synchrotron images for a single momentum and a pitch angle of 0.6 rad distributed equally over all radii. The results for momenta of 22, 47 and 60 $m_e c$ are shown alongside the experimentally obtained image.

Further constraints to the observed part of phase-space are found by matching the right edge of the overlap region in the synthetic output to that of the experimental footage. Since the edges of the spot are not clear cut in the experiment a rather wide range of possible values is considered. Edge positions between 375 and 410 pixels are used. Despite this large uncertainty, the high sensitivity of this geometrical factor to p results in a range between 45 and 53 $m_e c$ for a pitch angle of 0.58 and one between 37 and 48 $m_e c$ for a pitch angle of 0.44. Pitch angles below the latter result in multiple regions of lobe overlap, causing a large deviation from experimental results. For pitch angles above 0.60 rad the edge position falls outside of the range listed above.

The obtained bound on realistic dominant regions of phase-space allows for more focussed scans with a reduced computation time. A best match between the image and the SOFT output is sought for by (i) computing the root-mean-square (rms) error between the synthetic and real images after normalizing the maximum value to unity, (ii) calculating the distance between the image maxima, and (iii) calculating the absolute difference between two binary images with a threshold at 80 % of the maximum intensity. The first observation is that the vertical position of the overlap region at no point coincides with that in the experiment. Changes in the position of this region with p and Θ are mainly in the horizontal direction and can thus not account for the error. This mismatch could be caused by an inaccuracy in the equilibrium reconstruction or an offset in the camera position and distortion taken from the calibration. Errors in the latter especially affect the pattern at the edges of the image. A vertical shift of 27 pixels in the downward direction is required to get a synthetically reproducible location of the right side of the lobe intersection. This shift is adhered to below and revisited when studying the effect of perturbing the camera calibration and magnetic equilibrium on the (p, Θ) estimate.

For the shifted image, comparison results are shown in figure 6.5. The distance between the maximum of the synthetic and real image indeed mainly depends on the electron momentum as portrayed in B. Uncertainties in the camera calibration and its resulting mismatch in the overlap region position will therefore mainly affect the found best matching momentum. To take the size of the overlap region into account when comparing images, binary image matrices are generated by setting all pixel values above 80% of the maximum value to 1, and all other pixels to 0. The result is shown in sub-plot C. A best-match is found at a normalized momentum of 55, which is near the black line in figure B where the maxima positions match. The results in figure B however show a stronger pitch angle dependence, as the pattern shape does vary strongly with this parameter. For a momentum of 55 $m_e c$ an example is shown in figure 6.6. Moving from a pitch angle of 0.46 to one of 0.58 the upper lobe shifts upwards and intensity spreads more uniformly over the major radius. As a result the overlap region decreases in size, but the portion of it which exceeds the binary threshold increases. Since the experimental binary spot is in all cases larger than the synthetic one, the best pitch-angle match in sub-plot B is essentially the result of a peak in the product of overlap region size and the portion exceeding the threshold. A more realistic particle momentum distribution including contributions from a range of momenta could result in a spread of the high intensity region in the horizontal direction, and lead to a better fit.

Changes in pitch angle do not exclusively alter the overlap region, as also the orientation and intensity distribution inside the two lobes are affected. For smaller pitch angles the radiation is concentrated more towards the high field side as shown in figure 6.6. Sharp edges of the lobes with intensities comparable to that of the overlap region are predicted for pitch angles at the lower bound of the phase-space region of interest. To incorporate such information in image comparison the root-mean-square error between the normalized real and synthetic image is shown in figure 6.5 A. A clear local minimum in the error is found, and the best fit solution with $\Theta = 0.51$ and $p = 51\ m_e c$ is shown in sub-plot D. Note that the RMS does not increase quickly moving away from the maximum, which gives another indication that a superposition of single (p, Θ) is likely to produce better fits.

It is important to stress again that the best-fit values may be affected by inaccuracies in the camera calibration and magnetic reconstruction. As the unresolvable vertical offset has demonstrated such deviations are expected to be present. To assess the effect on the dominant (p, Θ) combination, an estimate of the uncertainty in the horizontal position of the overlap region is made. First, the calibration component is considered. Comparing the position of the center post in the real an synthetic image, a feature which was not used for the camera calibration, an error of 8 pixels is found. This exceeds the 1.9 pixel rms error provided by Calcam, which is likely the result of minor shot-to-shot camera movements. A viewing axis shift of 0.8 ° is sufficient to realize such an error, and is not deemed unrealistic given the fact that the MultiCam camera stand was not as rigid as desired during the discussed shot. In fact, comparison of frames from the same channel at the start and end of the first experimental week shows displacements in vessel details of comparable size to this shift. Translating the experimental image to the left and right by 8 pixels and performing the RMS comparison procedure again leads to a best fit of $\Theta = 0.51 \pm 0.01$ rad and $p = 52 \pm 1\ m_e c$. Estimating errors in the magnetic equilibrium reconstruction is more challenging. Taking an ad-hoc uncertainty equal to the vertical offset of 27 pixels, matching the observed vertical error, one obtains $\Theta = 0.53 \pm 0.02$ rad and $p = 54 \pm 3\ m_e c$. A shift this size corresponds to a shift in the magnetic axis of roughly

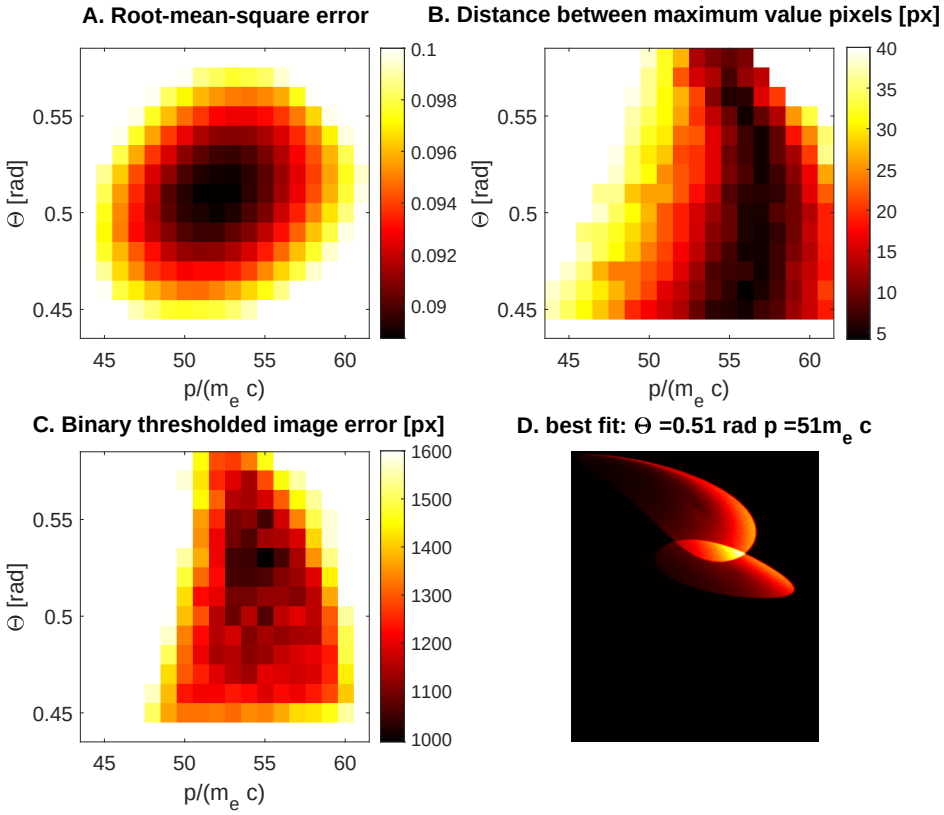

Figure 6.5: Comparison of single momentum, single pitch angle synthetic SOFT images to experimental results of shot 64584 at 1.1 s. Note that ceilings in the comparison values have been enforced for all results to enhance contrast in the region of interest. A) Root-mean-square error between images normalized to their respective maximum pixel reading. B) Distance between pixels which have the maximum value. C) Absolute difference between binary synthetic in real image. The binary images are created using a threshold equal to 80 % of the maximum value. D) Synthetic image corresponding to the lowest RMS error.

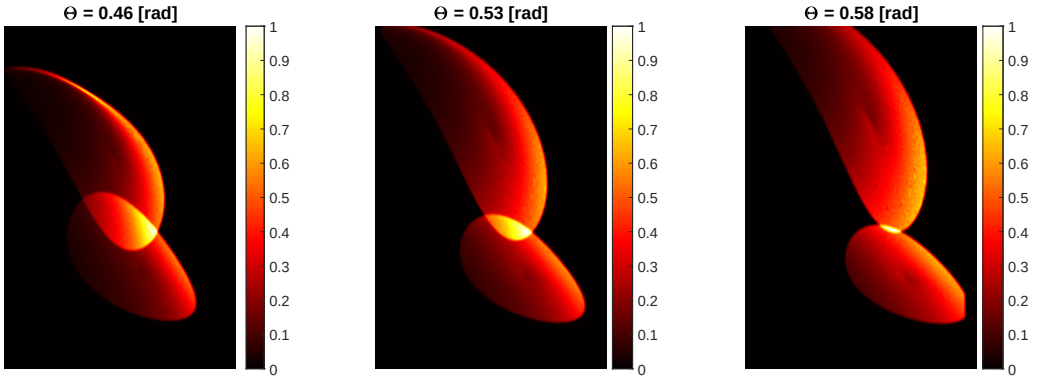

Figure 6.6: Zoom of synthetic synchrotron patterns for shot 64584, generated using a momentum of $p = 55m_ec$ and various pitch angle. While the position of the overlap region changes little with pitch angle, the overall pattern shape is greatly affected. Overlap region size decreases with increasing pitch angle, while intensity becomes less concentrated at the high field side.

30 mm. This was verified by shifting the magnetic equilibrium and recording changes in the location of maximum intensity of the synthetic pattern.

6.2.2 Constraining the runaway beam size

The achieved reduction in the potential dominant momentum-space allows for a first inquiry into the location of the observed electrons. SOFT allows a separation of contributions from particles at different minor radius in the Green function. Changes in synthetic pattern resulting from a limit on the maximum minor radius are portrayed in figure 6.7 for $p = 51\ m_e c$ and $\Theta = 0.51$ rad. The dominant effect of reducing the outer minor radius is a shrinkage of the projected size of the two separate surfaces of visibility. From the top view of the surfaces in the same figure it is evident that they remain centred around the same position, so that the size reduction is related to an actual decrease of the surface size. Below a maximum normalized radius of 0.78 the two lobes lose contact and the region of overlap, necessary for a reproduction of the experimental image, disappears. Note that this value does depend on the fit solution as a momentum of $p = 53\ m_e c$ and $\Theta = 0.52$ rad, derived from the bound on the camera calibration error estimate, gives a minimum required radius of 0.82.

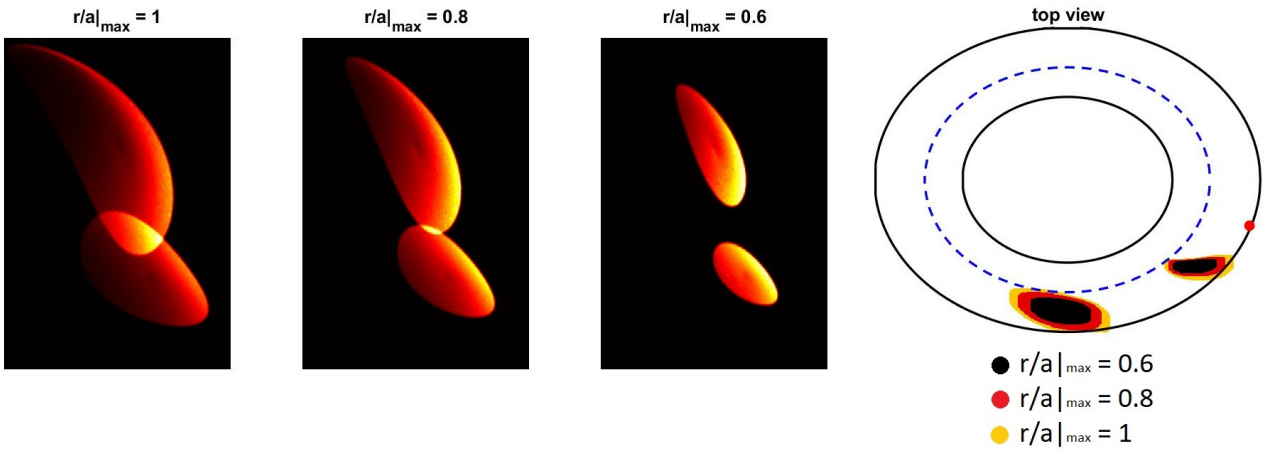

Figure 6.7: Synthetic synchrotron patterns from SOFT for shot 64584 at 1.1 s, generated using a fixed momentum of 51 $m_e c$ and pitch angle $\Theta = 0.51$ rad. The upper bound on the normalized minor radius of the test particles is varied. The dominant effect is a reduction of the size of the two surfaces of visibility. This can also be observed in the top view of the binary surfaces depicted on the right.

6.3 Phase-space estimates using spectral methods

Attention is shifted from matching experimental and synthetic images on the basis of geometrical features, to comparing the relative intensity of images obtained at different wavelengths. Methods proposed in this section are put to the test using data from the MST1 TCV campaign. Motivated by the patterns observed in the early phase of the campaign multiple synchrotron filters are installed on MultiCam simultaneously. In scenarios without neon puffing the narrowband 640.6 nm filter remains functional as a synchrotron filter and a useful reference channel with clear calibration images. Two additional filter have a relatively large FWHM of 10 nm to realise a higher signal to noise ratio. Central wavelengths are at 950 and 800 nm where little line emission is expected, which is confirmed by the Ocean spectrometers.

The frames treated here concern shot 64711 at 0.7036 s. The experimentally obtained shapes are depicted in figure 6.8. After the patterns have fully developed the runaway beam is moved in the vertical direction for a geometry dependence scan which will be discussed in section 6.4. As is to be expected for an emission peak at wavelengths exceeding the detection range, the peak intensity in the image falls off with decreasing wavelength.

6.3.1 Limits of synchrotron spectrum fitting

The most frequently employed method for extracting information on the electron distribution from synchrotron emission, is through slope fitting procedures. Using theoretical shapes of the spectrum, such as equation (2.28), information on the runaway population is inferred from spectrometer data by finding a best match with the forward modelled emission from a set of potential distributions. It is known that the distribution leading to a single spectrum is not unique, and using a single momentum and pitch angle fit may yield misleading interpretations [24]. Here this point is revisited, introducing the additional complicating factor of the highly anisotropic nature of synchrotron radiation. As will be shown the result (i) is non-conclusive in pitch angle and momentum and (ii)

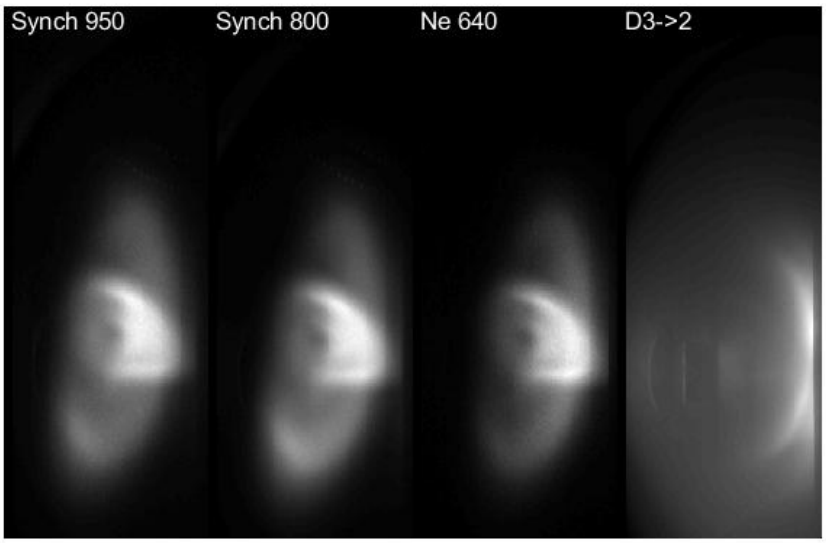

Figure 6.8: MultiCam images taken at 0.7036 s in shot 64711, where a quiescent runaway beam is moved up and down in the vertical direction. The first three channels show a synchrotron emission pattern.

depends on the spectral range of the spectrometer. The most important result is that the inaccuracy of the super particle method is not just due to an unrealistic shape of the distribution function, but also due to the fact that the complex nature of the emission geometry is neglected.

Degeneracy of super particle synchrotron slope fitting

In the super particle approach one assumes a fixed p and Θ with the aim of deriving statements on the dominant part of the electron distribution function. As mentioned when treating SOFT in section 2.5.2, the probed part of f_e need not be the most populated part due to the anisotropic nature of the emission. Constraining the observed part of phase-space can still be of value, but the single momentum approach turns out to be non-conclusive in the case of slope-fitting.

As a demonstration, the equilibrium from shot 64711 at 0.7036 s is used to generate synthetic spectrometer output for a system having the same field of view as MultiCam. Intensities at 950 and 640 nm are computed for super particles in the momentum range from 1 to 80 $m_e c$ and pitch angles between 0 and 1 rad. The results are depicted in figure 6.9, where contour lines are displayed. For a given experimentally obtained ratio there is a line in phase-space matching the synthetic output. Local slopes thus provide a space of solutions rather than a single estimate. One might hope to constrain the solution space using multiple local slope values. However, as will be shown below, light in the infrared is dominated by a different part of phase-space rendering such an intersection method inaccurate.

The influence of the Green function on spectrometer recordings

Single momentum estimates of electron distributions are, besides non-conclusive, also dependent on the spectral range of the spectrometer. This is demonstrated using an electron distribution function of the avalanche like form of equation (2.6.2). The parameters d_1 and d_2 have been chosen based on an RMS best-fit procedure for the experimental image:

$$f_e = \frac{f_0}{\cos(\Theta)p} \exp\big(-0.17\cos(\Theta)p - 0.37\tan(\Theta)\sin(\Theta)p\big). \tag{6.1}$$

Furthermore, the electrons are assumed to be uniformly distributed over the minor radius. In figure 6.10 the product of the Green function and electron distribution is shown for accumulated synthetic images constructed

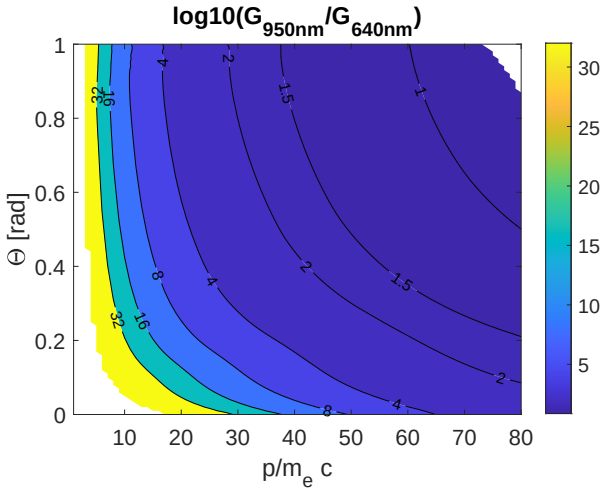

Figure 6.9: Ratio of synthetic spectrometer readings at 950 and 640 nm as a function of momentum and pitch angle. A MultiCam field of view is assumed. The values are computed using the magnetic equilibrium and detector settings for shot 64711 at 0.7036 s.

using artificial filters centred at 640.6 nm and 5 μm. Essentially the figures show the contributions from each point in momentum space to the spectrum recorded by a full view spectrometer pointing along the detector normal.

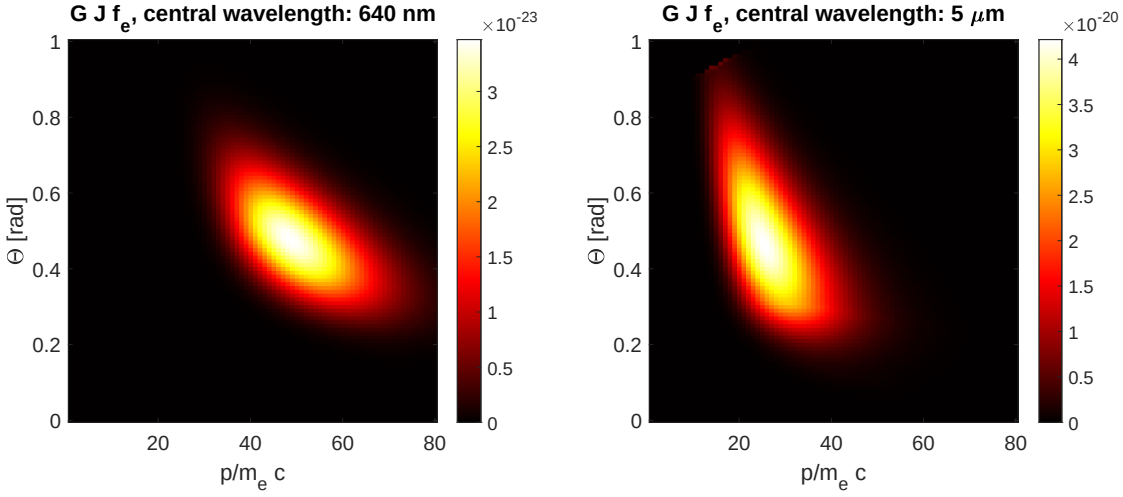

Figure 6.10: Product of the Green function and the avalanche like electron distribution function from equation (6.1) for an artificial MultiCam view spectrometer at 640.6 nm and 5 μm.

Visual inspection readily reveals a significant discrepancy between the parts of phase-space contributing to the spectrometer readings at different wavelengths. The value of GJf_e peaks at $(p, \Theta) = (49\ m_e c, 0.48$ rad) at 640.6 nm, while this is at $(p, \Theta) = (25\ m_e c, 0.47$ rad) in the infrared at 5 μm. The momentum estimate one would obtain from a super particle fitting procedure thus heavily relies on the spectrometer spectral details. While errors in such an approach are commonly attributed to not having a realistic shape for f_e, this analysis points to a more fundamental issue of synchrotron slope fitting. The emission geometry, which depends on the magnetic field and detector, has a strong influence on the recorded emission. This is not taken into account in present day matching of spectrometer data to electron distributions. The correct functional fit form takes on the shape of equation 2.31. Note that the synchrotron spectral power function is already incorporated in the Green function.

To illustrate the size of the errors obtained when ignoring the geometrical features of synchrotron emission, spectra are computed using equations (2.27) and (2.31). The distribution function used for this purpose it that of equation (6.1), cut off below 40 $m_e c$. The spectral range of the artificial spectrometer is between 400 nm and 5 μm, covering typical visible and infrared camera sensitivity regions. The full MultiCam view is used, along with a uniform spectral sensitivity curve. Equation (2.31) is evaluated using SOFT. Using equation (2.27) for slope

fitting requires one to estimate a value for the major radius and magnetic field at the location of emission, which underlies the errors in this approach. Here the minimum major radius of the central line of sight is adopted. A value of $R = 0.85$ m is found with an associated magnetic field in the $Z = 0$ plane of 1.50 T.

The two computed normalized spectra are shown in figure 6.11. Comparing the peak position of the distribution reveals that the SOFT output spectrum is shifted significantly towards the infrared. A first explanation is that the contributing pitch angle varies with the relative orientation of the magnetic field and the viewing direction, and thus changes over the length of the sight line. The contributing pitch angle is larger as one moves away from the point where the viewing line and magnetic field direction are tangent. Since the output power increases with pitch angle, see for instance figure 2.3, contributions from all major radii could potentially contribute significantly to the total spectrum. Prior knowledge on the dominant part of real-space is used to illustrate this point. Computing the spectrum from equation (2.27) using a major radius of 1.07 m and a magnetic field of 1.17 T, corresponding to the spatial edge of the distribution, much better agreement is found between the curves from equations (2.27) and (2.31), provided that one adopts a single pitch angle of 0.36 rad. In realistic situations one does however not know where the dominant emission is coming from, so that neglecting geometric details when computing spectra from f_e can give misleading fits.

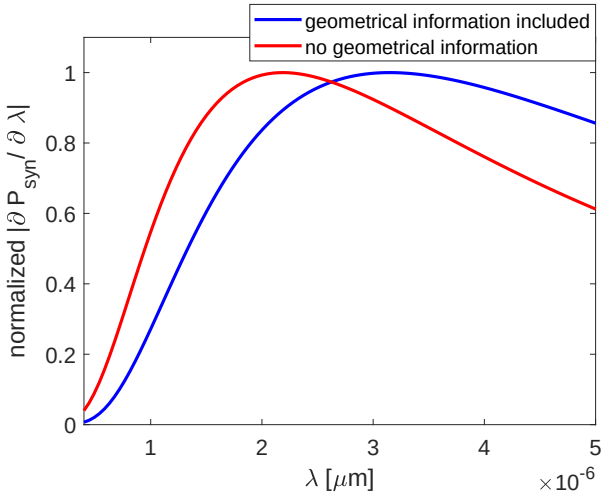

Figure 6.11: Synthetic spectrometer recordings for the distribution function of equation (6.1) cut-off below a momentum of 40 $m_e c$ in the magnetic geometry of shot 64711 at 0.7036 s. The red line is found from equation (2.27) using a constant radius of 0.85 m and a magnetic field of 1.50 T. The red curve shows SOFT output for this distribution, which takes into account the effects of the anisotropic nature of synchrotron emission. The field of view is the same as that for MultiCam. The clear deviation between the two curves illustrates the errors induced by not considering the geometrical details of emission in inferring information on the electron distribution from spectrometer data.

6.3.2 2D ratio maps as an additional constraint

While SOFT can be used to reveal how the anisotropic nature of synchrotron emission complicates estimations of the synchrotron electron distribution from spectrometer data, it might be used to set additional constraints on f_e using 2D views of the plasma. The concept introduced here strongly relies on the ability of multispectral systems to record emission at different wavelengths using cameras with nearly identical viewing geometries. Every point on the surface of visibility has a different associated local major radius and magnetic field, so that the spectrum details vary from point to point. Therefore, for a single momentum and pitch angle the ratio between the intensity of two images obtained using different narrowband filters varies from pixel to pixel.

The ratio of synthetic images generated for uniformly distributed particles with $p = 49\ m_e c$, $\Theta = 0.48$ rad and filters with central wavelengths around 950 nm and 640 nm is shown in figure 6.12. This chosen combination of momentum and pitch angle is based on the peak in GJf_e for the distribution of equation (6.1). A clear increase in ratio from the high (right) to low (left) field side of the image is found. This spread changes with momentum. At 49 $m_e c$ the ratio between the maximum and minimum value of the ratio map is 4.4, while this increases to 5.8 at 45 $m_e c$ for the same pitch angle. Fixing the momentum at 49 $m_e c$ and reducing the pitch angle from 0.48 rad to 0.44 rad the ratio increases to 5.2, showing that also the pitch angle affects this parameter. In case a large set

of possible p, Θ combinations is found from a spectrum slope or geometrical fitting method, the spread in ratio could thus help narrowing down the solution space further.

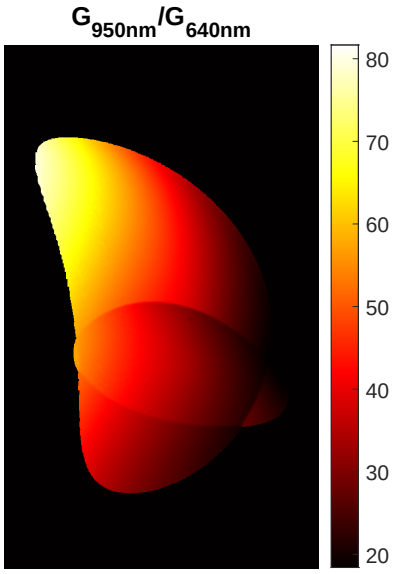

Figure 6.12: Ratio of SOFT $p = 49\ m_e c$, $\Theta = 0.48$ rad transmission weighed Green functions for the MultiCam detector at 0.7036 s in shot 64711 equipped with filters of a central wavelength equal to 950 and 640.6 nm.

A second approach relying on 2D images is the comparison of synthetic and experimental ratios of accumulated image pixel values. This takes away uncertainties related to the exact viewing direction of spectrometers, while including information on the geometrical features of synchrotron emission when a synthetic diagnostic such as SOFT is used. Note that the ambiguity of multiple distribution functions yielding the same spectrum slope is not resolved using this approach. For single momentum, pitch angle distributions the ratio between images obtained around wavelengths of 950, 800 and 640 nm are shown in figure 6.13. Upper bounds have been imposed on the color scale so that contrast is enhanced near values matching those observed in the experimental images, as discussed in the next section.

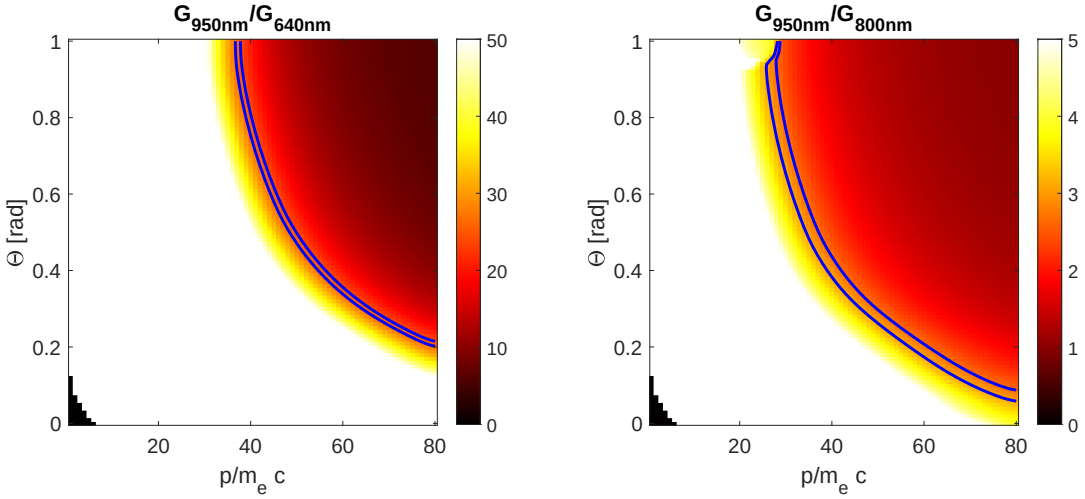

Figure 6.13: Ratio between the accumulated pixel intensity of SOFT images generated for the magnetic equilibrium at 0.7036 s of shot 64711, using synthetic detectors with central filter wavelengths of 640, 800 and 950 nm. Upper bounds of 5 and 50 have been imposed on the 950/800 nm and 950/640 nm map color scales respectively to enhance contrast near the experimentally found ratios. The contour lines indicate the uncertainty bounds of the experimentally obtained summed ratios.

A first observation is that the computed ratios shift towards lower values for higher pitch angles and momentum. The underlying reason in that the synchrotron emission peak moves to lower wavelengths with an increase in p and Θ. As the peak approaches the detector range the local slope becomes less steep and the ratio gets closer to 1. A second observation is that a single ratio corresponds to a line in phase-space. Contour plots reveal that the line shapes are nearly identical for different wavelength ratios so that the combination of two does not lead to a unique solution at some curve intersection. This observation is not merely the result of the proximity of the central filter wavelengths. A theoretical 5 μm detector combined with a 950 and 640 nm filter does not yield a conclusive curve intersection either.

Dependency of the ratio map on the maximum runaway minor radius is assessed. For the point $(p, \Theta) = (40\ m_e c, 0.50\ rad)$ the ratio values increase by 4% and 13% when limiting r/a to 0.8 for the G_{950nm}/G_{800nm} and G_{950nm}/G_{640nm} cases respectively. Resulting uncertainties in the phase-space estimate are of the same order as those introduced by the spread in the experimental ratios. From geometrical constraints on the pattern size one may however reduce the error source by narrowing the possible interval of beam radii.

6.3.3 Application of slope fitting procedures to TCV data

The described information extraction methods are put to the test for shot 64711. Camera calibration procedures in the elaborate Matlab MANTIS analysis structure are still being refined, and this is especially true for synchrotron radiation measurements. Here one is interested not in the total photon flux on the filter, but rather that on the sensor. In this way experimental results can be compared to SOFT output from equation (2.31). The experimental ratios presented here have been carefully checked at all steps of the calibration process and are correct to the best of the authors knowledge. Nevertheless, the analysis presented in this section ought to be applied to more shots to exclude the possibility of systematic errors.

The time evolution of the summed pixel values for channels 1 through 3 is shown in figure 6.14 A. Ratios between these measures for pattern intensity are shown in plot B. The sudden increase in intensity is the result of deliberate vertical movement of the runaway beam. Focus in the analysis is on the frame around 703.6 ms, where the 950 to 640 nm ratio is (25.5 ± 2.6), and that between 950 and 800 nm is (2.9 ± 0.3).

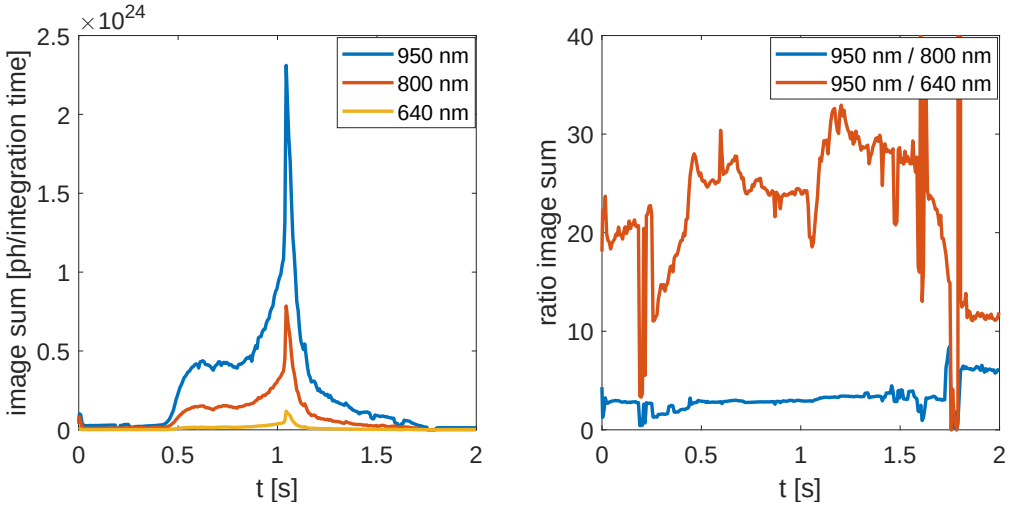

Figure 6.14: A) Time evolution of the calibrated sum of pixel values for the MultiCam channels recording synchrotron radiation in shot 64711. Channels are indicated with the central wavelength of the filter. B) Time evolution of the ratio of accumulated patterns.

The experimentally obtained accumulated image ratios are used to make an estimate of the observed part of phase-space by means of the simplistic single momentum particle approximation. The results for both the 950 nm to 800 nm and 950 nm to 640 nm ratios are indicated in figure 6.13. Both solution planes are rather narrow due to the steep gradient of the ratio maps. The 950 to 640 nm map has the largest relative slope near the observed ratio explaining why the solution plane is more narrow than that observed for the 950 nm to 640 nm output.

Both planes intersect parts of phase-space matching the constraints set by the geometrical fitting procedure. However, the transmission corrected ratio G_{950nm}/G_{640nm} points to momenta exceeding that indicated by the G_{950nm}/G_{800nm} ratio by over 11 $m_e c$. Most likely, this is caused by the simplistic super particle approach adopted

here. As was shown in section 6.3.1, energy estimates adopting such a peaked distribution depend on the wavelength under consideration. Since the emission weighed energy of the particles contributing to the spectrum at 640 nm is higher than that for 800 nm, the sign of the energy discrepancy appears plausible.

The 2D ratios computed for the experimentally obtained images are shown in figure 6.15. A threshold at 11 % of the maximum pattern intensity has been subtracted from all images to remove reflection, stray light and non-synchrotron continuum contributions outside the pattern region. From the uniformity of the background, and the consistency between the different channels, it is found that the introduced uncertainty in the ratio is negligible compared to that introduced by the labsphere calibration. Both maps show a clear increase in ratio from the high to low field side, consistent with the expectation displayed in figure 6.12. Note that matching the optical alignment of the channels is crucial for getting an accurate ratio. Similar attempts using shot 64614, where clear offsets between camera views exist, yield strong fluctuations of ratio over the pattern which obscure interpretation.

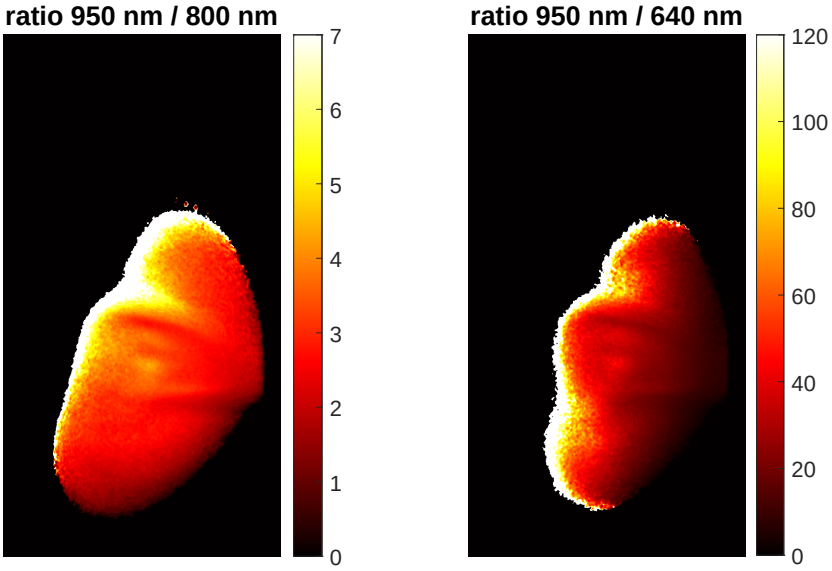

Figure 6.15: Experimentally obtained synchrotron pattern ratios at 0.7036 s in shot 64711. Note that limits have been set on the colorbar to better emphasize differences within the pattern. A background level at 11 % of the image maximum has been subtracted from all images before computing the ratio.

An attempt is made to reduce the solution space arrived at using the G_{950nm}/G_{800nm} ratio through a 2D ratio analysis. To do so, the maximum and minimum value of the overlap region ratio are computed for phase-space points between 0.40 and 0.50 rad along the solution curve displayed in figure 6.13. These pitch angles were chosen so as to assure that the overlap region falls within the synthetic MultiCam field-of-view. A constant ratio between these values of 2.2 ± 0.2 is found, meaning that this parameter can not be used to restrict the dominant phase-space. Variations in the spread are observed moving perpendicular to the contour lines of phase-space also found in the summed ratio maps. In the super particle approach, the ratio spread appears to serve as a consistency check rather than a tool for constraining the contributing electrons.

The real power of the 2D ratio method is expected to only reveal itself once experimental maps are compared to those resulting from realistic particle distributions. This is an endeavour yet to be initiated. It should be noted that the data storage needed for an elaborate ratio image sweep is large. SOFT output for 3 filtered images of 1032 by 580 pixels whose wavelength contributions are spaced by 0.2 nm and are computed on a phase-space grid with a 1 $m_e c$, 0.01 rad resolution, is over 10 TB. The summed ratio method requires a database of only 17 kb. Summed image ratios for the three channels discussed in this section, are computed in 0.4 ms for an arbitrary distribution function, which allows quick scans through a large set of potential distributions using this spectral method.

A comparison of the space-space reduction obtained using a geometry based procedure and the summed spectral ratio method presented here, is shown in figure 6.16. For setting the geometrical constraints, the horizontal position of the right edge of the overlap region in the experimental 640 nm image is compared with that of single (p, Θ) SOFT images. An upper bound of 20 pixels discrepancy is set, which is arbitrary but serves to make the point addressed here. Features of the pattern geometry remain rather constant when increasing pitch angle and

momentum proportionally. The solution bounds therefore stretch out in a direction orthogonal to the solution space obtained from the spectral methods. While not just one single point of intersection between the areas is found, most likely due to the simplistic distribution function shape, this hints at the potential of combining the two methods to significantly constrain local phase-space.

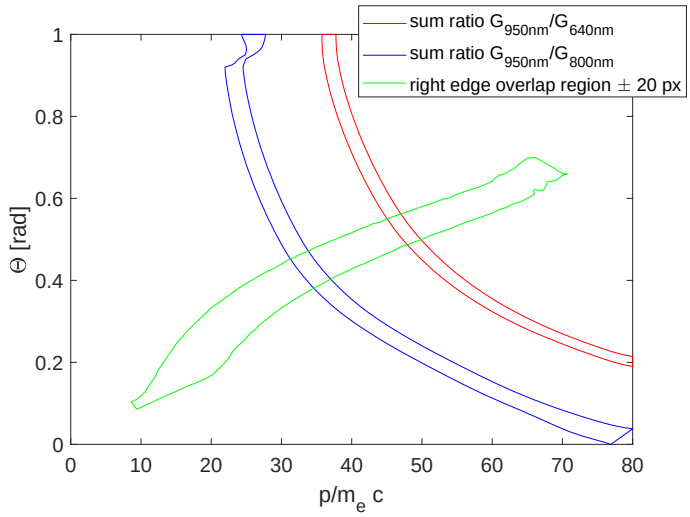

Figure 6.16: Comparison of the phase-space bounds for the electrons contributing to the synchrotron radiation. Restrictions based on the summed intensity ratio map of figure 6.13 are displayed. Furthermore, to illustrate the effect of combining geometrical and spectral approaches, a solution spaced based on the horizontal location of the right edge of the overlap region is portrayed. Note how the two solution spaces are stretched in orthogonal directions.

6.4 Varying the runaway beam position

6.4.1 Validation of SOFT behaviour for vertical plasma translations

The highly refined geometrical features of the synchrotron emission observed in some of the TCV shots along with the vertical control system present in TCV provide the ideal conditions for verification of the theory underlying SOFT and its implementation. Dependence of spot shape on the relative vertical distance between the camera and RE beam can be scanned experimentally as well as through the generation of synthetic images. Experimental data allowing this kind of benchmarking of synthetic diagnostics is novel. In this section an overview of the validation procedure and results are provided. Results presented here are also described in the corresponding paper by M. Hoppe, G. Papp, T.A. Wijkamp et al [84].

During shot 64614 the TCV control system moves the magnetic axis from $z = 0.23$ m to $z = -0.04$ m. The synchrotron pattern grows to constant state in the first 0.8 seconds. Position dependent geometry changes are thus studied from this point onwards for a fair comparison. Calibrated and distortion corrected images from the 640 nm filter channel at times $t = 0.800, 1.113, 1.375$ s are shown in the top row of figure 6.17. The pattern observed is a projection of two disconnected surfaces of visibility. Nearest to the camera is the large spot which shows a large shift across the image as the RE beam moves down. The smaller spot originates from a surface at a larger distance from the camera, and as a result shows a smaller shift with changing z. Due to the relative shift of the two projections there is a clear vertical dependency of the spot shape.

Comparison to SOFT output requires a choice of distribution function. In section 6.2 it was demonstrated that a small part of the momentum phase-space contributes most to the observed emission, and that single momentum distributions can reproduce overall spot shape adequately. Also, there are clear bounds to the phase-space region in which the dominant population should lay, based on the requirements that the surface of visibility projections overlap and are positioned at the correct horizontal location. This motivates the use of single momentum distributions in matching the experimental results of shot 64614. Generating images over all of accessible phase-space and manually matching the geometrical features, yields an approximate momentum of $p = 50 m_e c$ and pitch angle of $\Theta = 0.40$ rad. Details guiding the visual inspection are the small spot size and position and the relative orientation of the right side of the larger lobe.

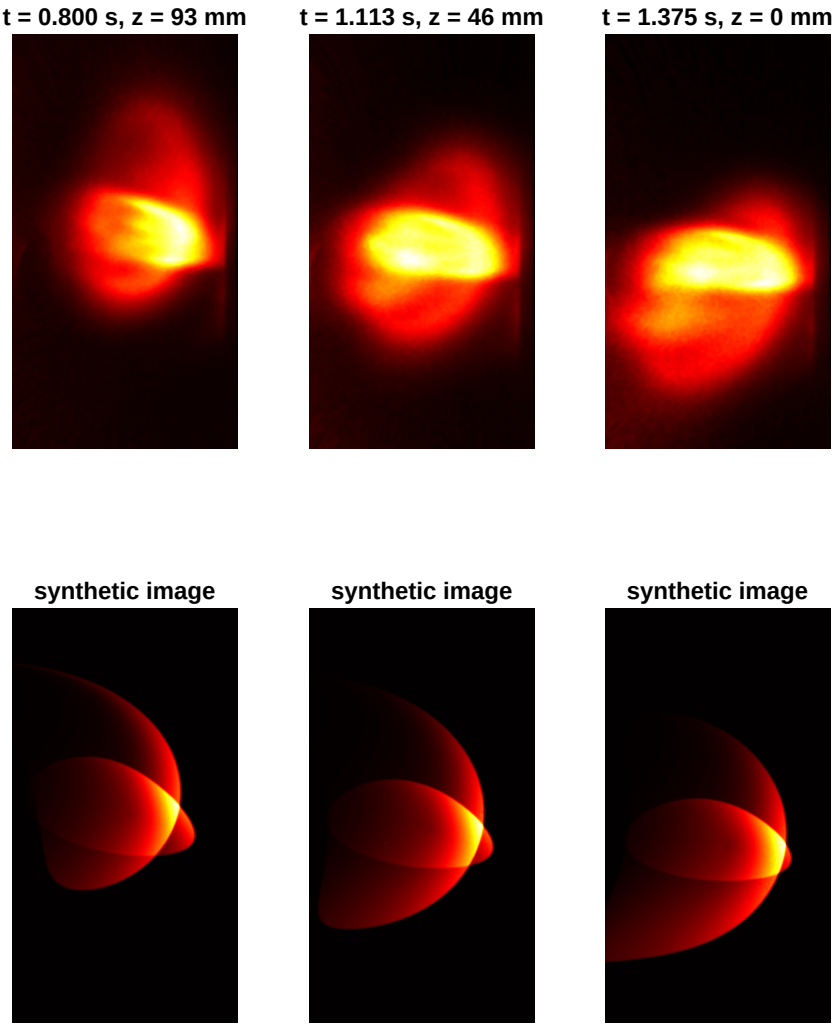

Figure 6.17: The top row shows experimentally obtained images from shot 64614 at different times and vertical runaway beam position for a camera channel equipped with a 640 nm narrowband filter. The large spot corresponds to a surface of visibility near the camera, and shows a large shift and change in orientation with respect to the smaller spot originating from a surface further away. Synthetic SOFT images for single momentum, $p = 50\ m_e c, \Theta = 0.40$ rad, spatially uniformly distributed electrons are shown in the bottom row. While the simplistic distribution does not yield the correct intensity distribution, the vertical shape dependency is close to that recorded experimentally.

The bottom row of figure 6.17 shows synthetic images corresponding to the LIUQE magnetic field reconstructions for the times indicated on the top. The spot position and relative orientation of the projected surfaces matches the experimental ones well at each point in time. Most notable is the agreement in the relative shift of the two projections. This is a good indication that the simplifications made in the guiding-center theory behind SOFT are sufficiently accurate to reproduce geometrical synchrotron spot details observed in experiments.

It is worth noting that more intricate distributions have been tried in matching the experimental data. Doing so modifies the intensity distribution but does not alter the conclusion about the vertical geometry dependence drawn here. In all cases the synthetic SOFT images displayed the experimentally observed relative shift of the surface projections.

6.4.2 Constraining momentum space using multiple vertically offset detectors

Apart from validation of SOFT behaviour, the vertical position scan is a test case for the usefulness of having two vertically offset detectors. Viewing the runaway population from two different angles yields different patterns and potentially distinct dominant phase-space regions. Thus, additional constraints on the runaway distribution could be attained, or degeneracies in the best fit solution could be lifted.

SOFT allows for the generation of images from a detector at any position in the tokamak. The Green function for an upper port MultiCam system is obtained by translating the middle port camera to $z = 0.45$ m. Such a system would image the runaway beam from a position which is nearly a mirror of the mid port detector around the plane which has z equal to the typical runaway axis height of 0.23 m. To assess whether the dominant population is expected to change significantly with detector position, a simplified avalanche like electron distribution of the following form is used:

$$f_e = \exp(20\cos(\Theta))\exp(-2.1 \cdot 10^{-3} p^2).$$

The product GJf_e is evaluated in the phase-space region $p = 40 - 65\ m_e c$, $\Theta = 0.3 - 0.7$ rad for both detector positions as shown in figure 6.18. The RE beam has its axis at $z = 0.23$ m for the magnetic field used in the image construction. Differences in the dominant momentum position are limited. The peak momentum is at 51 $m_e c$ in both cases and the pitch angle value decreases from 0.51 rad to 0.48 rad moving from the middle to top port. This is a difference expected to fall well within uncertainties caused by errors in the distribution function estimate from image fitting.

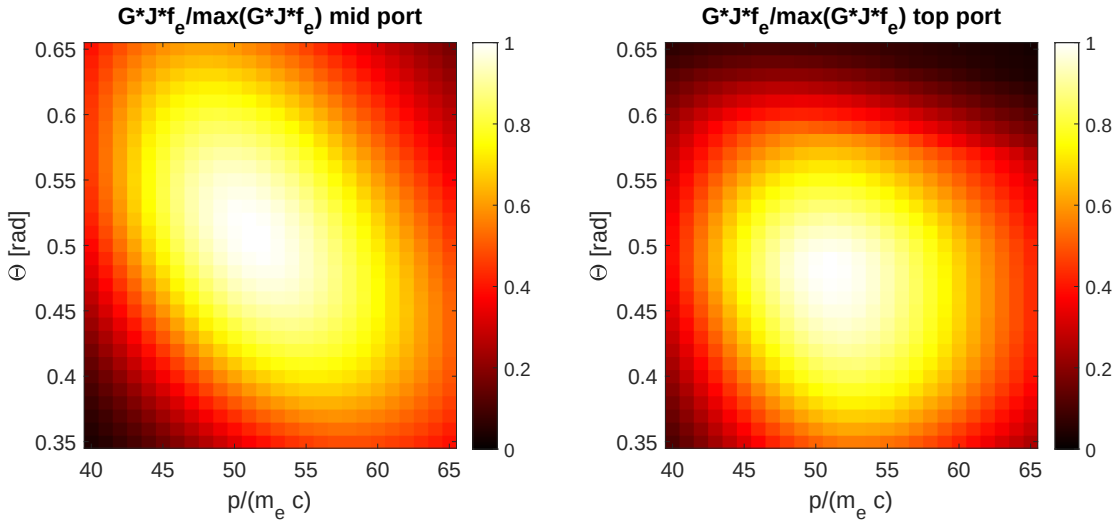

Figure 6.18: phase-space contributions to the total image formed in shot 64614 at 1.075 s from an RE beam at $z = 0.23$ m, constructed using synthetic MultiCam detectors at the mid and top port of TCV and a distribution function of the shape (6.1).

Although the region of phase-space which can be studied varies little with the vertical detector position, there is a clear difference in the observed pattern geometry. For the distribution function adopted in this section, the projected emission is shown in figure 6.19. The mid port image shows a pattern resembling that observed in the experimental images. As compared to the single momentum estimates, the region close to maximum intensity is now more smeared out and the orientation of the large lobe matches the observed pattern better. Clearly, having an idea of the distribution function shape is essential in obtaining accurate synthetic image matches. The top port pattern is cut-off at the bottom by the finite field of view. Also, it has a vastly different shape than the mid port emission projection. In case mid port fits based on geometry do not yield conclusive results, having a vertically offset camera could thus potentially provide alternative fitting material to work with.

The same analysis is performed for a runaway beam with its axis at $z = 0$ m. Using the same distribution function the shift is somewhat more pronounced than for the $z = 0.23$ m case, but remains small. While the peak of the image contribution is at $p = 51 m_e c$, $\Theta = 0.50$ for the middle port detector, the dominant population is at $p = 50 m_e c$, $\Theta = 0.45$ for the top port. Regardless of the RE beam position, for dominant populations at high pitch angles and momentum having a vertically offset detector is expected to have limited added value when trying

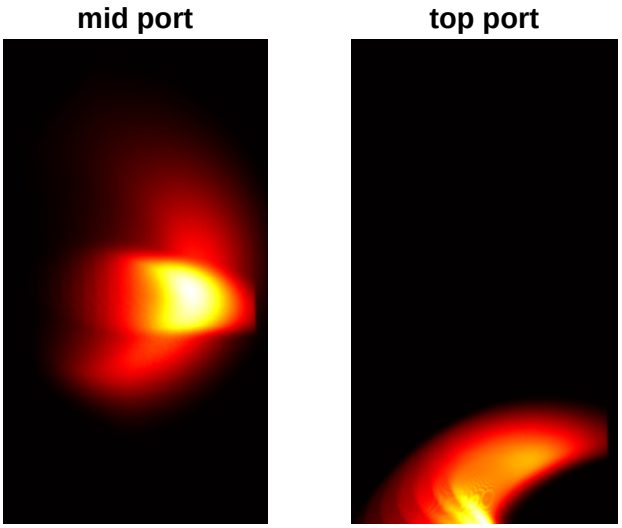

Figure 6.19: SOFT image reconstructions for shot 64614 at 1.075 s for the MultiCam system at the mid and top port. The electron distribution function is of the form $f_e = \exp(20\cos(\Theta))\exp(-2.1 \cdot 10^{-3}p^2)$.

to constrain the runaway distribution function at multiple positions in phase-space. The situation in which the detection peak lies at lower p and Θ is excluded from this discussion.

6.5 Conditions and explanation for pattern observations

6.5.1 Comparing plasma parameters

With the knowledge that the observed part of phase-space during the experimental campaign is of high momentum, pitch angle and minor radius, the basis is in place to explore the difference between the shots in which synchrotron radiation was and was not observed. As a relevant case-study the focus is on shots 64591 through 64595. These disruption scenario experiments are performed to quantify the relation between the amount of krypton injected to cause a disruption and the natural decay time of the subsequently formed RE beam. For a proper comparison, the runaway seed population right before the injection should ideally be similar during all shots. It is however found that from around 0.48 s onwards a synchrotron pattern starts to appear on the 640 nm MultiCam channel in shots 64593 and 64595, while it remains absent in the other shots. Interestingly, the two mentioned shots are the only ones in the sequence in which no post-disruptive RE beam is formed. The presence of observable synchrotron radiation in only a subset of the shots points towards a difference in the runaway seed population.

A wide range of diagnostics is available to identify differences in plasma parameters between the two sets of shots. On the basis of parameters governing kinetic model input, a comparison is shown in figure 6.20. Peak temperature (A) and density (B) data are derived from Thomson scattering measurements. These provide a rough, but at this stage best available, estimate of these core values. Large fluctuations in the signal and a low time resolution make it challenging to pinpoint temperature differences between the shots with and without recorded synchrotron radiation. Clear differences do appear in the density. Shots 64593 and 64595 do show a very similar trend with higher density values than those of the shots where no synchrotron emission was recorded.

A very clear distinctive factor in the plasma parameters is the estimated average electric field (C). Shots for which synchrotron radiation was recorded show a clearly elevated field with respect to those for which this was not the case. Given the high dominant momentum of the detected electrons, this is an observation in line with the experimental data. The higher loop voltage behaves so as to correct for discrepancies between the target and measured plasma current. The observed drop in I_p (D) for the two synchrotron shots is a likely candidate for causing the higher value of V_l.

Indicators for the runaway evolution can be observed in figure 6.20 in the form of the maximum calibrated MANTIS pixel value (A), the MANTIS X-ray estimation (B) and the PMTX signal (C). Plot A is a measure for the intensity of the synchrotron pattern strength. The figure clearly portrays the difference between the two sets of shots, as an

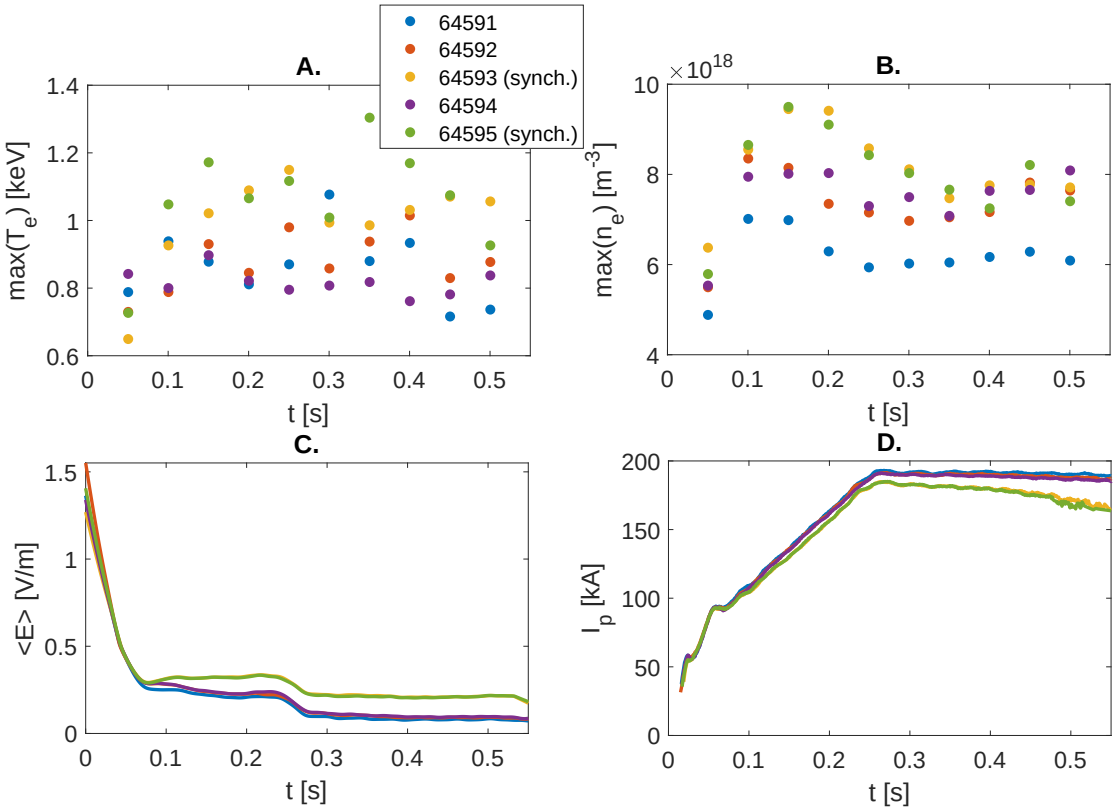

Figure 6.20: Comparison of plasma parameters for shots 64591 through 64595. The indication 'synch.' marks the shots for which synchrotron radiation was observed. Data is shown for an interval between plasma breakdown and krypton injection. A.) Maximum recorded electron temperature derived from Thomson scattering data. B.) Maximum electron density derived from Thomson data. C.) Smoothed average electric field estimate using the loop voltage and magnetic equilibrium reconstruction from LIUQE. D.) Plasma current evolution.

exponential increase of intensity is observed for shots 64593 and 64595. This evolution can be used for comparison of experimental data to the output of kinetic simulations using SOFT as a conversion tool. Note that the pattern does not reach saturation before the material injection and the subsequent disruption at 0.55 s.

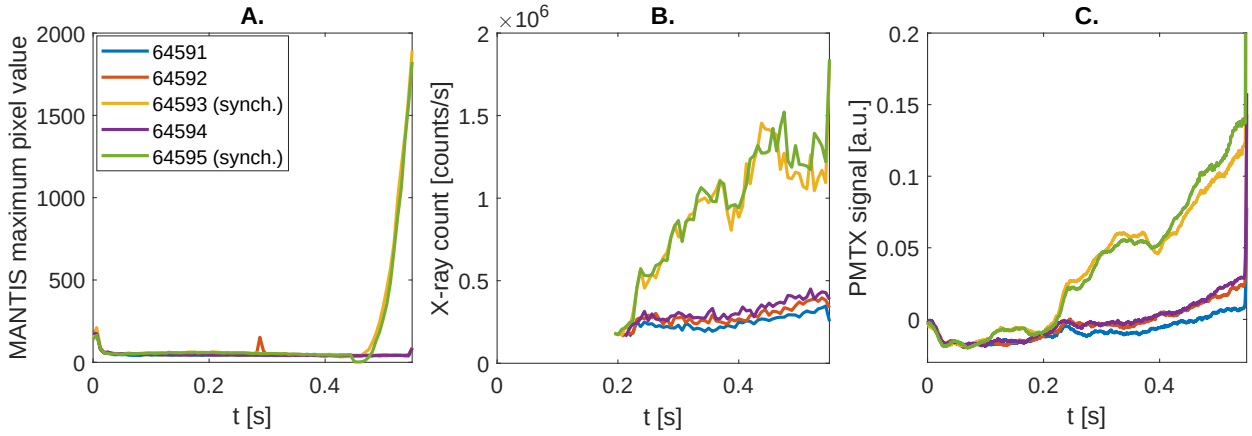

Figure 6.21: Comparison of runaway signals for shots 64591 through 64595. A.) Maximum calibrated pixel recording of snow filtered MANTIS images on a 640 nm filtered channel. The intensity is an indication of the synchrotron emission strength. B.) X-ray counts per second as determined by counting the X-ray snow on MANTIS images. C.) PMTX hard X-ray signal.

The X-ray signals (B,C) show an increase in from 0.2 s onwards for shots 64593 and 64595. For the shots where

no synchrotron radiation is detected a much smaller slope is found. Note that shot 64591 deviates from the other two non synchrotron shots on the PMTX, showing a lower signal. During this experiment the electron density was somewhat lower, which gives an indication that n_e is a parameter to take into consideration when trying to explain the experimental discrepancies. This is not unexpected as density is one of the governing parameters of kinetic theory.

6.5.2 Influence of different production mechanisms

Using the temporal evolution of the temperature, density and electric field, possible differences between primary and secondary production mechanisms in the two subsets of shots can be identified. The analysis presented here is of a 0D nature and forms a starting point for more elaborate 2D modelling efforts.

Dreicer generation

A first potential source of deviations is found in the Dreicer mechanism, which depends sensitively on the electric field. Also, the Driecer production rate introduced in equation (2.7) is a non-trivial function of the electron density and temperature through the Dreicer field. Using Thomson scattering data for the pre-disruption estimate of the density and temperature profiles in shot 64591 at 0.40 s, a Z_{eff} equal to 1 and an electric field of 0.10 V/m on axis, the ratio E/E_D is found to be $3 \cdot 10^{-3}$. The radial production profile depends very strongly on the distribution of Z_{eff} and E. Impurities present in the plasma causing radial deviations in Z_{eff} as small as 1% yield drastic changes in the radial profile. This makes an evaluation of the runaway source location challenging.

To illustrate the influence the electric field can have in Dreicer production, the estimates used above are compared to those for shot 64593 in which synchrotron radiation was observed. With an E/E_D equal to $7 \cdot 10^{-2}$ the steady state production rate exceeds that for 64591 by a factor of $7 \cdot 10^2$ assuming again that Z_{eff} is equal to 1. The computed production rate is however not deemed realistic at $3 \cdot 10^{19}$ s^{-1}. A quick calculation shows that a total runaway population of about $2.2 \cdot 10^{16}$ particles is required to carry the full 200 kA plasma current. Given the plasma cross-section the time until full conversion is reached in only 5 ms. Modifications to the effective charge as large as a factor of 4 do not resolve this issue.

A relativistic treatment of the Dreicer problem using the full Dreicer growth rate by Connor and Hastie is attempted [85]. Essential is the incorporation of the critical field as derived by Hesslow et al, taking into account partial screening [9]. As a dominant impurity specie Ar is chosen for the availability of the required constants to illustrate the effects of contaminations in general. Equation (A.1) is used for the effective field, assuming Ar^{15+} is the dominant ionization stage. This follows from the Coronal picture at 1 keV as calculated using equation (3.1). The use of this extended model has drastic consequences for the Dreicer growth rate through a modified E_c and Z_{eff}. For an impurity density of $1 \cdot 10^{17}$, which is around 2 % of the Deuterium content, the growth rate is reduced by over three orders of magnitude to $1.6 \cdot 10^{16}$ s^{-1}. Assuming a uniform production rate it would require over 8 seconds for a full current conversion which is far more realistic than the time scale estimated using the simple Dreicer growth model.

It should be noted that under these conditions the model predicts no Dreicer generation for the shots with low loop voltage. Given that MANTIS has non zero X-ray counts in these situations, and a seed is required to form the observed post-disruptive beam, this is evidently not the case. Expectations are that differences in the impurity content between the different sets of shots are not the sole cause for the deviations. Spatial non-uniformity of plasma parameters, especially the electric field, are likely to be involved. The analysis here does however show the importance of accurate electron-background plasma modelling and motivates a further inquiry into the impurity content during the pre-injection phase.

Avalanche effect

Given that significant synchrotron emission is observed from a high pitch angle part of phase-space, it is deemed unlikely that the Dreicer mechanism and direct acceleration alone can be used to explain the observations. Without pitch angle broadening mechanisms, runaways are typically collimated along the magnetic field vector [86]. The underlying argumentation is twofold. Firstly, acceleration by the toroidal electric field primarily increases the parallel speed of the electron. Secondly, synchrotron radiation losses increase with pitch angle damping so that perpendicular momentum is readily dissipated.

To assess whether secondary generation could play a role in the studied shots, equations (2.7) and (2.9) are evaluated. Central axis plasma parameters for T_e, n_e and E in shots 64592 and 64593 are used to calculate the RE population growth rates due to primary and secondary generation. To compute the effective critical field the same

approach is used as in the last section, assuming Ar impurities for the availability of the appropriate coefficients. Quantitative agreement is not the aim of this highly simplified 0D approach. The goal is to find out if secondary generation could be important under the given conditions. The fractional impurity content is varied from $2 \cdot 10^{-5}$ to 0.1. Runaway growth rates are calculated starting at 0.1 s to avoid ambiguities in the breakdown phase. Results for both shots along with an indication of the full current conversion level are displayed in figure 6.22.

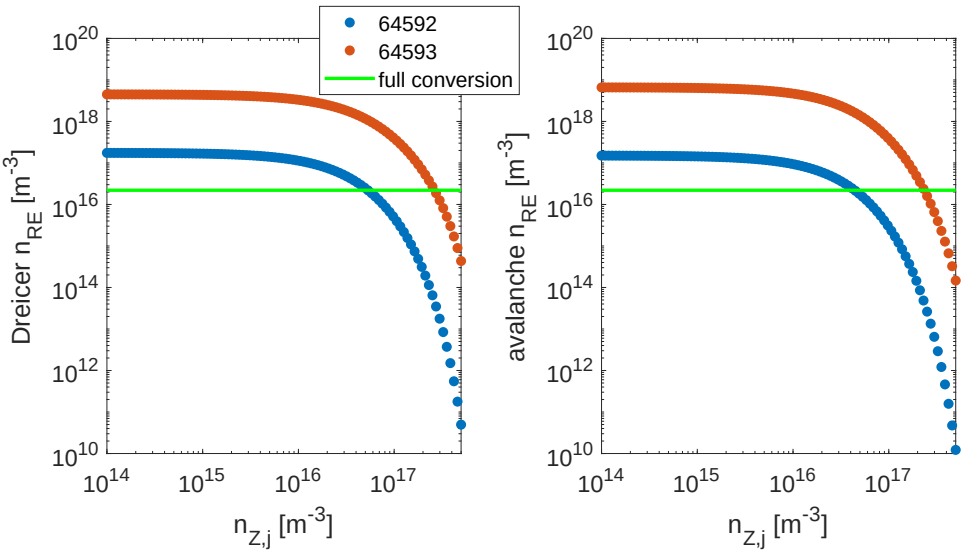

Figure 6.22: Total Dreicer and avalanche runaway production rate as a function of Ar impurity content, calculated using plasma parameters between 0.1 and 0.55 s in shots 64592 and 64593. A line indicating the full current conversion level is shown.

For the plasma parameters retrieved for the two shots the two production mechanisms have a comparable contribution to the total RE current. The contribution of the avalanche mechanism is a factor 1.4 larger than the Dreicer generation below fractional impurity densities of $2 \cdot 10^{-3}$. For higher Ar content Dreicer production starts to dominate within the studied range. The total production drops with $n_{Z,j}$. In this model around 1% impurity content is needed to not achieve full current conversion in 0.45 s. Note that this assumes a uniform RE production in the plasma which is not deemed realistic. Regardless of the Ar content, the secondary mechanism appears non-negligible and might have contributed to the evolution of the RE population in the experiments. Secondary generation is thus likely to be involved in the explanation as to why high pitch angle electrons are found to be present in the plasma.

Synthetic images from local analytical solutions

In order to distinguish between different production mechanisms, an attempt is made to find a local distribution function shape for the pattern observed in shot 64584 using the asymptotic expressions introduced in section 2.6.2. The use of this shot is motivated by the fact that the synchrotron pattern reaches saturation state before disruption. Note that the density is a factor of 2 higher than in the sequence of shots considered in the rest of this section. In the calculation pitch angles between 0.2 and 0.7 rad are included along with momenta between 30 and 80 $m_e c$. For convenience, the fit forms are reprinted below:

$$\text{Dreicer:} f(p_\parallel, p_\perp) = f_0 \exp(c_1 \cos(\Theta) p + c_2 \sin^2(\Theta)),$$
$$\text{avalanche:} f(p, \Theta) = \frac{f_0}{\cos(\Theta) p} \exp\left(d_1 \cos(\Theta) p + d_2 \tan(\Theta) \sin(\Theta) p\right).$$

First consider the high p limit for the kinetic equation in case Dreicer generation dominates. The coefficients c_1 and c_2 are determined by means of an iterative sweeping procedure which narrows down the parameter space at each step. The found values depend on the fitting selection criteria. A RMS error between the real and synthetic image is computed, as well as the RMS error for all parts of the image which exceed 50% of the maximum intensity value. The latter is representative for the match in the overlap regions. Error maps and the best fit

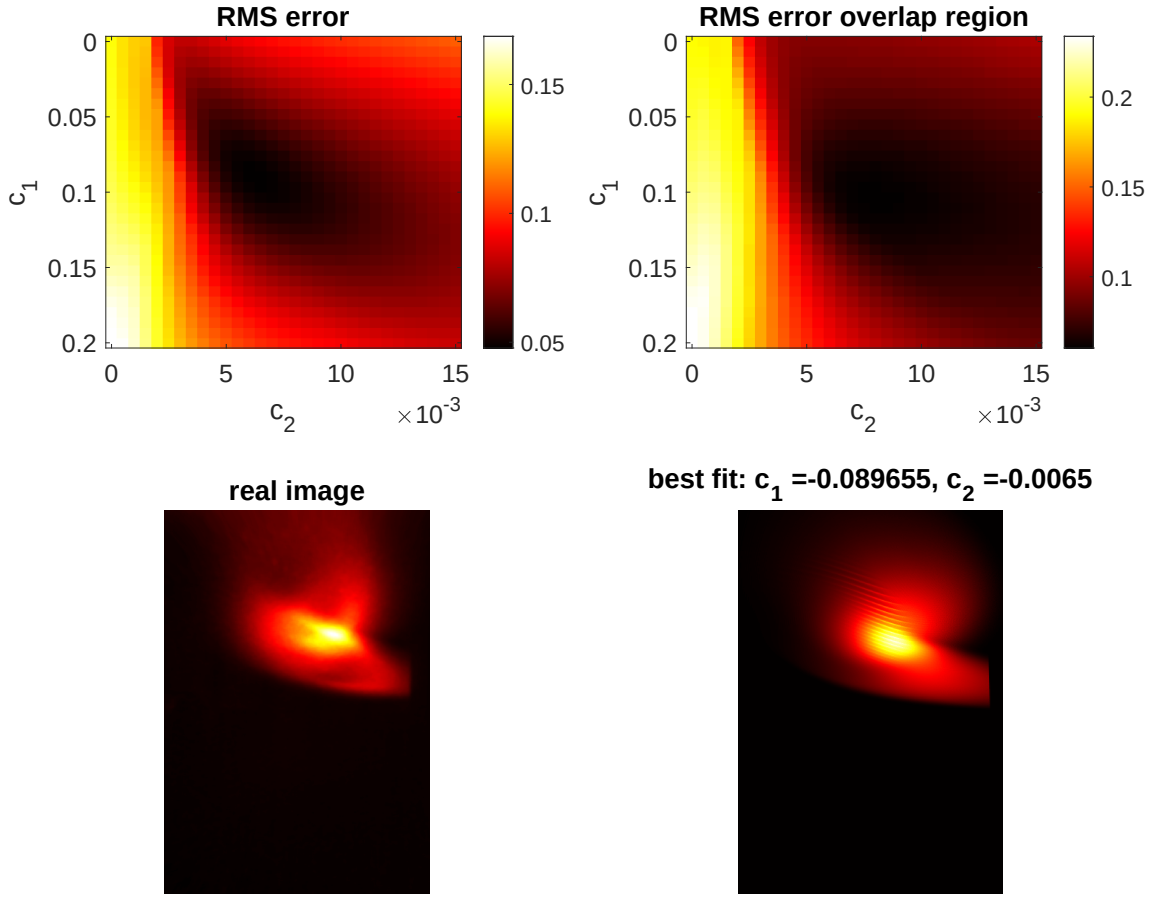

Figure 6.23: Root-mean-square error between the normalized synthetic and experimental image as a function of c_1 and c_2 for the high p Dreicer limit distribution of equation (2.34). The error is computed for the full image and the region exceeding 50% of the maximum intensity value. A RMS based best fit is shown on the bottom right.

are shown in figure 6.23. The full- and overlap region fits provide coefficients of $(c_1, c_2) = (-0.09, -0.0065)$ and $(c_1, c_2) = (-0.10, -0.0080)$ respectively. deviations between the coefficients are limited and provide similar images.

As a check on the coefficient magnitude, equation (2.34) is used to compute E/E_c from its theoretical connection to c_1 and c_2. From c_2, which does not depend on the effective charge, a value of 2.3 ± 1 is found. Using the electron density and mean electric field during the quiescent phase of shot 64584, it is found that the critical field exceeds the Connor-Hastie field by a factor of 6.6 ± 2.9. This is not uncommon in real experiments, meaning that c_2 is in the expected order of magnitude. Using this estimate and the expression for c_1, the matching value of Z_{eff} is found to be 0.5 ± 1.5. Only values above 1 are physically acceptable, but since expectations are that the plasma shows little contamination without injection, the inclusion of 1 in the found range is encouraging. The coefficient values are along the line of expectation.

A similar analysis for the avalanche distribution is shown in figure 6.24. Again the best fit coefficients obtained using the two different error maps are comparable at $(d_1, d_2) = (-0.16, -0.30)$ for the full image and $(d_1, d_2) = (-0.17, -0.38)$ for the thresholded one. Comparing the coefficient values to the expected ones, a non-physical value for Z_{eff} of -4.8 is found. To get a realistic value of Z_{eff} the absolute value of d_1 would have to be about on order of magnitude smaller. Assuming an effective charge of 1 the second coefficient does give a realistic value of E/E_c of 2.4 ± 0.2.

Judging from the obtained best fit and the coefficient values, neither of the 2 parameter models performs clearly better than the other. As shown in figure 6.25, the ratio between the normalized distribution functions is fairly constant in the phase-space region which was found to contribute most to the experimental image. The approach outlined here does not yield additional information on the RE production mechanisms at play, but is consistent

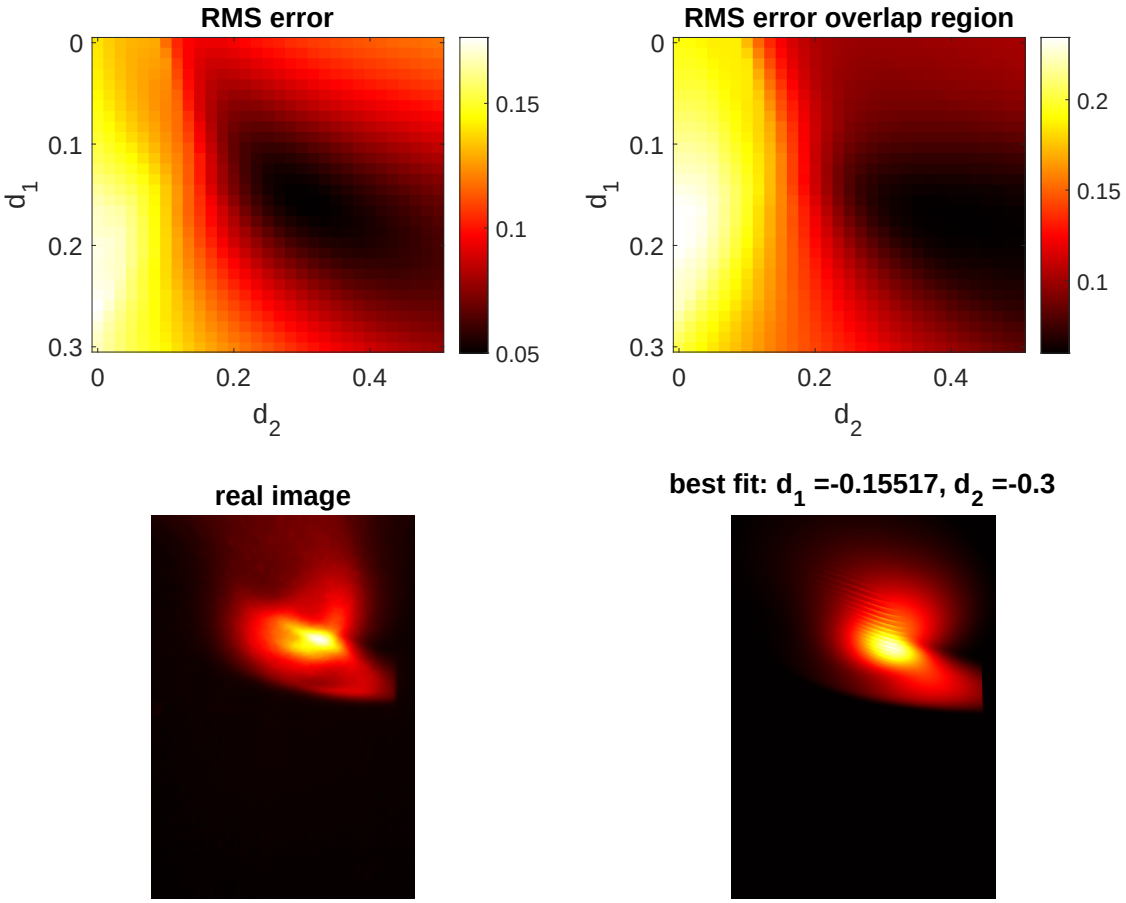

Figure 6.24: Root-mean-square error between the normalized synthetic and experimental image as a function of d_1 and d_2 for the avalanche distribution presented in equation (2.6.2). The error is computed for the full image and the region exceeding 50% of the maximum intensity value. A RMS based best fit is shown on the bottom right.

with the super particle geometrical estimate of the dominant part of phase-space.

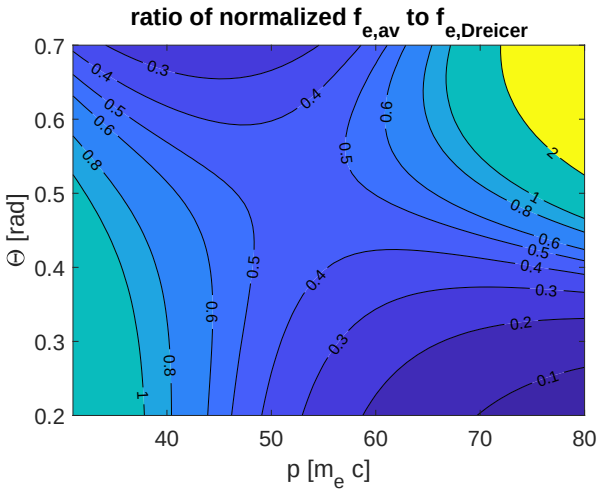

Figure 6.25: Ratio between the normalized distribution functions obtained as best fits to the synchrotron pattern observed in shot 64584. These were constructed using the 2 parameter models outlined in section 2.6.2.

6.5.3 Energy limits

Apart from the question what mechanisms populate the observed part of phase-space, one may also wonder what is setting the upper bound to the observed energies. Differences between the shots with and without observed synchrotron radiation could find their origin in deviations of such limits. From geometrical fits it is believed that the momentum of the observed electrons is not at the peak of camera sensitivity near $64 m_e c$. Therefore a drop in f_e steeper than the increase in the Green function G is required to explain the synchrotron observations in the first place. This can be caused by the details of the processes populating the high momentum, high pitch angle region, or by the presence of an energy limit. The latter can either be related to the upper bounds described in section 2.4, or by yet to be identified transport mechanisms.

Loop voltage limit

From the loop voltage upper bounds on the runaway energy at each point in time can be set using equation (2.18). At the moment when the synchrotron radiation starts to appear the difference in this maximum attained energy between the two subsets of shots is 11 MeV. It is a possibility that for the shots for which no synchrotron radiation was observed the runaways have not yet reached the part of the phase-space for which the Green function is sufficiently large to detect radiation on the camera. The energy for the dominant population in shot 64584, which has a fully developed pattern and similar plasma equilibrium as the shots considered here, was estimated before at 26 MeV. Interestingly, integrating the loop voltage from the moment when n_e has reached its equilibrium until 0.48 s when the synchrotron radiation starts to appear, the upper bound in energy is 32 MeV for shots 64593 and 64595, while it is only 22 for shots 64591, 64592 and 64594.

Two side notes have to be made regarding this explanation. Firstly, an electron accelerating nearly parallel to the electric field will not reach the required pitch angle for observation. To reach the observed (p, Θ) region in time the electrons would have to be scattered to higher pitch angles without too large a loss of energy. Secondly, the synchrotron pattern in shot 64584 remains constant for nearly 0.5 s after saturation. This indicates that the loop voltage is not the limiting factor during the final stage of that experiment, and other limits could play a role as well in the comparable shots 64591 through 64595.

A quantitative comparison of the recorded light intensity and predicted SOFT output could shine more light on the matter. In the considerations above it is assumed that only after the first 80 ms a significant population of electrons will be accelerated, as this is the first Thomson measurement showing an electron density near the stabilization level. During the breakdown phase runaways can however also be formed in low n_e, high E conditions. A quantitative analysis could give an indication of how many runaways are needed to provide the observed level of radiation. This could then be used to assess whether enough REs could have been created in the first tens of milliseconds to emit the detected level of synchrotron emission. If so, this alters the estimate on the maximum attained energy at 0.48 s, and excludes the loop voltage as the decisive energy limiting mechanism. In conclusion, due to the currently unknown production in the first phase of the discharge, no verdict can be drawn on whether it is the loop voltage limit which separates the two sets of shots.

Synchrotron energy limit

A second limiting factor for the runaway energy and pitch angle is synchrotron radiation losses. Using formula (2.22) the limits for shots 64592 (no synchrotron radiation) and shot 64593 (synchrotron radiation) are estimated. In doing so the major radius, magnetic field and loop voltage have to be chosen. Since top views of the SOFT surfaces of visibility show that the observed light originates from major radii equal to or larger than that of the magnetic axis, see for instance figure 6.3, R and B are retrieved for the axis and edge of the plasma. With regard to the loop voltage the value from LIUQE is adhered to. The results are shown in figure 6.26.

The curves show that the limits at 0.5 rad are separated by 11 $m_e c$. Furthermore, from this approach it appears that the p, Θ combination corresponding to the best geometrical fit for shot 64584, which has similar magnetic geometry, can not be reached. Note however, that this geometrical fit concerned the fully developed pattern at saturation. Applying the approach above to shot 64584 with a loop voltage of 1.5 V gives a limit of 48 $m_e c$ at 0.4 rad and 41 $m_e c$ at 0.5 rad. This is close to the phase-space estimate. Apart from differences in RE pitch angle distribution estimates the synchrotron limit emerges as a possible source for the difference between the shots where we do and do not record synchrotron emission.

This analysis, assuming a cylindrical plasma, does not cover the full geometry of the synchrotron problem. Also, the fact that currently no accurate estimate for the electric field distribution is available hinders a verification of

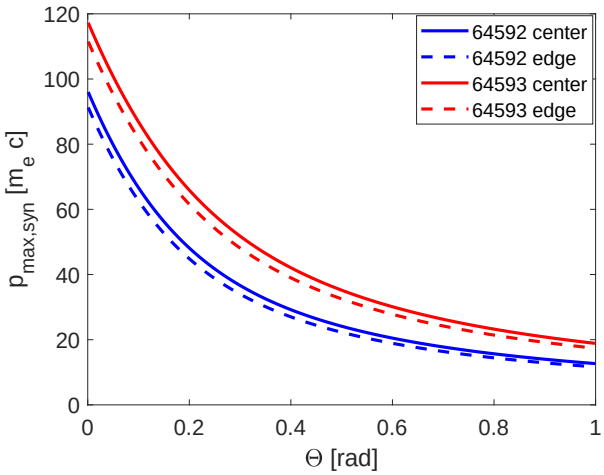

Figure 6.26: Synchrotron radiation momentum limit as a function of pitch angle for shots 64592 and 64593 at 0.48 s, as computed using equation (2.22). Curves for both magnetic axis and plasma edge values of the major radius and magnetic field are portrayed.

the hypothesized difference in the RE energy limit. The analysis does however point to a promising subject for further investigation with the use of 2D spatially resolved kinetic models.

Magnetic field ripple

As addressed with the introduction of equation (2.24), sufficiently energetic electrons can have a cyclotron frequency in resonance with the rate at which they feel ripples in the magnetic field due to the 16 toroidal coils. Since the cyclotron frequency is linearly proportional to the magnetic field, which scales as $\sim 1/R$, and the ripple frequency shows the same dependency the resonant energy is nearly independent of the major radius of the orbit. The estimated TCV momentum threshold for the first resonance, 900 MHz on axis, is somewhat lower than the estimated momentum as it is found to be $(46.3 \pm 0.4)m_e c$. Pitch angle scattering via this mechanism is therefore likely to occur at the energies under consideration, and might contribute to the population of detectable electrons. Higher order resonance frequencies are encountered at lower energies and could contribute to this process although the interaction weakens with increasing resonance order. The contribution of magnetic field ripple effects to the runaway dynamics could be assessed in TCV by modifying the number of used coils in this flexible system.

Orbit effects

A manner by which high energy and pitch angle electrons could be selectively lost to the wall is the drift orbit shift. The energy and pitch angle dependent expression for the orbit displacement to the low field side was given in equation (2.16). No such collisions with the wall are expected at the high field side as the drift orbit shift increases faster than the gyro radius so that the relativistic electrons do not have a point in phase-space where their orbit crosses the inner post.

For the low field side the situation is different, as both an increase in gyro radius and orbit shift with momentum and pitch angle bring the electron trajectory closer to the wall. Using the magnetic equilibrium values for the toroidal and poloidal field at $Z = 0$ from shot 64584, the normalized minor radius at which electrons are lost is computed as a function of momentum and pitch angle. The results are shown in figure 6.27.

In section 6.2.2 a minimum value of the maximum RE beam minor radius was obtained by comparison of an experimental synchrotron pattern to SOFT images. It was concluded that the beam should at least expand up to a normalized minor radius of 0.78 to explain the observed patterns. This sets an upper limit on the values of p and Θ crossing the $(p, \Theta) = (64 m_e c, 0.64 \text{ rad})$ point. To obtain a correct overlap region size it was argued that the minimum radius is somewhat larger, which would correspond to a lower momentum and pitch angle threshold. Orbit effects could therefore well be part of the explanation as to why light is observed from the identified part of phase-space.

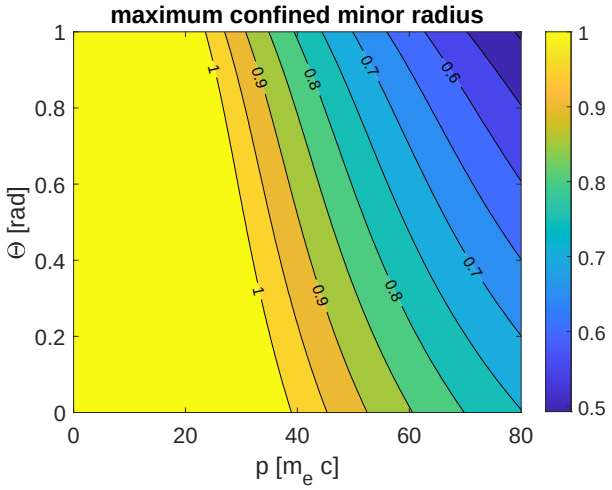

Figure 6.27: Maximum normalized plasma minor radius at which runaways are not lost to the wall via the orbit shift and gyro-movement, as a function of normalized momentum and pitch angle. The magnetic equilibrium data at $Z = 0$ for shot 64584 is used.

The role of transport

The limits treated above decelerate or stop the growth of particle energy, but apart from the orbit limit, do not necessarily de-populate the corresponding part of phase-space. As for shot 64584, all synchrotron radiation patterns saturate in intensity if no gas is injected, as shown in figure 6.28. The PMTX hard X-ray curve also saturates in read-out value, around the same time as the pattern intensity. These results indicate that the population of the visible momentum space reaches a near equilibrium state. Either the electrons are trapped here or the influx is equal to the outflux. Since the light originates from the edge of the plasma the second situation could entail continuous radial diffusion of REs outwards where they are eventually lost to the wall. Regardless of whether this is the case or not, the fact that runaways are observed near the edge of the plasma indicates that transport plays an important role in explaining the observations.

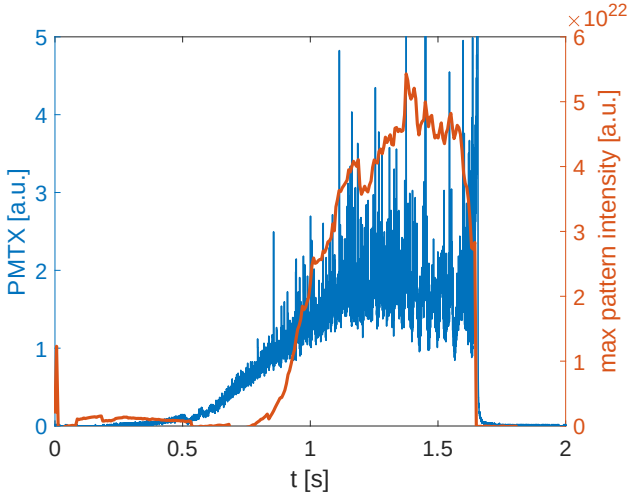

Figure 6.28: Time evolution of the PMTX hard X-ray signal and maximum synchrotron pattern pixel value for the quiescent shot 64584.

Classical transport of electrons is due to a random radial walk through collisional processes. For particles of the observed momentum and pitch angle the diffusion coefficient is estimated to be $D_{cl} = \rho_{l,e}^2 \nu_{th,rel} = (2.0 \pm 0.4) \cdot 10^{-3}$ m^2/s [7]. Neoclassical transport is not expected to play an important role due to the low collisionality of runaways. Actual transport coefficients have been found to exceed the classical value by orders of magnitude [87]. RE transport is thought to be dominated by magnetic micro-turbulence through the overlap of narrow magnetic islands [88]. The diffusion coefficient is expected to increase with the relative perturbation size $\delta B/B$ [7].

Using the magnetic probes on TCV a difference in the magnetic turbulence between the shots with and without synchrotron radiation is searched for. Apart from the absolute magnitude of the poloidal field, which stems from differences in the plasma current, no distinguishing features are found. Installation of magnetics which can detect fluctuations on shorter time scales is required to potentially pinpoint differences in the contribution of micro-turbulence between the two sets of shots.

6.5.4 Directions for kinetic modelling

Based on the analysis presented in this section, directions for kinetic modelling of the synchrotron shots are provided. The rough estimate of Dreicer and avalanche growth rate contributions from section 6.5.2 suggests that detailed modelling of avalanche sources is of essence. Incorporation of radiation reactions on the momentum space evolution is crucial as well since energies were found to approach the synchrotron radiation barrier in section 6.5.3.

Since the detected electrons are found near the edge of the plasma, the kinetic modelling will have to take into account spatially non-uniform plasma parameters. Alternatively, if one has an idea if the involved transport times and location of RE generation this non-uniformity can be transformed into a time dependency. This would allow for the use of computationally efficient 0D codes. Transport estimates are however an outstanding issue of RE studies on their own.

From the simplified analysis of energy limits in section 6.5.3, none of the treated mechanisms can be excluded as source of the momentum limit. Experiments with alternative coil currents or plasma shapes can help isolating the different effects. Moving the circular plasma radially will for instance affect the orbit drift limit. As such data is currently not yet available, kinetic models of considerable detail will likely be required to differentiate between the influence of the different phenomena.

6.6 Conclusions

In this chapter the power and limits of synchrotron image analysis with the use of synthetic tools have been demonstrated. This was done using multispectral MultiCam images of the quiescent shot phase in several experiments of the TCV MST1 campaign. The most important conclusions following from this work are brought together in this section.

Using the computationally efficient tool SOFT the dominant momentum and pitch angle space contributing to the synchrotron images has been constrained by means of a geometrical fitting procedure. From the well defined geometrical features of the patterns it was found that:

> *Synchrotron radiation in the visible range can be observed in TCV. Through geometrical comparison to images from the synthetic diagnostic SOFT it is concluded that the light originates from high momentum ($\sim$50 $m_e c$), high pitch angle ($\sim$0.50 rad) runaway electrons at the edge ($r/a > 0.8$) of the plasma.*

This result remains standing when perturbing the magnetic field and camera calibration. The obtained knowledge provides a validation opportunity for kinetic codes, as the time evolution of this part of phase-space can be used to compare numerical and experimental results.

Experimental validation of SOFT behaviour was aimed for using a vertical position scan of a quiescent runaway beam, leading to the following statement:

> *Experimentally observed geometrical changes in synchrotron patterns when varying the vertical runaway beam position are accurately reproduced by SOFT.*

Conclusions from geometrical fitting procedures can be reinforced through spectral methods. Commonly used spectrum fitting methods are first evaluated. It is shown that:

> *Using super particle approximations to extract distribution function data from spectrometer recordings:*
>
> *i Can yield misleading interpretations as very different f_e can yield the same spectrum [24].*
>
> *ii Provides very different results depending on the spectral detection range of the spectrometer.*
>
> *iii Is non-conclusive, as a best fit (p, Θ) curve over a wide range of values is obtained.*

More generally, for electron distributions of all forms it is concluded that:

> *Due to the highly anisotropic nature of synchrotron emission, the distribution best fitting spectrometer data depends sensitively on the relative geometry of the magnetic field and detector.*

This implies that attempts at extracting runaway distribution information using spectrometers calls for a comparison with forward modelled results from synthetic diagnostics such as SOFT. Simply fitting a spectral emission function to the data, instead of using the full Green function, can yield misleading interpretations.

Having to take into account the geometrical features of synchrotron emission does not only complicate fitting procedures but can also provide additional constraining parameters.

> *Multispectral imaging systems can provide 2D synchrotron projections with the same viewing geometry at different wavelengths. Ratios between these images are sensitive to the details of the electron distribution function, and can potentially be used to constrain estimates of the observed part of phase- and real-space.*

This method is put to the test using TCV MultiCam data. Qualitative agreement with super particle SOFT images is found regarding the ratio spread over the image. It is yet to be examined whether more accurate distribution function shapes can lead to quantitative agreement.

An idea for further constraining phase-space evolution through cameras with different viewing positions is explored. It is concluded that

> *For a TCV like machine and a visible light camera, the targeted part of phase-space is affected little by the vertical camera position. The geometrical features of the synchrotron pattern do however strongly depend on the position, so that an extra system can be used to formulate additional geometrical constraints.*

Over the whole sequence of TCV experiments not all shots display synchrotron radiation. It is found that occurrence of these patterns coincides with a failure to create a post-disruptive RE beam using MGI. A difference between the shots with and without patterns is searched for. The most prominent difference in plasma parameters is that the loop voltage is significantly higher in case radiation was observed. It is found that the impurity content during the pre-injection phase can strongly affect RE generation processes and that both Dreicer and avalanche generation could have played a role. The latter might be important for explaining the high observed pitch angles.

The dominant momentum and pitch angle are compared to theoretical energy limits for runaways. It is found that:

> *Theoretical runaway momentum limits related to loop voltage, synchrotron radiation, field ripple and orbit effects are all consistent with the estimated energies and pitch angles. None of these explanations can be excluded as limiting factor.*

The magnetics do not resolve differences which can explain transport discrepancies between the two sets of shots. Further kinetic modelling is essential to pinpoint the dominant mechanisms and contribution from spatially non-uniform plasma parameters. For the time being it is unclear as to what precisely causes the difference between the shots, and more importantly why this difference appears to govern the formation of the post-disruptive runaway beam.

Chapter 7

Reconstruction of emission profiles in TCV runaway studies

Kinetic modelling of runaway experiments requires knowledge of the prevailing electron and impurity temperature and density distributions inside the plasma. Such properties can be inferred from 2D emissivity profiles provided by multispectral systems, given that suitable CRMs are at hand. On the basis of chapters 3 and 4 the different experimental phases are revisited, addressing the question whether currently available CRMs are applicable or if benchmarking of newly developed models is required. Challenges unique to each discharge phase are identified and where possible addressed.

A test-case for emissivity reconstruction is presented for neutral and singly ionized helium. The spatial resolution is assessed and the profiles are used to study a runaway current expulsion event in the post-disruptive phase. The unique multi-wavelength view of the plasma is used to form a hypothesis for the question why concentric emission tubes are observed for neutral helium during the event, potentially shining light on the magnetic geometry of the field during the phenomenon. Understanding the transport of runaways during instabilities is of essence for predictive modelling efforts.

7.1 Limits of emission profile reconstructions in runaway studies

7.1.1 Pre-processing of images

Camera footage obtained during runaway experiments has two potential sources of pollution for which multispectral systems and the MANTIS analysis structure were not originally designed to deal with. X-ray noise and strong continuum background radiation may obscure interpretation and are therefore briefly revisited here.

X-ray noise

An example of an emission reconstruction using data from a TCV RE experiment was shown in figure 5.8 in the context of uncertainty estimates for circular profiles. Before invoking the SART algorithm most images require median filtering to remove X-ray contributions. This image pre-processing avoids the incorporation of non-physical sharp pixel gradients across the image in the iterative solution descent. It does however mean that edges of emission regions in the original image typically obtain a spatial uncertainty of around 3 pixels with the used filter settings. In real space this translates to an error of about 3 mm which means that for the size of inversion elements used here the spatial uncertainty in the emission profile is about 1 element. This ought to be taken into account deciding if to filter an image with a low amount of X-ray noise.

It should be noted that during the post-disruptive phase the X-ray snow sometimes reaches the filtering limit for the MultiCam middle port configuration. The majority of pixels are white in this case, so that median filtering will not provide a usable image. In MultiCam this situation regularly occurs as the device is close to the vessel and a significant amount of light is lost in the beam-splitter structure. The latter means that large gains are required, which increases the amount of detected X-rays per exposure time. A typical value above which the image filtering procedure provides grainy results is 6 dB.

Synchrotron background radiation

The appearance of synchrotron radiation in the visible range comes with welcome information on the runaways in the plasma as was shown in chapter 6. When focussing on line radiation this continuum source however modifies the perceived line emission. The two can be hard to separate when they overlap. Having a dedicated synchrotron filter in the filter set can help identifying whether such pollution is present, and on what parts of the image this is the case.

Correction for this light can occur on physical grounds if it can be established that the region from which light in some image originates should not show any line emission. An example is the center of a circular plasma where on grounds of the temperature hydrogen should be fully ionized. This is the case for the Balmer channels depicted in figure 6.1. The synchrotron contribution in this example is however minor and barely rises above the reflection light. The issue is more pronounced for weaker emission lines.

Given that the pattern structure is roughly the same across the different viewing channels, an approach to removing the undesired contribution is by using a subtraction method based on the synchrotron channel. This is especially useful in situations where line- and synchrotron emission overlap, as manually zeroing out local synchrotron contributions is then not feasible. A complication here is that the intensity distribution can vary significantly with wavelength as was shown in section 6.3.2. While subtraction will likely improve the accuracy of the input to the inversion algorithm, one should be cautious when drawing conclusions from the inversion.

7.1.2 Discharge phases

Four shot phases of interest are separated here following the scenario outlined in chapter 4. All involve different time scales on which the plasma parameters evolve. During the breakdown phase, typically lasting around 20 ms, the plasma emission starts with a spike. For the strongest emission lines MANTIS can capture the evolution in 25 frames. Due to the strong temporal emission gradient most of the frames display a large region of saturation as camera gain changes are based on a feedback process. Parameters such as density and temperature are highly uncertain so that the breakdown runaway seed remains unknown. Multispectral systems can indicate where the breakdown is occurring, but are of limited use if exposure and gain are not pre-set. Determining the right values for these settings is an iterative procedure, most likely requiring several shots. Dedicated breakdown experiments, with suitable short exposure time settings, have not been conducted. Studies of plasma position evolution during this phase, when LIUQE reconstructions are absent, might benefit from such attempts. This information is valuable for start-up runaway studies.

Second is the quiescent phase, where the number of runaways and their energy increase over time in a steady plasma. Images obtained in this time interval are characterized by a low level of X-ray noise, and the plasma by high temperatures and low densities. Due to the slow fluctuations in plasma parameters the gain and exposure have ample time to adjust. Equilibrium collisional radiative models are expected to yield accurate results here. Runaways have little influence on the plasma emission at the low RE density and high T_e so that rate coefficients obtained through ADAS can be used [22]. However, since little impurities are present the hot center of the plasma where most runaways are formed is hard to probe. This limits the usefulness of obtained reconstructions as these will typically only allow temperature and density estimates near the edges.

Before the thermal quench when gas is injected, multispectral imaging data becomes more valuable. The distribution of gas in the plasma is a highly uncertain parameter in RE modelling. This while the assimilation of gas in the plasma and the RE beam, especially in post-disruption situations, is one of the crucial output parameters in mitigation studies. MANTIS like systems could provide a 2D spatial evolution of the gas location. Hindering factors are (i) the involved time scale and (ii) toroidal asymmetry of the emission right after injection. MGI and pellet injection studies require the use of fast cameras reaching acquisition rates of at least 10 kHz. This is an order of magnitude faster than can be achieved by the small sized MANTIS cameras. Also, initially gas is not distributed equally in the toroidal direction which invalidates the tomographic inversion procedure applied here. Judging when the method would become appropriate requires a study of the parallel transport time scales.

Shortly after gas injection the thermal quench sets in. As this phase lasts a few ms, MANTIS can captures this event in only a small amount of frames. Plasma parameters change quickly and time evolving CRM models are required to describe the emission. At the same time the RE current increases significantly due to the avalanching effect so that the validity of currently available collisional radiative coefficients is compromised. Using pre-set exposure times to avoid saturation multispectral systems have the potential to aid in spatially resolved RE CRM model validation.

The main value of emission reconstructions with multispectral systems currently lies in resolving the location of different ionization stages and impurities in the post-disruptive stable phase. Evolution of the plasma parameters up until the final disruption is gradual enough to resolve the spatiotemporal dynamics. Obtaining quantitative data in terms of densities and temperatures is hindered by molecular, metastable and RE contributions to the emission which greatly increase the complexity of the problem. Emissivity profiles for post-disruptive scenarios could however be used for benchmarking CRMs for runaway companion plasmas. An application not requiring an intermediate model is ionization state tracking. This application is demonstrated in the next section for Helium states.

7.2 Resolving Helium charge states

During a select number of experiments of the TCV MST1 campaign, RE beam formation is triggered using a He injection. Given the filters available for MultiCam operation this gas type is the most suitable candidate for testing the procedure of separating ionization states in space. To this end a HeI filter for a triplet emission line at 587.6 nm is used alongside a HeII 468.6 nm singlet line.

7.2.1 Quiescent phase

As an example of ionization state resolved imaging, helium images from the pre-disruptive phase are treated. Leftover and intrinsic He radiates at the edges of the circular plasma as shown in figure 7.1. From visual inspection it appears that the emission from HeII originates from smaller minor radii than that of HeI. This is consistent with the picture of a radially decreasing temperature profile. Thomson scattering is not suited for resolving the low temperatures at the edges for comparison. The images are used as input for the SART procedure, the outcome of which is depicted in figure 7.2. Here the emissivities are shown in the poloidal plane along with the difference between the two. HeII indeed radiates up to smaller radii than HeI.

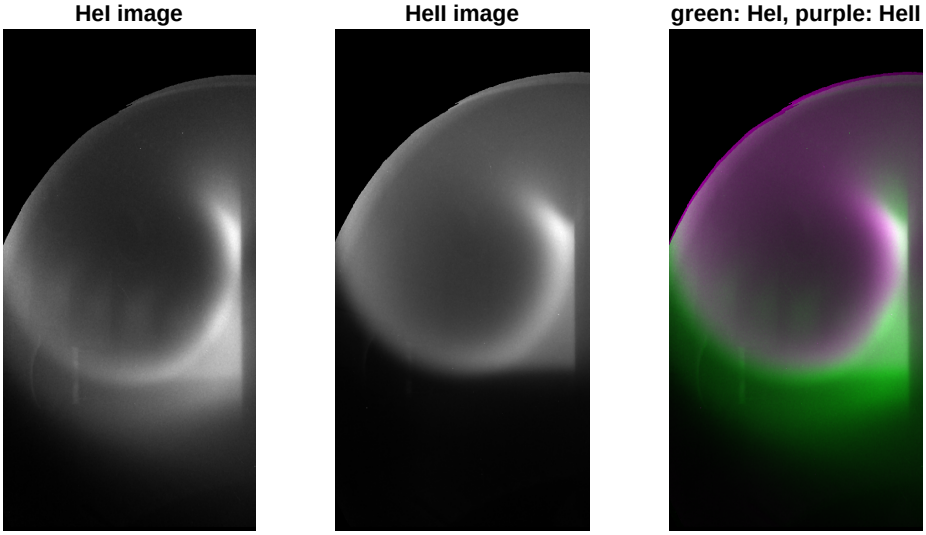

Figure 7.1: HeI and HeII emission from the edges of a circular plasma at 0.53 s into shot 64719. Note that HeII appears to radiate at smaller minor radii than is the case for HeI, as illustrated most clearly in the image at the right.

An important feature in the reconstructions is the absence of the circle on the top right of both images. This is found in all reconstructions performed for the images in the MST1 TCV campaign. It is likely related to an insufficient amount of rays used in calculating the geometry matrix. Further inquiries into the underlying mechanisms and possible solutions are required to obtain information on the missing region of the plane. These are deferred to future studies.

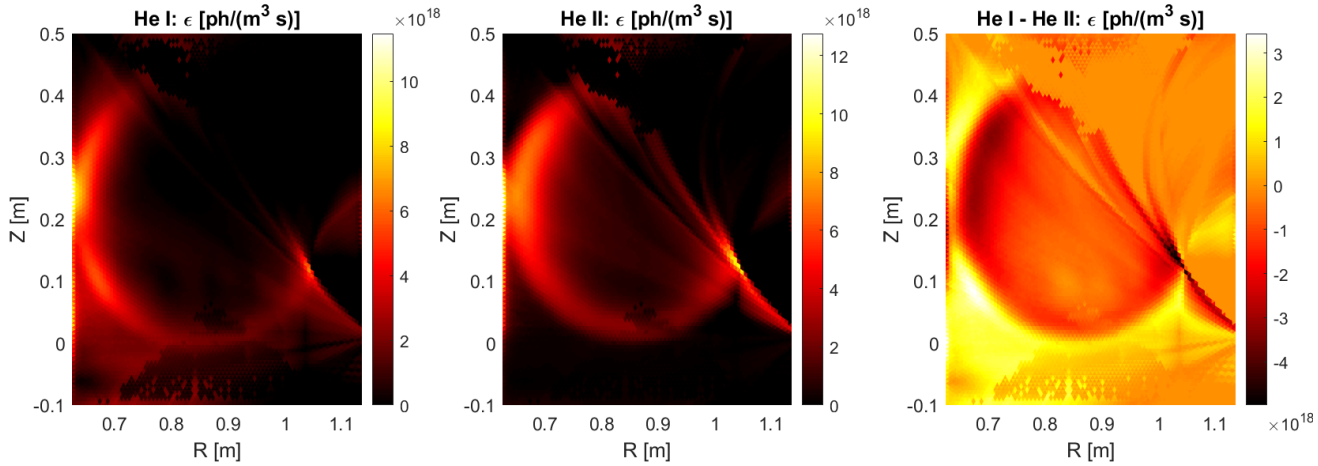

Figure 7.2: Emissivity profiles for HeI and HeII in the poloidal plane at 0.53s into shot 64719. On the right the difference between the profiles is depicted to show that HeII radiates up to minor radii smaller than is the case for HeI as is expected for a peaked temperature profile. The absence of the circle on the top right is attributed to reconstruction artefacts.

7.2.2 Post-disruptive phase

Post-disruptive emission patterns are vastly different from those observed before the gas injection due to the low core temperature and increased density. As the core is cold enough to permit He emission the profile of emissivity now takes the form of a filled tube. This is illustrated using HeI and HeII data from shot 64723, 80 ms after the gas injection. Obtained images at three different times are shown in figure 7.3. Emission tubes are centred some 23 cm above the camera and are thus viewed from below. The HeII images show local RE excitation traces, which distort the inversion through their non toroidally symmetric shape. Appearance of these tube-like structures could point to the presence of magnetic islands trapping the runaways [69]. To make any conclusive statements tube tracing procedures can be used to obtain the local q-factor by means of Calcam and LIUQE. Such an endeavour is however deferred to future work.

A few observations can be made here. Firstly, the emissivity of HeI appears to extend to larger minor radii, as would be expected for a temperature profile peaked at the center. Secondly, the HeI profile shows a sudden expansion at time 0.637 s. Concentric tubes are visible on a single frame, after which the tube recovers to its original state. Similar bursts are seen in multiple shots and correspond to a temporary increase in X-ray snow on the MultiCam images. Motivated by this observation the plasma current and PMTX signal are retrieved and displayed in figure 7.4. Within the 1 ms temporal resolution of the signal 3.5 ± 0.5 kA of I_p are lost, which amounts to around 2 % of the total runaway plasma current. At the same instance in time the PMTX signal shows a strong spike, corresponding to a significant loss of REs to the vessel wall.

To better map the spatial structure of the emissivity an attempt is made to invert the images. Results are shown in figure 7.5. Although the same emissivity artefacts on the top right remain, other features of the pattern are reconstructed well. The difference in tube size is clearly visible, and even the concentric tubes in the bottom left image for HeI are retrieved. From visual inspection, the center of the profile is at $(R, z) = (0.86, 0.21) \pm (0.01, 0.01)$ m which is close to that provided by LIUQE at $(R, z) = (0.85, 0.22)$ m. Furthermore, the HeI intensity appears to drop near the center of the plasma which could indicate that more He is ionized here. Either temperatures or RE driven ionization might be higher in this region than at larger minor radii. This statement does come with the side note that the drop in HeI intensity is near the artefact region, so that it should be reassessed once the inversion problem has been dealt with.

Changes in the emissivity profiles are analysed using the emission at $z = 0.210$, which is calculated using all emission elements which have their geometrical center within 2 mm of this central value. The time evolution of the radial emissivity traces for both HeI and HeII is shown in figure 7.6. Times before the current ejection around 0.637 s are shown, as well as two profiles after the disappearance of the concentric rings. For HeII the emissivity increases monotonically towards the center of the plasma at all studied times. The high values near the limiter at $R = 0.62$ m are attributed to emission artefacts. As the moment of RE current loss is approached the central emissivity value increases, but the trend with radius is not affected. The increase continues undisturbed after the expulsion event.

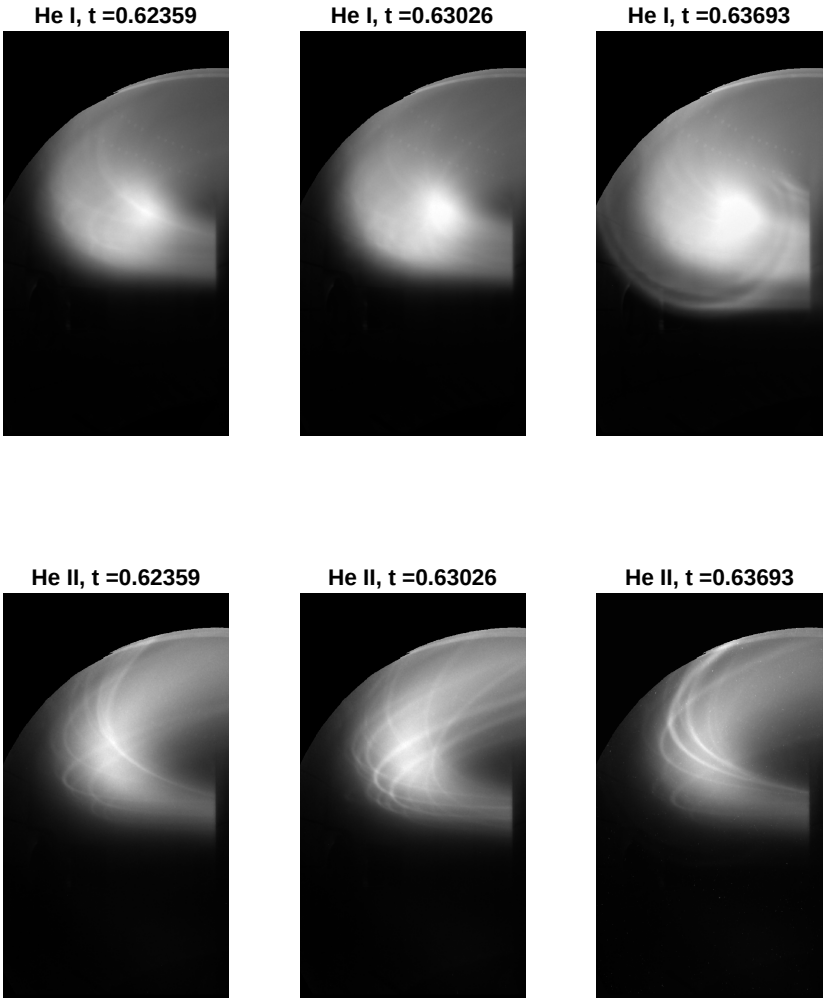

Figure 7.3: HeI and HeII emission in the runaway filled disruptive plasma in shot 64723. The last frames correspond to a sudden loss of plasma current, spike in the hard X-ray signal and a short burst of magnetic activity.

HeI profile evolution follows a different trend. At first ϵ increases monotonically from the edge until $R = 0.80$ m, after which a descend towards a local minimum at the plasma center is set in. This corresponds to the observation made in the initial visual inspection. As the current expulsion is approached the central emissivity rises. The fact that both emissivities increase could indicate a change in the local density, temperature, RE distribution or impurity content. Identification of what drives these changes can help forming a hypothesis on what mechanism is causing the RE current loss. Interestingly, the Mach-Zehnder interferometer shows an increasing trend in the electron density estimate, as shown in figure 7.7, very similar to the behaviour of the HeI emissivity. A higher electron density means more collisions to excite the ions, and is thus in line with an increase in ϵ. The behaviour of HeI emission however deviates from this trend, and a different mechanism needs to be invoked to explain the observations.

The temporary emission at large minor radii is captured well by the radial trace of HeI. While HeII does not show a clear enhancement of the emission, neutral helium shows a clear local bump. At the target z the double concentric tube is not as clear as at other z, as figure 7.5 reveals. A first hypothesis as to what causes the hollow tubes to appear is that these in fact coincide with the location of rational surfaces in the q-profile. MHD modes of low order are known to be frequently excited in tokamak discharges, forming isolated surfaces of finite thickness.

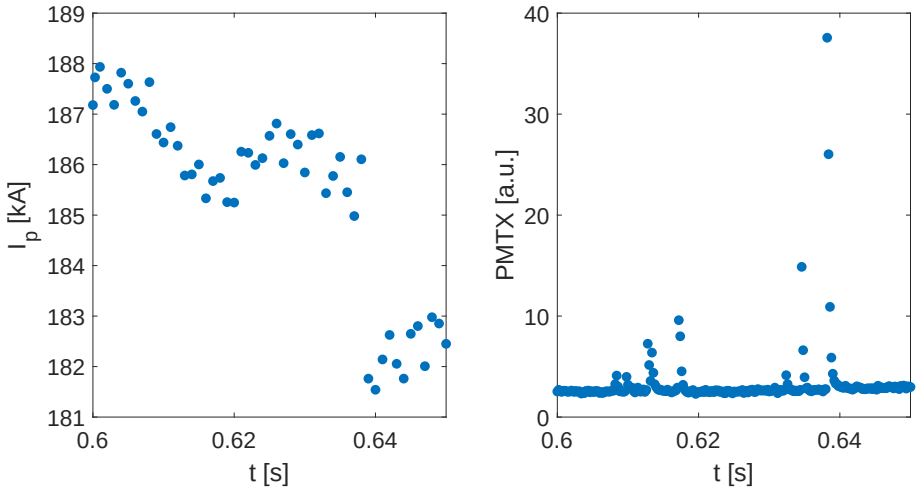

Figure 7.4: Plasma current and PMTX signals around the times for which MultiCam frames are shown in figure 7.3. The observation of the emission tube expansion for HeI coincides with a rapid loss of plasma current and a spike in the hard X-ray signal.

These islands have been found to be capable of harbouring runaway electrons in previous experimental studies, forming nested beams. If the modes are sufficiently separated in space they can act as transport barriers in chaotic transport processes, hindering suprathermal electrons in their cross field diffusion. The barrier effect is especially pronounced for highly energetic electrons [88, 89]. As the runaways in nested surfaces can locally excite the background gas, hollow surfaces of emissivity could be formed around these locations where the high energy RE density peaks.

The hypothesis is supported using the magnetic equilibrium reconstruction from LIUQE. Rational magnetic surfaces are computed and shifted by a fixed amount so that the rings are concentric with those in the emission profile. The required translation is roughly $(R, z) = (0.02, -0.01)$ m. This corresponds to an orbit shift for electrons at several tens of MeV according to equation (2.16). The result is shown in figure 7.8 for the $q = 3/2$ and $q = 2$ surfaces. Good agreement in their location is found, indicating that the formulated explanation for the existence of the tubes is a promising start for further analysis. Note that more intricate electron orbit simulations are needed to find the dependency of the location of the effective rational surfaces for electrons on their energy and pitch angle. Also, verification of RE excitation of the background gas as driving emission source is needed. A study of collision cross sections, such as the one addressed in section 3.4, is required to assess if the energies and densities the REs need to cause significant excitation are realistic.

As shown, emissivities for different species can offer unique spatial information on the runaway and impurity population. The resolution of the system is sufficient to resolve the emission contribution of different ionization stages to the 5 mm level.

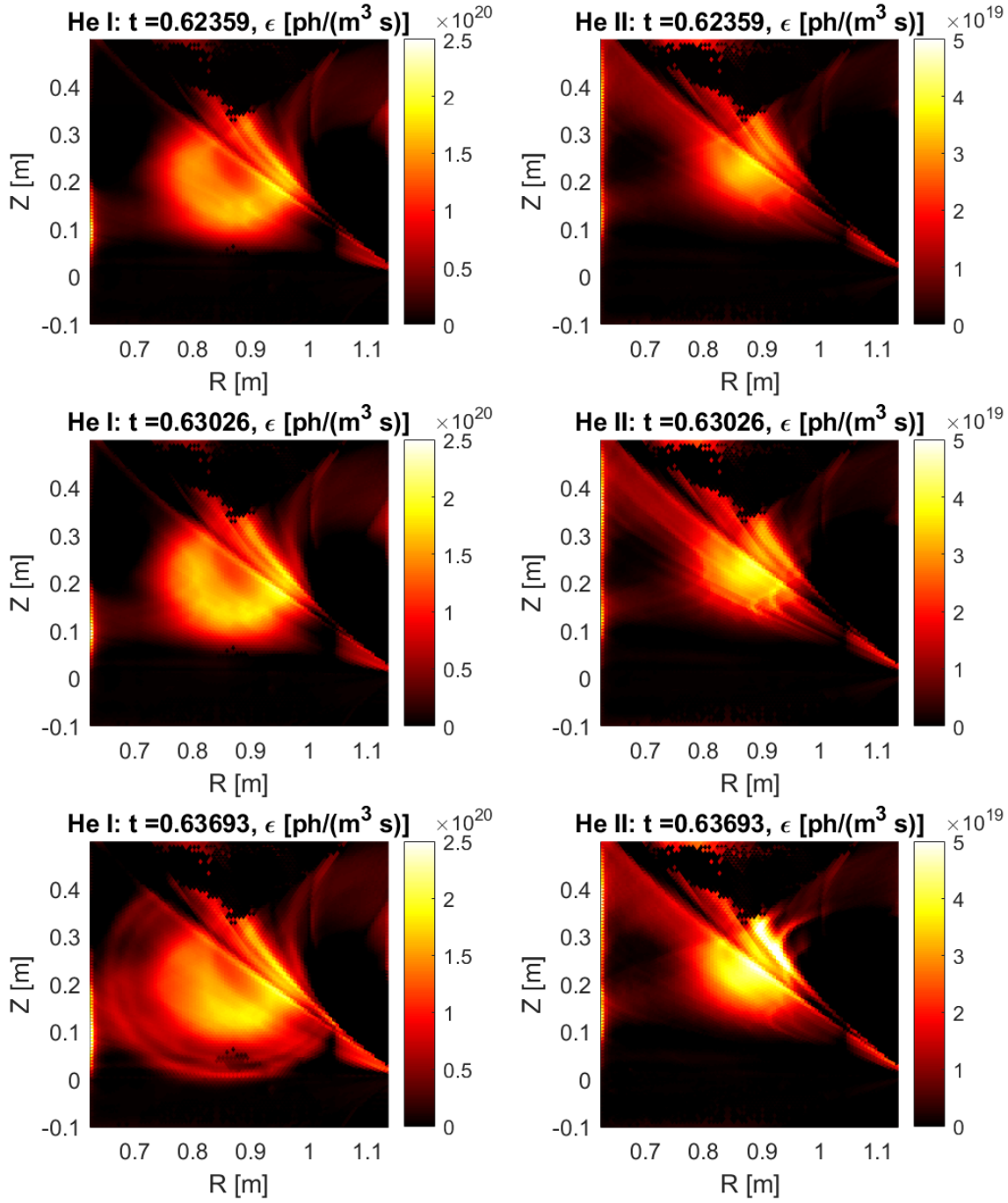

Figure 7.5: 2D emissivity reconstructions for the images presented in 7.3. The concentric tubes in the HeI pattern are resolved by the inversion, as well as the difference in tube size between the HeI and HeII channels. Artefacts cut-off the top right half in all cases.

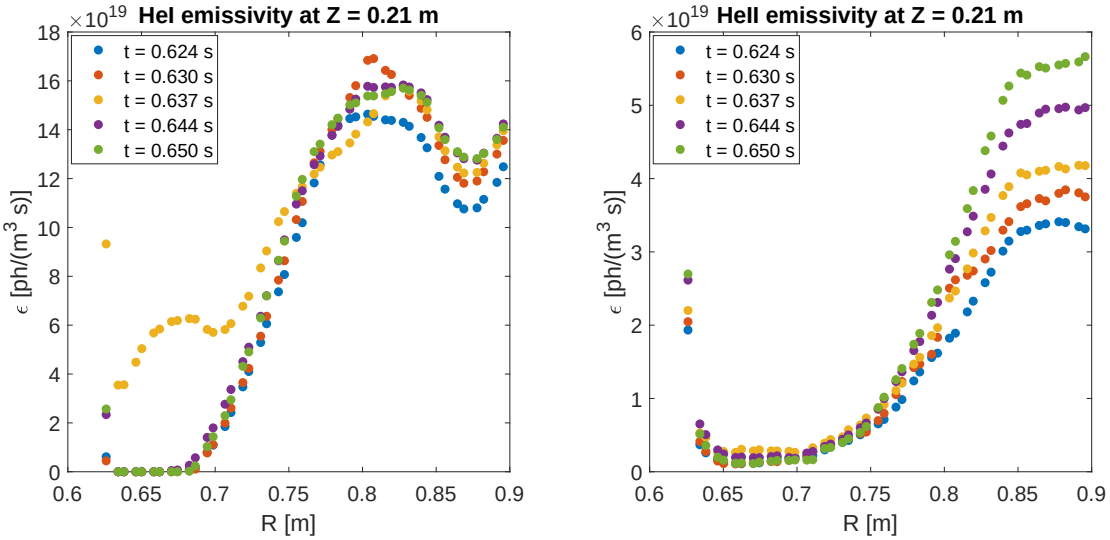

Figure 7.6: Time evolution of radial HeI and HeII emissivity profile for emission elements with their geometrical center at $z = 0.210 \pm 0.002$ m.

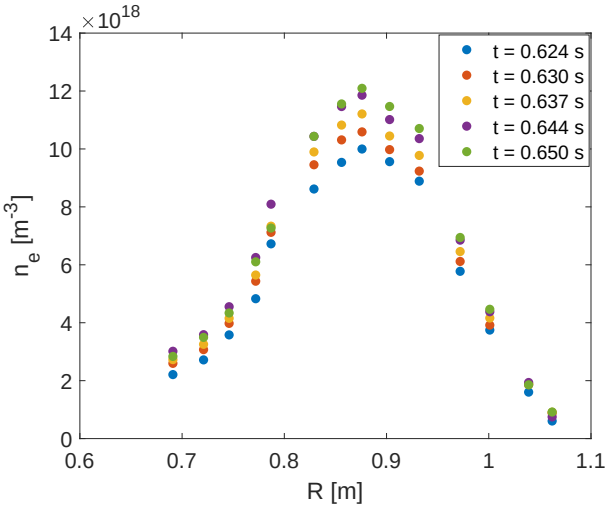

Figure 7.7: Electron density estimate as a function of major radius, obtained using the Mach-Zehnder interferometer at TCV. The density profile evolution matches changes in the HeII emissivity profile.

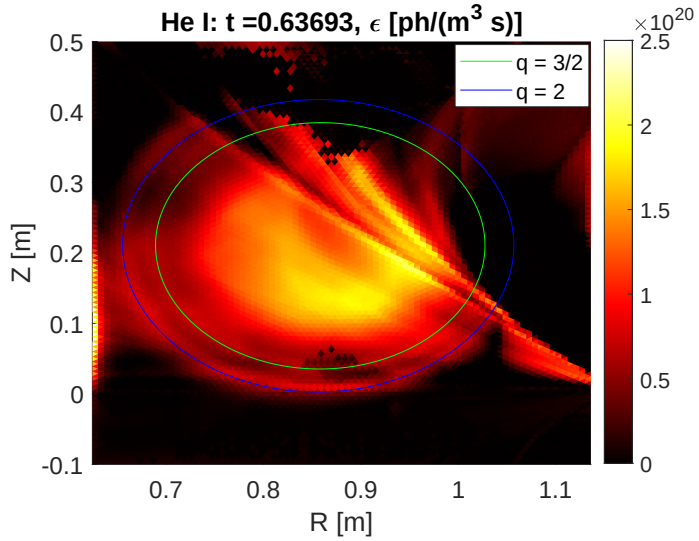

Figure 7.8: Shifted rational q surfaces from LIUQE on top of the HeI emissivity profile during the runaway expulsion event in shot 64723. A shift of $(R, z) = (0.02, -0.01)$ m is required to match the location of the concentric emission rings.

7.3 Conclusions

The work presented in this chapter gives on overview of the challenges specific to 2D line emissivity reconstruction in runaway experiments. Also, the applicability of multispectral systems and interpretive CRMs in studying different characteristic phases of RE discharges was discussed. A brief study on spatial He ionization state distributions was presented as a test case. The conclusions drawn are summarized here.

When recording line emission in runaway experiments two specific issues to deal with are X-ray snow and continuum background pollution. The former can render imaging of weak emission lines during the post-disruptive phase non feasible without additional X-ray shielding. This is due to the fact that the X-rays impose a maximum exposure time above which they cloud the complete image. Optical cavity based systems such as MANTIS combat the issue through maximizing light retention. With regard to the removal of synchrotron emission from line radiation images, it is found that this introduces uncertainties when the projection of the surface of visibility overlaps with the impurity emission location.

The characteristic time scale of plasma dynamics during different discharge phases in combination with the maximum 1 kHz acquisition rate of the system, determine which of these phases can be captured:

> *Emissivity reconstructions at the mm accuracy level can be performed for images acquired during the quiescent and post-disruptive phase of a discharge. Propagation of image errors to the inversion have now been quantified.*

Thermal quenches and breakdowns are too fast for the system to automatically adjust gain and exposure. Also, very few frames of a single event would be available without an increase of the frame rate.

Extraction of plasma parameter estimates from the emissivity profiles relies on the incorporation of the appropriate collisional radiative processes in rate equation coefficients.

> *Estimates of temperature, density and ionization distributions can be obtained for quiescent companion plasmas at high temperatures. Extraction of such information from post-disruptive plasmas requires one to self-consistently incorporate runaway driven excitation processes [22].*

Obtaining information on core plasma impurities and parameters during the quiescent phase requires imaging of high atomic number, high ionization state particles. Emissivity patterns obtained from impurities at low temperatures is mainly interesting in the post-disruptive phase. Tests have been performed using emission from HeI and HeII, with the result that:

> *Local HeI and HeII distributions can be resolved in the 2D poloidal plane with at least a 5 mm spatial resolution. Obtained profiles are found to be consistent with magnetic equilibrium reconstructions.*

A reconstruction analysis is performed for shot 64723. This experiment draws attention due to observed runaway current expulsion events in the post-disruptive phase. Changes in the HeII emissivity are attributed to the electron density evolution, but this can not explain behaviour observed in the HeII emission. During the expulsion event itself concentric rings of emission are visible for neutral helium. These are hypothesized to match the location of rational magnetic islands locally reducing the runaway transport coefficient.

Chapter 8

The value of multispectral imaging systems for runaway studies

On the basis of knowledge obtained throughout the exploration of multispectral imaging applications in runaway electron studies, answers to the posed research questions from section 1.6 are formulated in this section. In essence these summarize the conclusions drawn in sections 6.6 and 7.3. Using the results presented in this work as a starting point, a direction for future research is set out.

8.1 Outcome of the feasibility study

Runaway electrons have the potential to carry many mega Ampères of plasma current after a disruption event in future tokamaks. Formation and subsequent loss of control of a runaway beam would irreversibly damage the device. To understand runaway electron behaviour and design avoidance strategies and mitigation techniques, accurate models are required. Validation of these models requires comparison to experiment. Doing so, knowledge of plasma parameters such as temperature, density and impurity distributions is needed. Furthermore one would like to probe the evolution of the runaway distribution function to asses how these parameters affect the runaways. A diagnostic which has the potential to provide valuable information on both fronts is the multispectral imaging system. These devices image several plasma emission lines at different wavelengths simultaneously, from an almost identical camera view. An exploration of the potential of such systems, in specific the MANTIS systems, for runaway studies was presented in this work. The exploration was guided by two questions, the first one being:

> What part of electron phase-space can be detected and identified using visible synchrotron radiation and the synthetic runaway diagnostic SOFT?

To investigate whether synchrotron radiation can be detected during runaway experiments in the TCV tokamak, a 4 camera multispectral imaging system is installed on it middle port. Detection of direct light from relativistic electrons is not evident on forehand due to the relatively low magnetic field in combination with the visible light detection range of the system. During the quiescent phase of a number of high loop voltage discharges, synchrotron emission is recorded on channels not showing line emission pollution.

Using the synthetic synchrotron diagnostic SOFT an attempt is made at tracing back the origin of the light. Comparison of geometrical features in the experimental data and artificial patterns leads to the conclusion that runaway electrons require a high pitch angle and energy, $(p, \Theta) \approx (50\ m_e c, 0.50\ \text{rad})$, to generate the observed structures. Furthermore, only beams with a normalized radius larger than 0.8 are consistent with the observations. This knowledge of the energy, direction of movement and location of the particles forms the necessary starting point for (kinetic) model validation on the basis of these TCV experiments.

An attempt is made to support these conclusions using patterns obtained through different narrowband filters. The unique capability of multispectral imaging systems to compute synchrotron ratio distributions over full images is discussed. Qualitative agreement between experiments and SOFT behaviour of the ratio spread is found. Furthermore, SOFT is used to illustrate that neglecting the highly anisotropic nature of synchrotron radiation can lead to misleading interpretations of spectrometer recordings. It is eventually concluded that an idea of the shape of the electron distribution function in needed to accurately pinpoint the experimentally observed part of phase-space through spectral methods.

The clarity of the geometrical features observed is unique, and is successfully used to validate specific components of SOFT behaviour. Using the equilibrium control system at TCV, the runaways are moved vertically to observe changes in the pattern geometry. The geometrical behaviour is reproduced well by SOFT as discussed elaborately in a submitted paper by Hoppe et al [84].

The second component to the feasibility study is related to the information which can be obtained from line emission:

> Can the MultiCam system generate 2D poloidal emissivity maps on temporal and spatial scales relevant to kinetic runaway models?

Knowledge of the impurity distribution can serve as valuable input for runaway formation and mitigation models. Multispectral systems can provide the images required to construct 2D emissivity maps in the poloidal plane. If suitable collisional radiative models are available these can be used to estimate plasma parameters such as the electron temperature, electron and impurity density distributions and the ionization distribution.

The MultiCam system is used to image, among other lines, HeI and an HeII emission in pre- and post-disruptive plasma conditions. Given the 1 kHz acquisition rate limit, dynamics during the thermal quench cannot be resolved, and emission dynamics in fast RE loss processes can at best be captured in a few frames. Impurity distribution changes on longer time scales in the quiescent and flat-top beam phase are shown to be resolvable by the system. Extensive system developments over the years now allow for quantitative reconstruction of the emissivity profile with known error bars and mm scale spatial resolution. It is shown that the two helium ionization stages can be separated in space yielding information on the plasma structure not resolved by other available diagnostics.

Extracting knowledge on plasma parameters in the post-disruptive phase requires incorporation of runaway interactions with the background gas in collisional radiative model. Currently such frameworks are still under development within the community. Simultaneous development of multispectral systems can open the way to validation of these complex models in experiments.

Based on the results presented in this work, it is concluded that multispectral systems can provide unique input to runaway electron models. Further extension of the use of MANTIS systems in the domain of RE studies is deemed a rewarding path to follow.

8.2 Future directions

The statement that multispectral imaging systems can provide valuable and unique contributions to experimental validation in the field of runaway research, implies that the conclusions drawn here are a starting point rather than a closing statement. Much of the potential of the obtained data and the system in itself remain unexplored. The remainder of this chapter will sketch paths worth following in the continuation of this research.

8.2.1 Kinetic studies for TCV MST1 results

Using SOFT, the part of phase-space contributing to the synchrotron patterns observed during the MST1 campaign was identified. This information can be used as a basis for kinetic studies on the distribution function evolution in the quiescent stage of the discharge. Such an undertaking is deemed worthwhile to (i) support RE formation and transport models, and (ii) reveal if the distribution function shape is related to the fact that no post-injection RE beam was formed when pre-injection synchrotron radiation was observed.

A first step is an analysis of plasma parameter influence on RE creation using the 0D kinetic modelling tool CODE [40, 53]. This code includes a wide variety of collision- and avalanche operators and includes radiation reactions in the form of synchrotron and brehmstrahlung emission. Motivation for the use of this framework is its high computational efficiency, allowing one to scan a great deal of scenarios and collision descriptions. Phenomena it can not capture are the influence of spatially non-uniform plasma parameters and the effects of transport. The latter can be approximated through the use of a suitable sink term. This is needed to explain why the population in the observed momentum and pitch angle region saturates after about 300 ms.

At least three specific phenomena observed in the MultiCam videos call for specific attention. Firstly, after saturation the intensity of the synchrotron patterns fluctuates in time. Either fluctuations in plasma parameter cause a continuous imbalance of source and sink terms, or the population itself in prone to instabilities. Identification of these instabilities can help specifying runaway loss mechanisms in models, and reveal channels of runaway seed loss which could be used to avoid avalanche generation during a disruption.

Secondly, the runaway current loss events during the post-disruptive phase require additional attention. At this point it is unclear what the nature of the instability is. Knowledge of RE loss processes during this stage is important in designing beam control and mitigation techniques. Furthermore, with the use of a runaway-gas interaction cross section the hypothesis on the presence of transport reducing magnetic islands can be tested. If consistent, this experimental observation provides backup for transport theories of runaways in predominantly stochastic fields.

A third observation which has sparked interest is a sudden change in the synchrotron pattern during shots 64711 and 64799. As shown in figure 8.1 the event is accompanied by a sudden increase in current and a more gradual drop in loop voltage. This could point towards avalanching, during which the number of REs and thus the current increase while the resistivity and loop voltage drop. As energetic runaways give away energy to initially slow electrons, the high momentum part of phase-space could be drained. This hypothesis in reinforced by the movement of the observed pattern to the high field side, where it has been shown that lower energy particles emit their light in the MultiCam direction. This mechanism might thus explain the change of pattern and loss of observed radiation intensity. What would cause such a sudden transition to significant avalanching is unclear at this stage, and requires kinetic modelling.

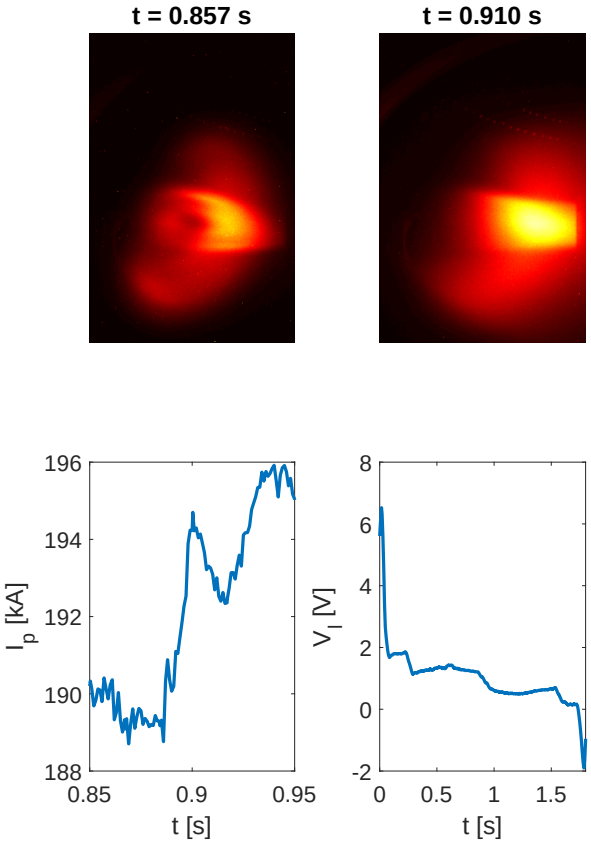

Figure 8.1: Synchrotron patterns observed in shot 64799, where a sudden change occurred around 0.88 s. The plasma current around this time shows a quick increase, and the loop voltage around this point in time a more gradual decrease.

8.2.2 Emissivity studies in runaway companion plasmas

While significant attention has been devoted to extracting information from the observed synchrotron patterns in this work, the analysis performed on the obtained emission profiles is limited. With the currently available data much is still to be explored, such as the accuracy of using ADAS coefficients in the pre-injection phase. Since TCV has other diagnostics capable of estimating temperatures and densities the analysis method can be tested. Furthermore, understanding the emissivity dynamics of the post-disruptive plasma requires a careful look at what influence runaways have on the excitation of the atoms using newly developed models [22].

Improvements in the inversion profiles can be made on both the analysis and system side. Many steps have been taken to obtain a reliable conversion from camera signal to absolute emissivity, and putting error bars on the obtained results. Despite this, non-physical artefacts remain present in the inversions. Improvements in the geometry matrix construction through sight line interpolation appears a promising path to better results. The same goes for image pre-processing using signal to noise ratio based masks. Furthermore, emission profile constraining could be improved with the use of multiple multispectral systems installed at different ports. The new, highly flexible, MANTIS+ systems will make this possible in the near future.

In future runaway experiments it is worthwhile to install filters for high ionization states of high atomic number species. These will allow 2D resolved local temperature estimates in the plasma core of the quiescent phase. At the same time knowledge of impurity transport near the runaway beam can provide information on how the two interact. Performing studies on tokamaks other than TCV seems feasible with the extension of the multispectral system family, especially given that the new devices are light, compact and easy to relocate. It should be noted that installation on reactors with highly reflective walls calls for more intricate ray tracing methods to construct the geometry matrix than the one currently employed.

Apart from potential upgrades to the method of acquiring emissivity profiles, the dataset currently available harbours some more phenomena to explore as well. Firstly, as shown in the bottom windows of figure 7.3, post-disruptive emission profiles frequently show helical traces of increased intensity. These are hypothesized to originate from locally enhanced emission by runaway driven excitation. Using software such as Calcam one can set constraints on the trajectory of the particles. The spatial origin of the emission and possibly the runaways can be traced back. Combined with runaway driven excitation cross-sections, one might be able to check if these traces are consistent with distribution function estimates or indicate the presence of RE trapping magnetic islands.

8.2.3 Polarization and infrared imaging

In the near future the MANTIS systems will be equipped with a new type of polarization camera. Using pixel to pixel coatings, 2D images in 4 different polarization orientations can be recorded. While not originally meant to support runaway studies, also this extension to the system could prove to be a valuable addition when studying the runaway population. As explained when SOFT was introduced in section 2.5.2, only part of the electron emission cone lands on the detector. Since the electric field direction of light emitted by a charged particle is perpendicular to the velocity vector and magnetic field, the radiation reaching the detector is linearly polarized. SOFT can keep track of the polarization details. For a given magnetic field, electron distribution and camera geometry the fraction of linearly polarized light over the observed synchrotron pattern can be predicted. This provides an additional parameter to constrain the experimentally observed part of momentum space in experimental data.

Simultaneous 2D imaging of synchrotron radiation patterns using 4 different polarization directions would be yet another unique way in which the MANTIS line of systems can shine light on the runaway problem. In combination with recording light in a few different spectral regions, multispectral systems would have access to three complementary methods of extracting information on the energy, pitch angle and location of the runaway beam.

Another addition to the MANTIS system worth considering is the installation of an infrared camera. As was shown in figure 6.10, the dominant part of phase-space depends on the spectral range of the sensor. Extending multispectral systems outside of the visible range, different parts of the runaway population could be constrained. Knowledge on the dynamics of two regions in momentum- and real-space would greatly increase the level of confidence obtained by matching kinetic model results to experimental observations.

Bibliography

[1] J. P. Freidberg. *Plasma Physics and Fusion Energy*. Cambridge University Press, 2007. 1, 2, 6, 8, 25

[2] T. F. Stocker et al. Sumary for policymakers. In *Climate Change 2013: The Physical Science Basis. Contribution of Working Group I to the Fifth Assessment Report of the Intergovernmental Panel on Climate Change*, chapter 1. Cambridge University Press, Cambridge, 2013. 1

[3] N. J. Lopes Cardozo, A. G. G. Lange, and G. J. Kramer. Fusion: Expensive and taking forever? *Journal of Fusion Energy*, 35(1):94–101, 2016. 1

[4] C. W. Horton and S. Benkadda. Machine architecture and objectives. In *ITER Physics*, chapter 1. World Scientific Publishing, Singapore, 2015. 1, 8, 90

[5] E. M. Hollmann et al. Plasma–surface interactions during tokamak disruptions and rapid shutdowns. *Journal of Nuclear Materials*, 415(1, Supplement):S27 – S34, 2011. Proceedings of the 19th International Conference on Plasma-Surface Interactions in Controlled Fusion. 1, 2, 7

[6] J. W. Connor and R. J. Hastie. Relativistic limitations on runaway electrons. *Nuclear Fusion*, 15(3):415–424, 1975. 2, 7

[7] R. J. E. Jaspers. *Relativistic runaway electrons in tokamak plasmas*. PhD thesis, Technische Universiteit Eindhoven, Department of Applied Physics, 1995. 2, 6, 9, 10, 11, 12, 68

[8] M. Hoppe. *Simulation and analysis of radiation from runaway electrons*. Licentiate thesis, Chalmers University of Technology, Department of Physics, 2019. 2, 7, 8, 16

[9] L. Hesslow, O. Embréus, G. J. Wilkie, G. Papp, and T. Fülöp. Effect of partially ionized impurities and radiation on the effective critical electric field for runaway generation. *Plasma Physics and Controlled Fusion*, 60(7):074010, 2018. 2, 7, 62, 90, 91

[10] M. Vlainic et al. Post-disruptive runaway electron beams in the COMPASS tokamak. *Journal of Plasma Physics*, 81(5):475810506, 2015. 2

[11] D. J. Griffiths. Radiation. In *Introduction to Electrodynamics*, chapter 11. Pearson, Boston, United States, 4 edition, 2013. 2, 92

[12] Z.Y. Chen et al. Enhancement of runaway production by resonant magnetic perturbation on J-TEXT. *Nuclear Fusion*, 56(7):074001, 2016. 2

[13] D. Carnevale et al. Runaway electron beam control. *Plasma Physics and Controlled Fusion*, 61(1):014036, 2018. 2

[14] G. Papp, M. Drevlak, T. Fülöp, P. Helander, and G. I. Pokol. Runaway electron losses caused by resonant magnetic perturbations in ITER. *Plasma Physics and Controlled Fusion*, 53(9):095004, 2011. 2, 11

[15] J. Mlynar et al. Runaway electron experiments at COMPASS in support of the EUROfusion ITER physics research. *Plasma Physics and Controlled Fusion*, 61(1):014010, 2018. 2

[16] P. Martin et al. Physics, control and mitigation of disruptions and runaway electrons in the EUROfusion Medium Size Tokamaks science programme. In *Proceedings 26th IAEA Fusion Energy Conference*, 2016. 2, 5, 7

[17] K. Wongrach et al. Runaway electron studies in TEXTOR. *Nuclear Fusion*, 55(5):053008, 2015. 2

[18] K. Gál, T. Fehér, H. Smith, T. Fülöp, and P. Helander. Runaway electron generation during plasma shutdown by killer pellet injection. *Plasma Physics and Controlled Fusion*, 50(5):055006, 2008. 2

[19] L. Hesslow et al. Effect of partially screened nuclei on fast-electron dynamics. *Physical Review Letters*, 118:255001, 2017. 2

[20] D. Hu, E. Nardon, M. Lehnen, G. T. A. Huijsmans, and D. C. van Vugt. 3D non-linear MHD simulation of the MHD response and density increase as a result of shattered pellet injection. *Nuclear Fusion*, 58(12):126025, 2018. 2

[21] M. Landreman, A. Stahl, and T. Fülöp. Numerical calculation of the runaway electron distribution function and associated synchrotron emission. *Computer Physics Communications*, 185(3):847 – 855, 2014. 2, 18

[22] N. A. Garland et al. Impact of a minority relativistic electron tail interacting with a thermal plasma containing high-atomic-number impurities. 2019. 2, 23, 72, 80, 83

[23] G. Papp et al. The effect of ITER-like wall on runaway electron generation in JET. *Nuclear Fusion*, 53(12):123017, 2013. 2

[24] A. Stahl, M. Landreman, G. Papp, E. Hollmann, and T. Fülöp. Synchrotron radiation from a runaway electron distribution in tokamaks. *Physics of Plasmas*, 20(9):093302, 2013. 3, 50, 69

[25] M. Hoppe et al. SOFT: a synthetic synchrotron diagnostic for runaway electrons. *Nuclear Fusion*, 58(2):026032, 2018. 3, 13, 14

[26] W. A. J. Vijvers et al. Conceptual design and proof-of-principle testing of the real-time multispectral imaging system MANTIS. *Journal of Instrumentation*, 12(12):C12058–C12058, 2017. 3

[27] A. Perek et al. MANTIS: A real-time quantitative multispectral imaging system for fusion plasmas. *Review of Scientific Instruments*, 90(12):123514, 2019. 3, 30

[28] T. Ravensbergen et al. Real-time detection of the radiation front during divertor detachment using multispectral imaging. *submitted to Nuclear Fusion*, 2019. 3, 30

[29] W. Gonzalez et al. Conceptual studies on spectroscopy and radiation diagnostic systems for plasma control on demo. *Fusion Engineering and Design*, 2019. 4

[30] W. Biel et al. Diagnostics for plasma control – from ITER to DEMO. *Fusion Engineering and Design*, 146:465 – 472, 2019. 4

[31] V. V. Plyusnin et al. Comparison of runaway electron generation parameters in small, medium-sized and large tokamaks—a survey of experiments in COMPASS, TCV, ASDEX-upgrade and JET. *Nuclear Fusion*, 58(1):016014, 2018. 5, 11, 25, 26, 90

[32] S. Coda et al. Overview of the TCV tokamak program: scientific progress and facility upgrades. *Nuclear Fusion*, 57(10), 2017. 5, 25

[33] G. Fussmann. On the motion of runaway electrons in momentum space. *Nuclear Fusion*, 19(3):327–334, 1979. 6

[34] I. Entrop. *Confinement of relativistic runaway electrons in tokamak plasmas*. PhD thesis, Technische Universiteit Eindhoven, Department of Applied Physics, 1999. 6, 9, 10, 11

[35] H. Dreicer. Electron and ion runaway in a fully ionized gas. I. *Physical Review*, 115:238–249, Jul 1959. 6

[36] A. Stahl, E. Hirvijoki, J. Decker, O. Embréus, and T. Fülöp. Effective critical electric field for runaway-electron generation. *Physical Review Letters*, 114:115002, 2015. 7

[37] L. Hesslow. *Effect of Partial Screening on Runaway-Electron Dynamics*. Licentiate thesis, Chalmers University of Technology, Department of Physics, 2018. 7, 90

[38] A. Stahl, O. Embréus, M. Landreman, G. Papp, and T. Fülöp. Runaway-electron formation and electron slide-away in an ITER post-disruption scenario. *Journal of Physics: Conference Series*, 775:012013, 2016. 7, 8

[39] G. Papp. *The role of magnetic perturbations in runaway electron and sawtooth dynamics*. PhD thesis, Chalmers University of Technology, Department of Physics, 2013. 7

[40] A. Stahl. *Momentum-space dynamics of runaway electrons in plasmas*. PhD thesis, Chalmers University of Technology, Department of Physics, 2017. 7, 8, 18, 82

[41] H. M. Smith, T. Fehér, T. Fülöp, K. Gál, and E. Verwichte. Runaway electron generation in tokamak disruptions. *Plasma Physics and Controlled Fusion*, 51(12):124008, 2009. 8

[42] M. N. Rosenbluth and S. V. Putvinski. Theory for avalanche of runaway electrons in tokamaks. *Nuclear Fusion*, 37(10):1355–1362, 1997. 8

[43] C. J. McDevitt, Z. Guo, and X. Tang. Avalanche mechanism for runaway electron amplification in a tokamak plasma. *Plasma Physics and Controlled Fusion*, 61(5):054008, 2019. 8

[44] S. Coda. Progress and scientific results in the TCV tokamak. *Nuclear Fusion*, 51(9):094017, 2011. 8

[45] A. H. Boozer. Magnetic surface loss and electron runaway. *Plasma Physics and Controlled Fusion*, 61(2):024002, 2019. 8

[46] L. Hesslow, O. Embréus, O. Vallhagen, and T. Fülöp. Influence of massive material injection on avalanche runaway generation during tokamak disruptions. *Nuclear Fusion*, 59(8):084004, 2019. 8

[47] R. J. Zhou, L. Q. Hu, Y. Zhang, G. Q. Zhong, and S. Y. Lin. Runaway electrons generated during spontaneous disruptions in the EAST tokamak. *Nuclear Fusion*, 57(11):114002, 2017. 9

[48] A. J. Russo. Effect of ripple on runaway electrons in tokamaks. *Nuclear Fusion*, 31(1):117–126, 1991. 10

[49] C. Paz-Soldan et al. Kink instabilities of the post-disruption runaway electron beam at low safety factor. *Plasma Physics and Controlled Fusion*, 61(5):054001, 2019. 11

[50] M. Fouka and S. Ouichaoui. Analytical fits to the synchrotron functions. *Research in Astronomy and Astrophysics*, 13(6):680–686, 2013. 12

[51] I.M. Pankratov. Analysis of the synchrotron radiation spectra of runaway electrons. *Plasma Physics Reports*, 25(2):145–148, 1999. 13

[52] J. M. Moret et al. Tokamak equilibrium reconstruction code LIUQE and its real time implementation. *Fusion Engineering and Design*, 91:1 – 15, 2015. 15

[53] A. Stahl, O. Embréus, G. Papp, M. Landreman, and T. Fülöp. Kinetic modelling of runaway electrons in dynamic scenarios. *Nuclear Fusion*, 56(11):112009, 2016. 18, 82

[54] O. Embréus, A. Stahl, and T. Fülöp. On the relativistic large-angle electron collision operator for runaway avalanches in plasmas. *Journal of Plasma Physics*, 84(1):905840102, 2018. 18

[55] G. Zehua, T. Xian-Zhu, and C. J. McDevitt. Models of primary runaway electron distribution in the runaway vortex regime. *Physics of Plasmas*, 24(11):112508, 2017. 18

[56] T. Fülöp, G. Pokol, P. Helander, and M. Lisak. Destabilization of magnetosonic-whistler waves by a relativistic runaway beam. *Physics of Plasmas*, 13(6):062506, 2006. 19

[57] U. Fantz. Basics of plasma spectroscopy. *Plasma Sources Science and Technology*, 15(4):S137–S147, 2006. 20

[58] R. J. E. Jaspers. Plasma Spectroscopy. *Fusion Science and Technology*, 61(2T):384–393, 2012. 20, 33

[59] R. W. P. McWhirter. Spectral intensities. In *Plasma Diagnostic Techniques*. Academic Press, 1966. 20

[60] H. P. Summers. The adas user manual. `http://www.adas.ac.uk/manual.php`, 2004. 21, 94

[61] C. A. Johnson, S. D. Loch, and D. A. Ennis. ColRadPy: a Python collisional radiative solver. *Nuclear Materials and Energy*, 20:100579, 2019. 21, 22

[62] H. P. Summers et al. Ionization state, excited populations and emission of impurities in dynamic finite density plasmas: I. the generalized collisional–radiative model for light elements. *Plasma Physics and Controlled Fusion*, 48(2):263–293, 2006. 21, 22, 23

[63] J. M. Muñoz Burgos, O. Schmitz, S. D. Loch, and C. P. Ballance. Hybrid time dependent/independent solution for the He I line ratio temperature and density diagnostic for a thermal helium beam with applications in the scrape-off layer-edge regions in tokamaks. *Physics of Plasmas*, 19(1):012501, 2012. 22, 23

[64] A. Pospieszczyk. Spectroscopy. *Fusion Science and Technology*, 53(2T):417–424, 2008. 23

[65] G. Papp et al. Runaway electron generation and mitigation on the European medium sized tokamaks ASDEX Upgrade and TCV. In *Proceedings 26th IAEA Fusion Energy Conference*, 2016. 25, 26

[66] E. Nardon et al. On the mechanisms governing gas penetration into a tokamak plasma during a massive gas injection. *Nuclear Fusion*, 57(1):016027, 2016. 25

[67] G. Pautasso et al. Disruption mitigation by injection of small quantities of noble gas in ASDEX Upgrade. *Plasma Physics and Controlled Fusion*, 59(1):014046, 2016. 25, 26

[68] A. J. Thornton et al. Plasma profile evolution during disruption mitigation via massive gas injection on MAST. *Nuclear Fusion*, 52(6):063018, 2012. 25

[69] R. Jaspers et al. Islands of runaway electrons in the textor tokamak and relation to transport in a stochastic field. *Physical Review Letters*, 72:4093–4096, 1994. 25, 74

[70] Y. Peysson et al. Modeling runaway electrons dynamics in tokamak plasmas: progresses and challenges. In *Proceedings 27th IAEA Fusion Energy Conference*, 2018. 25

[71] A. H. Boozer. Runaway electrons and magnetic island confinement. *Physics of Plasmas*, 23(8):082514, 2016. 25

[72] Zemax. OpticStudio. `https://www.zemax.com/products/opticstudio`. Accessed: 04/09/2019. 28

[73] E. Hecht. Geometrical Optics. In *Optics*, chapter 6, pages 243–277. Pearson, 5 edition, 2016. 29

[74] C. B. Hitz, J. J. Ewing, and J. Hecht. Interference. In *Introduction to Laser Technology*, chapter 4. IEEE Press, Canada, 2012. 32

[75] J. A. Dobrowolski. Optical properties of films and coatings. In *Handbook of Optics I*, chapter 42, pages 1–130. McGraw-Hill, 1995. 33, 96, 97

[76] A. Kramida, Y. Ralchenko, J. Reader and NIST ASD Team. NIST Atomic Spectra Database. `https://physics.nist.gov/asd`, 2018. 33

[77] A. Meakins S. Silburn and T. Farley. euratom-software/calcam: Calcam v2.2. `https://github.com/euratom-software/calcam/tree/v2.2.0`, 2019. 34, 35, 39

[78] S. N. Luko. The "coupon collector's problem" and quality control. *Quality Engineering*, 21(2):168–181, 2009. 37

[79] A. H. Andersen and A. C. Kak. Simultaneous Algebraic Reconstruction Technique (SART): A superior implementation of the ART algorithm. *Ultrasonic Imaging*, 6(1):81–94, 1984. 38, 39

[80] M. Carr et al. Physically principled reflection models applied to filtered camera imaging inversions in metal walled fusion machines. *Review of Scientific Instruments*, 90(4):043504, 2019. 39

[81] M. Carr et al. Description of complex viewing geometries of fusion tomography diagnostics by ray-tracing. *Review of Scientific Instruments*, 89(8):083506, 2018. 39

[82] J. Mlynar et al. Current research into applications of tomography for fusion diagnostics. *Journal of Fusion Energy*, 38(57):102001, 2018. 39

[83] M. Hoppe, O. Embréus, C. Paz-Soldan, R. A. Moyer, and T. Fülöp. Interpretation of runaway electron synchrotron and bremsstrahlung images. *Nuclear Fusion*, 58(8):082001, 2018. 46

[84] M. Hoppe, G. Papp, T. A. Wijkamp, A. Perek, J. Decker, B. Duval, O. Embréus, T. Fülöp, U. A. Sheikh, TCV team, and EUROfusion MST1 Team. Runaway electron synchrotron radiation in a vertically translated plasma. *submitted to Nuclear Fusion*, 2020. 57, 82

[85] L. Hesslow et al. Evaluation of the Dreicer runaway generation rate in the presence of high- Z impurities using a neural network. *Journal of Plasma Physics*, 85(6):475850601, 2019. 62

[86] Z. Guo, X. Tang, and C. J. McDevitt. Models of primary runaway electron distribution in the runaway vortex regime. *Physics of Plasmas*, 24(11):112508, 2017. 62

[87] Z. Y. Chen et al. Measurement of the internal magnetic fluctuation by the transport of runaways on J-TEXT. *Review of Scientific Instruments*, 87(11):11E304, 2016. 68

[88] S. Abdullaev. Transport of particles in a turbulent field. In *Magnetic Stochasticity in Magnetically Confined Fusion Plasmas: Chaos of Field Lines and Charged Particle Dynamics*, pages 295–331. Springer International Publishing, Cham, 2014. 68, 76

[89] N. J. Lopes Cardozo and M. Peters. Diffusion across a layered medium and relation to transport in thermonuclear plasmas. *Physics of Plasmas*, 2(11):4230–4235, 1995. 76

[90] J. R. Martín-Solís, A. Loarte, and M. Lehnen. Runaway electron dynamics in tokamak plasmas with high impurity content. *Physics of Plasmas*, 22(9):092512, 2015. 90

[91] L. Hesslow et al. Generalized collision operator for fast electrons interacting with partially ionized impurities. *Journal of Plasma Physics*, 84(6):905840605, 2018. 90

[92] J. D. Jackson. Radiation by moving charges. In *Classical Electrodynamics*, chapter 14. Wiley, New York, United States, 3 edition, 1999. 93

[93] T. Erdogan. Optics and Filter Knowledge. `https://www.semrock.com/optics-and-filter-knowledge.aspx`. Accessed: 11/09/2019. 96, 97

[94] D. B. Murhpy and M. W. Davidson. Illuminators, filters, and the isolation of specific wavelengths. In *Fundamentals of Light Microscopy and Electronic Imaging*, chapter 3, pages 35–51. John Wiley & Sons, 2012. 96

[95] Andover. bandpass filter fundamentals. `https://www.andovercorp.com/technical/bandpass-filter-fundamentals`. Accessed: 11/09/2019. 96

[96] J. Reichman. *Handbook of Optical Filters*. Chroma, 2010. 97

Appendix A

The effective critical field

Collisional scattering of electrons on partially ionized impurities is affected by the fact that bound electrons screen out part of the atomic charge. In fact, the interaction of slow electrons with impurities only depends on the ion charge, obeying the Coulomb collision law. The nuclear charge is completely screened by the bound electrons. As electrons gain more energy the situation changes. Fast electrons are able to penetrate the electron cloud of an impurity, probing the internal charges. This partial screening leads to an enhanced interactions with heavy species, as compared to what is predicted when only taking the net ion charge into account. Runaways will consequently slow down to a larger extend when they collide with the impurities. This effect is enhanced further by an increase in radiation losses due to large particle deceleration [37, 90].

A notable consequence of partial screening is the elevation of critical electric field. Experiments have shown values of E_c well above that predicted by equation (2.6) [31]. Hesslow and coworkers provide a rigorous approach to tackling the problem of electron-impurity interactions which appears to explain the discrepancy. A quantum-mechanical treatment of inelastic and elastic collisions as well as the electron charge density of the impurity, are employed to arrive at a suitable collision parameter to be used in a kinetic description of the plasma [91, 37]. Using this expression one can look for the minimum electric field at which particles overcome the deceleration due to radiative and collisional forces. The obtained effective critical field $E_{c,eff}$ must normally be solved iteratively. For the special case of one single dominant ionized state, an approximate analytical expression can be found. For a plasma with free electron density n_e, with a dominant impurity specie of atomic number Z_j in ionization state $Z_{s,j}$ present in a density $n_{Z,j}$, the effective critical field is approximated by the following set of equations [9]

$$\begin{aligned} E_{c,eff} &= E_c\Big(1+\frac{(Z_j-Z_{s,j})n_{Z,j}}{n_{e,tot}}\frac{1}{\ln(\Lambda_c)}(S_j+R_j\sqrt{\frac{B_\phi^2}{n_{e,tot20}}+\frac{0.9}{\ln(a_j)}})\Big) \\ \ln(\Lambda_c) &= \ln(\Lambda)+\frac{1}{2}\ln(\frac{m_ec^2}{T_e}) \approx 14.6+0.5\ln(\frac{T_{e,eV}}{n_{e,20}}) \\ S_j &= -\ln(I_j)-1+\frac{3}{2}\Big(1+\frac{1}{\ln(a_j)}\Big)\Big(\frac{Z_j}{3}\ln(a_j)\Big) \\ R_j &= 0.09(Z_j+Z_{s,j})\ln(a_j). \end{aligned} \tag{A.1}$$

In these expressions $\ln(\Lambda_c)$ is the relativistic Coulomb logarithm, B_ϕ the toroidal magnetic field and $n_{e,tot}$ the total electron density including bound electrons. Furthermore equation (A.1) contains a few specie specific parameters. The quantity a_j is the effective ion size, I_j the mean excitation energy normalized to the electron rest mass and S_j is the so called screening constant. For the ionization states of Ne and Ar their values are given in the Appendix of a paper by Hesslow et al [9]. Note that $n_{e,tot20}$ and $n_{e,20}$ are densities in units of 10^{20} m^{-3} and $T_{e,eV}$ is in electron volts.

In figure A.1 the effects of incorporating the radiation losses and partial screening on the critical field for a deuterium plasma with argon impurities are illustrated. Both E_c and $E_{c,eff}$ are displayed as a function of the argon ionization state at fixed density (A), and for a range of densities for a fixed singly charged state (B). The plasma parameters used resemble ITER design parameters. An on-axis toroidal field of 5.3 T, an electron temperature of 21 keV and a deuterium density n_D of 10^{20} m^{-3} are used for the calculations [4].

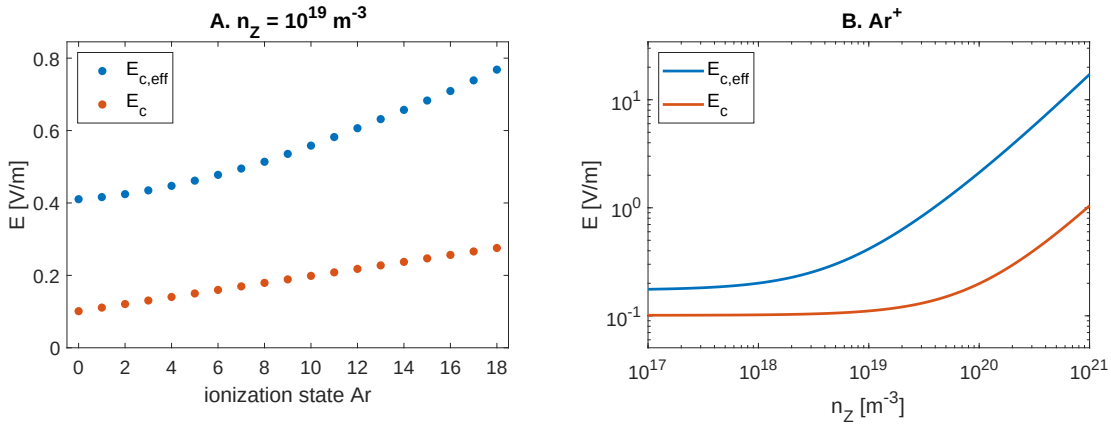

Figure A.1: Critical- and effective critical electric field for a D-Ar plasma with ITER-like parameters; $B_\phi = 5.3$ T, $T_e = 21$ keV and $n_D = 1 \cdot 10^{20}$ m^{-3}. Results were obtained using a critical field model by Hesslow et al [9]. A) E_c and $E_{c,eff}$ for all ionization states of Ar given a fixed ion density of 10^{19} m^{-3}. The ratio of the fully quantum mechanical to the classical results is especially large for low ionization states. B) E_c and $E_{c,eff}$ as a function of the ion density for single ionized Ar. The correction using the quantum treatment can for high densities exceed an order of magnitude.

The corrections that the quantum mechanical treatment gives on the critical field is evidently large from the results presented in figure A.1 A. Where E_c merely depends on the impurities through their contribution to the total free electron density, $E_{c,eff}$ shows more complicated behaviour. The discrepancy between the two quantities in terms of their ratio is largest for lower ionization states. For neutral argon $E_{c,eff}$ exceeds E_c by a factor of 4.6, while this is reduced to 2.9 for fully ionized argon. This can be explained by the fact that for high ionization states the influence partial screening is less significant, as there are fewer bound electrons.

Since the main difference between the theories underlying the two critical field calculations is the way in which the electron-impurity interaction is treated, it is to be expected that discrepancies are especially large for high impurity contents. This behaviour also emerges from the calculations presented in figure A.1 B. Note that when the deuterium and argon densities are of comparable magnitude, the effective critical field can exceed the classical one by over one order of magnitude. The decay characteristics of runaways after gas injection strongly depend on the electric field. From the example provided here, it is evident that having knowledge of the impurity charge state and density distributions is essential for predictive and interpretive modelling in mitigation studies.

Appendix B

Radiation from accelerating charges

In this section a classical treatment of charged particle radiation is presented, leading up to expressions for the emitted power pattern and intensity. The treatment departs from the Liénard-Wiechert potentials for an arbitrarily moving point charge q, velocity $\vec{v}$ accelerating with $\vec{a}$. The scalar potential V and vector potential $\vec{A}$ are given by [11]:

$$\begin{aligned} V(\vec{r},t) &= \frac{1}{4\pi\epsilon_0}\frac{qc}{\tilde{r}c - \vec{\tilde{r}}\cdot\vec{v}} \\ \vec{A}(\vec{r},t) &= \frac{\vec{v}}{c^2}V(\vec{r},t). \end{aligned} \tag{B.1}$$

In equation (B.1) $\tilde{r}$ denotes the position of the evaluated point relative to the position of the source. The source position is to be evaluated at the retarded time $t_r = t - \tilde{r}/c$ which takes into account the finite propagation speed c of the electromagnetic fields. From these potentials one can derive the electric and magnetic fields associated with the particle:

$$\begin{aligned} \vec{E}(\vec{r},t) =& -\nabla V - \frac{\partial\vec{A}}{\partial t} = \frac{q}{4\pi\epsilon_0}\frac{\tilde{r}}{(\vec{\tilde{r}}\cdot\vec{u})^3}\Big((c^2-v^2)\vec{u} + \vec{\tilde{r}}\times(\vec{u}\times\vec{a})\Big) \\ \vec{B} =& \nabla\times\vec{A} = \frac{1}{c}\hat{\tilde{r}}\times\vec{E}(\vec{r},t), \end{aligned} \tag{B.2}$$

where the vector $\vec{u}$ is defined as $\vec{u} = c\hat{r} - \vec{v}$. The first part of the electric field expression is often referred to as the velocity field. The second contribution $\sim \vec{\tilde{r}}\times(\vec{u}\times\vec{a})$ is the radiation field $\vec{E}_{rad}$, which is the part of the electric field carried off to infinity. Radiated power per unit area is now given by the pointing vector $\vec{S}$, which again has a radiation contribution:

$$\vec{S}_{rad} = \frac{\vec{E}_{rad}\times\vec{B}}{\mu_0} = \frac{E_{rad}^2}{\mu_0 c}\hat{\tilde{r}}. \tag{B.3}$$

Next, the power radiated P by the particle into the solid angle $d\Omega$, corrected for the fact that the field source is moving, is given by [11];

$$\frac{\partial P}{\partial\Omega} = \frac{\vec{\tilde{r}}\cdot\vec{u}}{\tilde{r}c}S_{rad}\tilde{r}^2 = \frac{q^2}{16\pi^2\epsilon_0}\frac{|\hat{\tilde{r}}\times(\vec{u}\times\vec{a})|^2}{(\hat{\tilde{r}}\cdot\vec{u})^5}. \tag{B.4}$$

Integration over all angles yields Liénards formula:

$$P = \frac{\mu_0 q^2\gamma^6}{6\pi c}\Big(a^2 - |\frac{\vec{v}\times\vec{a}}{c}|^2\Big). \tag{B.5}$$

Lastly, the power distribution as a function of solid angle and frequency can be studied. The total energy emitted per solid angle can be re-written using equation (B.4);

$$\begin{aligned}\frac{\partial W}{\partial \Omega} =& \int_{-\infty}^{\infty} \frac{dP}{d\Omega} dt = \int_{-\infty}^{\infty} |\vec{C}(t)|^2 dt \\ \vec{C}(t) =& \frac{q\sqrt{c}}{4\pi\sqrt{\epsilon_0}} \frac{\hat{\vec{r}} \times (\vec{u} \times \vec{a})}{(\hat{\vec{r}} \cdot \vec{u})^3},\end{aligned}$$

and defining the Fourier transform of $\vec{C}(t)$;

$$\vec{C}(\omega) = \frac{1}{\sqrt{2\pi}} \int_{-\infty}^{\infty} \vec{C}(t) \exp(i\omega t) dt,$$

so that [92]:

$$\begin{aligned}\frac{\partial^2 W}{\partial \Omega \partial \omega} =& 2|\vec{C}(\omega)|^2 \\ \vec{C}(\omega) =& \frac{-iq\omega}{4\pi\sqrt{2\pi\epsilon_0 c}} \int_{\infty}^{\infty} \hat{\vec{r}} \times (\hat{\vec{r}} \times \vec{\beta}) \exp\Big(i\omega(t_r - \hat{\vec{r}} \cdot \vec{w}/c)\Big) dt_r,\end{aligned} \tag{B.6}$$

the quantity β introduced here is the ratio of the particle velocity over the speed of light.

Appendix C

CRM metastable resolved rate equations

Here the ADAS extension of the rate equation model for including metastable species is presented. Each ionization state is subdivided into metastable states σ, which includes the ground state. Metastable parent states, which belongs to ionization level $(z+1)$, are denoted by ν. Similarly, daughter states are labelled using ρ. Different combinations of parent-child metastable pairs are linked by different transition coefficients such as $S_{CD,(z,\sigma\to\nu)}$. Furthermore, two additional coupling coefficients between metastables are added. Direct coupling is denoted by $Q_{CD,(z,\sigma\to\sigma')}$. Metastable formation as a result of recombination of state σ to ρ and subsequent re-ionization to state σ' is described by $X_{CD,(z,\sigma\to\sigma')}$. For a given metastable the time evolution is now given by:

$$\begin{aligned}\frac{1}{n_e}\frac{dn_{(z,\sigma)}}{dt} = &\sum_{k=1}^{M_{(z-1)}} S_{CD,(z-1,\rho[k]\to\sigma)} n_{(z-1,\rho[k])} \\ &- \Big(\sum_{k=1}^{M_{(z+1)}} S_{CD,(z,\sigma\to\nu[k])} + \sum_{k=1}^{M_{(z-1)}} \alpha_{CD,(z,\sigma\to\rho[k])} + \frac{n_o}{n_e} \sum_{k=1}^{M_{(z-1)}} C_{CD,(z,\sigma\to\rho[k])} + \\ &\sum_{k=1}^{M_{(z)}} Q_{CD,(z,\sigma\to\sigma'[k])} + \sum_{k=1}^{M_{(z)}} X_{CD,(z,\sigma\to\sigma'[k])} \Big) n_{(z,\sigma)} \\ &+ \sum_{k=1}^{M_{(z+1)}} \alpha_{CD,(z+1,\nu[k]\to\sigma)} n_{(z+1,\nu[k])} + \frac{n_o}{n_e} \sum_{k=1}^{M_{(z+1)}} C_{CD,(z+1,\nu[k]\to\sigma)} n_{(z+1,\nu[k])} + \\ &\sum_{k=1}^{M_{(z)}} Q_{CD,(z,\sigma'[k]\to)} n_{(z,\sigma'[k])} + \sum_{k=1}^{M_{(z)}} X_{CD,(z,\sigma'[k]\to)} n_{(z,\sigma'[k])},\end{aligned} \tag{C.1}$$

where $M_{(z)}$ is the amount of metastables of the ionization level z, and $\sigma[i]$ refers to the i^{th} metastable state of a certain ion. The system of linear equations can again be represented in matrix form, where things are complicated by the fact that the rate coefficients now take on the form of matrices themselves [60]:

$$\begin{bmatrix} d\mathbf{n}_{(0)}/dt \\ d\mathbf{n}_{(1)}/dt \\ \vdots \\ d\mathbf{n}_{(Z)}/dt \end{bmatrix} = \mathbf{C} \begin{bmatrix} \mathbf{n}_{(0)} \\ \mathbf{n}_{(1)} \\ \vdots \\ \mathbf{n}_{(Z)} \end{bmatrix}, \tag{C.2}$$

where the density vectors of each inonization state contain the population of all metastables:

$$\mathbf{n}_{(z)} = \begin{bmatrix} n_{(z,\sigma[1])} \\ n_{(i,\sigma[2])} \\ \vdots \\ n_{(i,\sigma[M_{(z)}])}. \end{bmatrix}$$

The matrix elements in equation (C.2) are given by

$$\begin{aligned} \mathbf{C}_{z,z-1} &= \mathbf{S}_{CD,(z-1\to z)} \\ \mathbf{C}_{z,z} &= \begin{cases} -n_e \mathbf{S}_{CD,(0)} & \text{if } z = 0 \\ -n_e(\mathbf{S}_{CD,(z)} + \mathbf{Q}_{CD,(z)} + \mathbf{X}_{CD,(z)} + \boldsymbol{\alpha}_{CD,(z)} + \frac{n_o}{n_e}\mathbf{C}_{CD,(z)}) & \text{if } z = 2,3,...,Z-1 \\ -n_e(\boldsymbol{\alpha}_{CD,(Z)} + \frac{n_o}{n_e}\mathbf{C}_{CD,(Z)}) & \text{if } z = Z \end{cases} \\ \mathbf{C}_{z,z+1} &= n_e \boldsymbol{\alpha}_{CD,(z+1\to z)} + n_o \mathbf{C}_{CD,(Z)}. \end{aligned} \tag{C.3}$$

The boldface symbols are all matrices of the form:

$$\begin{aligned} \mathbf{S}_{CD,(z)}(i,i) &= \sum_{k=1}^{M_{(z+1)}} S_{CD,(z,\sigma[i]\to\nu[k])} \\ \mathbf{S}_{CD,(z)}(i,j\neq i) &= 0 \\ \mathbf{S}_{CD,(z-1\to z)}(i,j) &= S_{CD,(z-1,\rho[j]\to\sigma[i])} \\ \boldsymbol{\alpha}_{CD,(z)}(i,i) &= \sum_{k=1}^{M_{(z-1)}} \alpha_{CD,(z,\sigma[i]\to\rho[k])} \\ \boldsymbol{\alpha}_{CD,(z)}(i,j\neq i) &= 0 \\ \boldsymbol{\alpha}_{CD,(z+1\to z)}(i,j) &= \alpha_{CD,(z+1,\nu[j]\to\sigma[i])} \\ \mathbf{C}_{CD,(z)}(i,i) &= \sum_{k=1}^{M_{(z-1)}} C_{CD,(z,\sigma[i]\to\nu[k])} \\ \mathbf{C}_{CD,(z)}(i,j\neq i) &= 0 \\ \mathbf{C}_{CD,(z+1\to z)}(i,j) &= C_{CD,(z+1,\nu[j]\to\sigma[i])} \\ \mathbf{Q}_{CD,(z)}(i,i) &= -\sum_{k=1;k\neq i}^{M_{(z)}} Q_{CD,(z,\sigma[k]\to\sigma[i])} \\ \mathbf{Q}_{CD,(z)}(i,j\neq i) &= Q_{CD,(z,\sigma[i]\to\sigma[j])} \end{aligned}$$

$$\begin{aligned} \mathbf{X}_{CD,(z)}(i,i) &= -\sum_{k=1;k\neq i}^{M_{(z)}} X_{CD,(z,\sigma[k]\to\sigma[i])} \\ \mathbf{X}_{CD,(z)}(i,j\neq i) &= X_{CD,(z,\sigma[i]\to\sigma[j])} \end{aligned}$$

Appendix D

Compositions and specifications of interference filters

D.1 Filter composition

Real commercially available interference filters consist of vacuum-deposited thin film stacks on top of a substrate. The stack type discussed here only contains dielectric layers. Mirrors are created by quarter wavelength slab stacks of alternating high and low refractive index to reflect most of the light outside of the transmission region. Light with a wavelength matching the one fourth wavelength optical thickness of the layers is efficiently reflected back through constructive interference of outgoing waves at the first mirror surface [93]. Tuning of the reflectivity occurs through material choice, which influences the refractive index, and the amount of deposited layers. Behind the first mirror, there is a spacer layer with an optical thickness equal to half of the transmission wavelength. This serves as the cavity depicted in figure 5.3. Below this section is another mirror stack to complete the cavity [94]. A single filter can contain multiple cavities to ensure narrow transition bands and strong light blocking in neighbouring spectral ranges.

For some applications the dielectric spacer material between the mirrors is replaced by a metal. This is however detrimental for the sharp slopes around the bandpass, rendering such a material unsuitable for an application in which close lying emission lines have to be separated.

In all-dielectric interference filters the blocking well outside the transmission range is often limited. To ensure the camera is not exposed to infrared and gamma radiation broad band blocking layers are included in the filter stack. The choice of layer thickness is guided by a trade-off between out-of-band blocking and peak transmission [95].

Besides the number of layers, layer thickness and the used materials, also the employed deposition technique influences the transmission properties of the overall stack. Control over the deposition process expands the accessible optical parameter space via changes in the microstructure of the material. Tuning is not a straight forward process, as also the mechanical properties of the filters depend on these small scale features [75].

D.2 Specifying filter performance

In filter optics, the quantity most commonly used to describe the degree of blocking is the optical density OD:

$$OD = \log_{10}(\frac{1}{Tr}), \tag{D.1}$$

where Tr is the transmission. To illustrate, OD 4 blocking indicates a transmission of 0.01 %. Note that the blocking outside of the transmission band near wavelengths of strong non-targeted emission lines should be high for MANTIS+ filters. If one for instance wants to image some line which is a factor 1000 weaker than D_α, the OD of the filter should stay above 4 to ensure that the Balmer alpha emission is not the dominant light transmitted through the filter. Such pollution is not avoidable and knowing the D_α intensity corrections can be made.

Up till this point in the discussion, the fact that not all light is transmitted or perfectly reflected has been ignored. Scattering of light on imperfect interfaces on the filter surface and interior cause a loss of intensity to be detected

by any of the sensors. Furthermore, some of the light is absorbed in each layer of the optical coating and converted to heat [75]. For the MANTIS+ application the light intensities are relatively low, so no damage is expected from sudden heating. Absorption A_r, transmission T_r and reflection R_r together add up to unity, which means that any of the three can be computed if the other two are known:

$$A_r + T_r + R_r = 1. \tag{D.2}$$

Another filter parameter of considerable importance for the MANTIS+ system is the flatness of the reflecting surface. This determines quality of the image at the next filter, as curvatures which are unaccounted for can shift the focal point along the optical axis, or cause blurring via an increase focal spot size. Flatness is typically described as a superposition of spherical surface curvature and surface irregularities.

Surface curvature can result from stress inherent to the stack configuration of the filter. The radius of curvature has been found to increase quadratically with the clear aperture of the filter and linearly with the coating film thickness. In case of double sided coating, the last quantity is replaced by the difference between the thickness of the two sides. Increasing the substrate thickness will reduce the bending error in a quadratic fashion [93]. From these observations it is concluded that in order to minimize unwanted bending, double coated filters with comparable coating thickness on both sides are desirable. The filter diameter can not be altered in the current application, but is a factor of two smaller than in the MANTIS system. Changing the coating thickness to tune bending effects is not recommended, as it affects transmission properties and production costs. Most design freedom is found in the substrate thickness. Here one searches for a balance between having a low surface curvature and achieving a high transmission. Specifying a maximum filter curvature, manufacturers can design the filter stack such that the transmission is maximized.

Filter flatness is commonly specified in terms of central transmission wavelengths or the wavelength of a reference laser [96]. The height difference between the edge of the clear aperture and the filter center is then measured on the side under consideration. Note that this definition thus depends on the filter size.

Surface roughness on the small scale is often expressed in 'scratch/dig' terms. Scratches are measured in units of 0.1 μm. Digs refer to bubble or pit like features of which the diameter is indicated in units of 10 μm. A scratch/dig of 60/40 has a maximum scratch size of 6 μm and a maximum dig diameter of 400 μm.